PEOPLE'S DEMOCRATIC REPUBLIC OF ALGERIA
MINISTRY OF HIGHER EDUCATION AND SCIENTIFIC RESEARCH

UNIVERSITY KASDI MERBAH OF OUARGLA
FACULTY OF APPLIED SCIENCES
DEPARTMENT OF MECHANICAL ENGINEERING

THESIS

Submitted for obtaining the LMD Doctorate degree in

Mechanical Engineering

Specialty: Mechanical and Productive Manufacturing

By

BENABDERAZAG Khalil

Entitled

Identification of the Mechanical Properties of Composite Materials Through a Spectral Study

Publicly defended on 09 /07 /2025, before the jury composed of:

CHERRAD Noureddine	Prof	University Kasdi Merbah - Ouargla	President
GUEBAILIA Moussa	Prof	University Kasdi Merbah - Ouargla	Supervisor
BELOUADAH Zouheyr	MCA	Ecole Nationale Polytechnique ENP	Co-Supervisor
BOUAKBA Mustapha	Prof	University Kasdi Merbah - Ouargla	Examiner
TOUFIK Ameur	MCA	University Kasdi Merbah - Ouargla	Examiner
DJILANI necib	MCA	University of el-oued	Examiner

REPUBLIQUE ALGERIENNE DEMOCRATIQUE ET POPULAIRE

MINISTERE DE L'ENSEIGNEMENT SUPERIEUR ET DE LA RECHERCHE SCIENTIFIQUE

UNIVERSITE KASDI MERBAH OUARGLA

FACULTE DES SCIENCES APPLIQUEES

DEPARTEMENT DE GENIE MECANIQUE

THÈSE

Présentée pour l'obtention du diplôme de Doctorat LMD

Spécialité : Fabrication Mécanique et Productique

Par

BENABDERAZAG Khalil

THÈME

Identification des propriétés mécaniques des matériaux composites par une étude spectrale

Soutenue publiquement le 07 / 09 / 2025 devant le jury :

CHERRAD Noureddine	Prof	Université de Ouargla	Président
GUEBAILIA Moussa	Prof	Université de Ouargla	Encadrant
BELOUADAH Zouheyr	MCA	Ecole Nationale Polytechnique	Co-encadrant
BOUAKBA Mustapha	Prof	Université de Ouargla	Examinateur
TOUFIK Ameur	MCA	Université de Ouargla	Examinateur
DJILANI necib	MCA	Université de el-oued	Examinateur

Dedication

I dedicate this work to my dear parents may God, the Almighty, bless you with health, long life, and happiness. I also extend this dedication to my family, my brothers and sisters, as well as my friends, colleagues, and all those who have supported me, whether near or far.

Furthermore, I dedicate this work to the researchers and engineers who shape the future and drive societal progress, embracing their responsibility and privilege in advancing humanity.

ACKNOWLEDGEMENTS

I would like to begin by expressing my deepest gratitude to God, the Almighty, for granting me the strength, perseverance, and clarity of mind necessary throughout this doctoral journey.

I wish to extend my special thanks to Dr. GUEBAILIA Moussa, my thesis supervisor, whose guidance and advice have been invaluable in directing my research. I would also like to express my appreciation to Dr. BELOUADAH Zouheyr, my thesis co-supervisor, whose contributions have greatly enriched my experience and the quality of my thesis. May God reward your efforts.

I also thank Professor TOUBAL Lotfi from the Université du Quebec à Trois-Rivières, Canada, for his expertise and support, which were essential to achieving a high level of research.

Furthermore, I express my gratitude to the Faculty of Applied Sciences of Kasdi Merbah Ouargla, the National Polytechnic School, and the Research Center in Semi-conductors Technology for Energetic (CRTSE) for creating an environment conducive to research and learning, as well as to all those who contributed, directly or indirectly, to the realization of this work.

Finally, I would like to express my profound gratitude to my family for their unconditional support throughout this demanding academic journey.

List of Abbreviations and Symbols

AE: Acoustic Emission

ANN: Artificial Neural Network

CV: Cross-Validation

DIC: Digital Image Correlation

dB: Decibels (Amplitude of AE Signals)

DSC: Differential Scanning Calorimetry

E: Young's Modulus (GPa)

F_c: Crystallinity Fraction

FTIR: Fourier Transform Infrared Spectroscopy

GPa: Gigapascal (Unit of Young's Modulus)

IET: Impulse Excitation Technique

kHz: Kilohertz

L.S: Lygeum spartum

MPa: Megapascal (Unit of Stress)

MSE: Mean Squared Error

NDT: Non-Destructive Testing

PLA: Polylactic Acid

R^2: Coefficient of Determination (R-squared)

SEM: Scanning Electron Microscopy

SHM: Structural Health Monitoring

T: Temperature (°C)

t: Time (s)

TGA: Thermogravimetric Analysis

ΔT: Temperature Change (°C)

Δ**H**: Enthalpy

Δ**H_m**: Enthalpy of Fusion

Δ**H_m0**: Enthalpy of Fusion at 100% Crystallinity

ε: Strain

σ: Stress (MPa)

μs: Microsecond

Table of Contents

Chapter I State of the art

Chapter II Materials and Experimental Techniques

Chapter III Physicochemical and Thermal Characterization of Lygeum spartum/PLA Biocomposite

Chapter IV Mechanical Properties and Damage Assessment Through Spectral Analysis

List of figures

List of tables

General introduction

General introduction

Composite materials have emerged as a dominant force in various fields and industries in recent years, gradually replacing traditional materials owing to their superior properties. Over time, they have captured a significant share of the industrial materials market. In the aerospace industry, for instance, steel and aluminum alloys have been superseded by other composite materials that offer superior performance at a lower cost. In many cases, traditional materials may not be able to meet the specific requirements of certain applications. For example, components used in space equipment must withstand harsh conditions such as high pressure and extreme temperatures. Ceramic composites have proven to be the only viable solution for such demanding applications. Similarly, in the medical field, composite materials have played a pivotal role in the development of artificial organs that are lightweight, affordable, and readily accessible to patients. Composite materials have also made significant advances in other industries such as automotive and construction. In the automotive sector, carbon fiber-reinforced polymers (CFRP) are used to manufacture high-performance vehicles, offering improved fuel efficiency and safety due to their lightweight and high-strength properties. In the construction industry, fiber-reinforced polymers (FRP) have become crucial for reinforcing concrete structures, as they offer superior corrosion resistance and longevity compared to traditional steel reinforcements, thereby reducing maintenance costs and enhancing structural durability. These examples further demonstrate the versatility and growing importance of composite materials across multiple sectors.

Among the various types of composite materials, those based on thermoplastic plastics and natural fibers have gained widespread popularity. These materials offer several advantages over other composite materials, such as their wide availability and affordability. In particular, composites made from a PLA matrix and plant fibers are biodegradable and can be degraded in the environment without leaving any harmful residues. PLA is a bio-based polymer derived from natural sources, while plant fibers are readily available and renewable.

To study and analyze the mechanical properties of these materials, classical mechanical tests are employed. However, these tests can be expensive and destructive to the sample. Fortunately, advancements in research have led to the development of non-destructive methods that can be used

to understand the behavior of these materials under stress and obtain their mechanical properties without causing any damage. For example, the acoustic emission method can be used to detect micro-damage and phenomena that occur at the microstructure level. This information can then be used to predict the failure of a particular structure. Digital image correlation can be used to analyze consecutive images of a sample or structure to determine the behavior and areas of deformation or stress. The mechanical properties of the sample can also be extracted from the displacement field. Additionally, the impulse excitation technique can be used to determine the mechanical properties of a sample without causing any damage. This technique involves measuring the free vibration of the sample to obtain its Elasticity modulus and Poisson's ratio. This method is considered to be one of the cheapest and fastest ways to obtain the mechanical properties of a material.

In our research, we produced 100% biocomposites by extracting lygeum spartum L fibers, chemically treating them, and then dissolving PLA in a chloroform solution to produce granules. After drying, the granules were cut in preparation for the extrusion process. We also produced filament for three-dimensional printing. Subsequently, we printed 3D printing samples using both filament biocomposite and neat PLA. This allowed us to compare the effect of adding lygeum spartum L fibers on the mechanical, thermal, and physical properties of the material.

The thesis is divided into five sections:

- The first chapter provides a general overview of composite materials, including their history, areas of use, and role in solving problems that were difficult to address with traditional materials.
- The second chapter discusses the methods used to extract the fibers, the elaboration process, the extrusion process, and three-dimensional printing.
- The third chapter compares the chemical, physical and thermal properties of composite samples and neat PLA, and examines the effect of the fibers on these properties.
- The fourth chapter investigates the mechanical properties of the materials using classical methods such as tensile and flexural tests, as well as a spectral study that uses non-destructive methods such as the impulse excitation technique, acoustic emission, in addition to digital image correlation, and also a machine learning for the classification of the damage modes and the prediction of the stress during the mechanical testing.

- The last chapter is dedicated for the discussion of these results and the potential of our study for the progression of the material science especially the biocomposite materials.

Chapter I

State of the art

I.1 Introduction

In this chapter, an overview of the latest innovations and developments in the field of natural fiber composites that have seen a rise in their use in several industries. Plant based fibers have several benefits compared to synthetic ones, such as lower cost, decreased environmental harm, and ability to biodegrade. These fibers are being increasingly used as reinforcements in polymer matrices to produced biocomposites with enhanced mechanical performance and sustainability. Types of natural fibers, their extraction methods and their benefits to composite materials are discussed in this chapter. Moreover, the disadvantages of natural fibers, such as fiber-matrix integration and compatibility are discussed. A summary of the current literature on natural fiber reinforced composites is done with aim towards possible applications in the automotive, construction, and aerospace industries. This chapter provides a glimpse into the rationale behind this research and the part played by Lygeum spartum L. fibers in the creation of durable and sustainable biocomposites.

I.2 Generalities on composite materials

A composite material is defined as a material that is made of at least two different and incompatible components whose combination results in a material with properties superior to those of the individual components [1, 2]. Within a composite material, there exists a matrix (continuous phase) and reinforcement (discontinuous phase) which possesses superior mechanical properties (strength and stiffness) than the matrix. An interface is created between the two components, which ensures that adequate bonding occurs by facilitating stress transfer from one component to the other (**Figure I.1**).

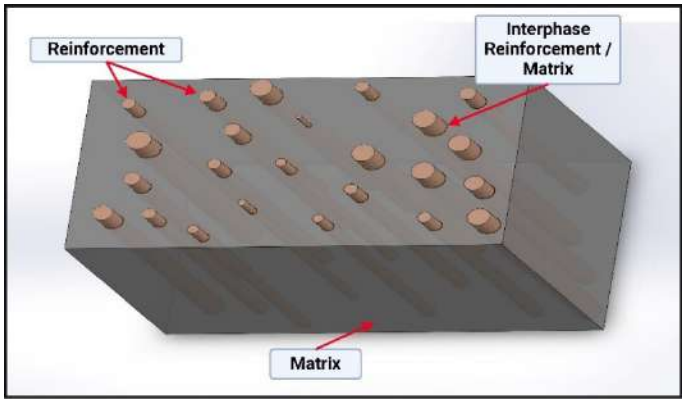

Figure I-1: a 3D model illustrates composite material matrix and the reinforcement [1, 2].

Composite materials are distinguished by the type of these matrix constituents. These include composites with organic matrices, which can be thermoplastic or thermosetting, as well as those with mineral matrices, such as metallic (MCM) or ceramic (CCM) matrix composites (**Figure I.2**). Characteristics of composite material is based on the nature of its constituents such as the type of the reinforcement morphology and distribution, volume fraction, the interfacial region of the reinforcement and the matrix, and the fabrication methods used. Compared to the other materials, such as metals, polymers, or ceramics, composites have better mechanical properties and thus are seeing increased use in the automotive and aeronautical industries. Unfortunately, composite materials were often usually described as glass, carbon or other fibers embedded in a thermosetting, or thermoplastic matrix [3-5]. Fortunately, composite materials containing natural fibers have become of great interest to many researchers in recent years due to their potential environmental benefits.

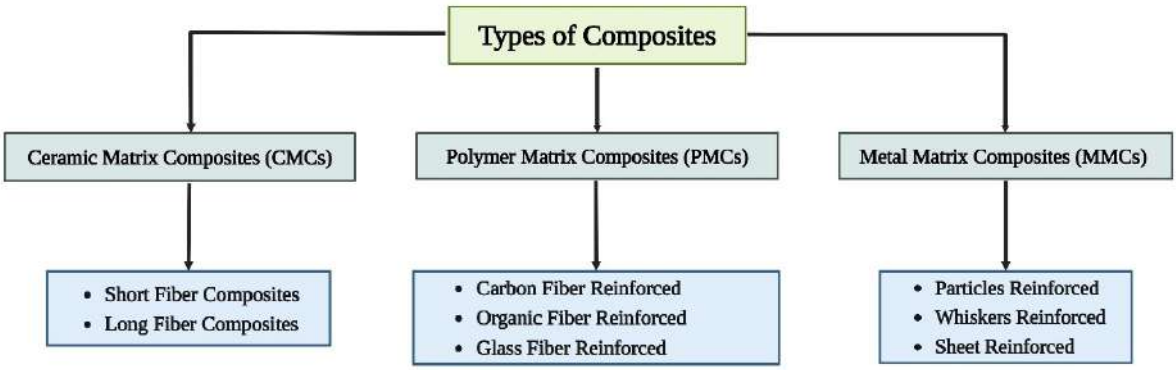

Figure I-2: Classification of Composite Materials Based on Matrix Type and Reinforcement Structure [6].

I.3 Natural fibers

In recent years, natural fibers have gained popularity in producing composite materials. These materials are advantageous because of their competitiveness such as, being biodegradable, light weight, cheap to produce and having better mechanical properties. Based on the source, natural fibers are divided into three types: plant, animal or mineral fibers as illustrated in (**Figure I.3**).

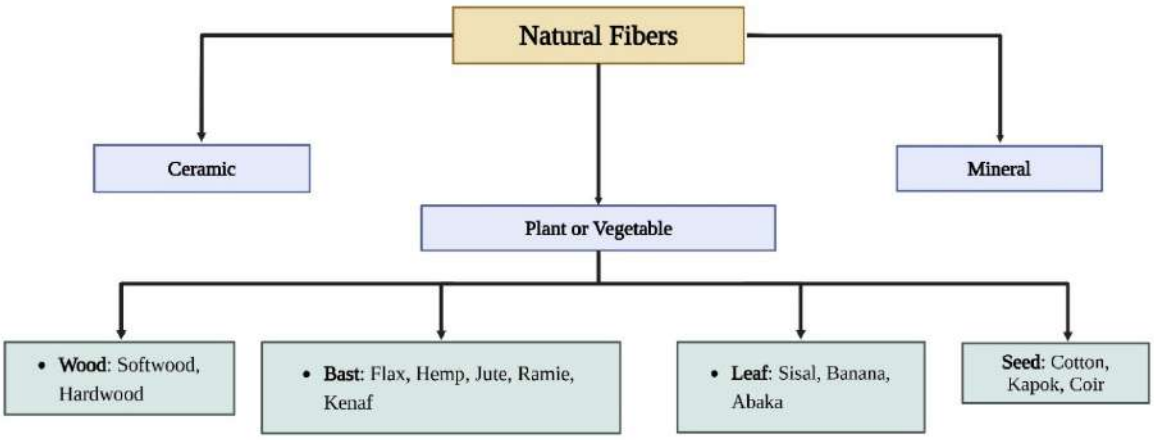

Figure I-3: Classification of natural fibers based on their origin [7].

I.4 Application of Natural Fibers

In our daily life, we use natural fibers, as well as plant fibers, in textiles and ropes, fabrics, and even papers. At present, with the increased focus on the green economy, environmental friendly natural fibers have become significant for reinforcement in composites [8]. These materials are widely used in the automotive, building and many other industries. The uses and market shares of natural fiber composites are given in **Table I.1.**

Table I-1: Market Share Distribution of Natural Fiber Composites by Industry [9].

Field of Application	Percentage (%)
Building and Construction	35%
Automotive	25%
Aerospace	10%
Electrical & Electronics	15%
Other Industries	10%
Sports	5%

I.5 Structure and Composition of a Plant Fiber

The properties of a plant fiber are directly related to its composition of natural polymers. The chemical composition of these fibers can be classified into two groups:

- Macromolecular Substances: These materials, which are mainly cellulosic in nature, hemicellulose, and lignins, form the cell wall. These materials are integrated in a manner that requires vigorous chemical separation treatments for disintegration.
- Low Molecular Weight Substances: These are more specific to certain species and include extractable substances or extracts.

Each fiber is a multilayer biocomposite, composed of cellulose, the most rigid structural element, covered by a matrix of lignin (**Figure I.4**). Plant fiber composition is dependent upon botanical origins, climate, age, and mode of extraction [10, 11].

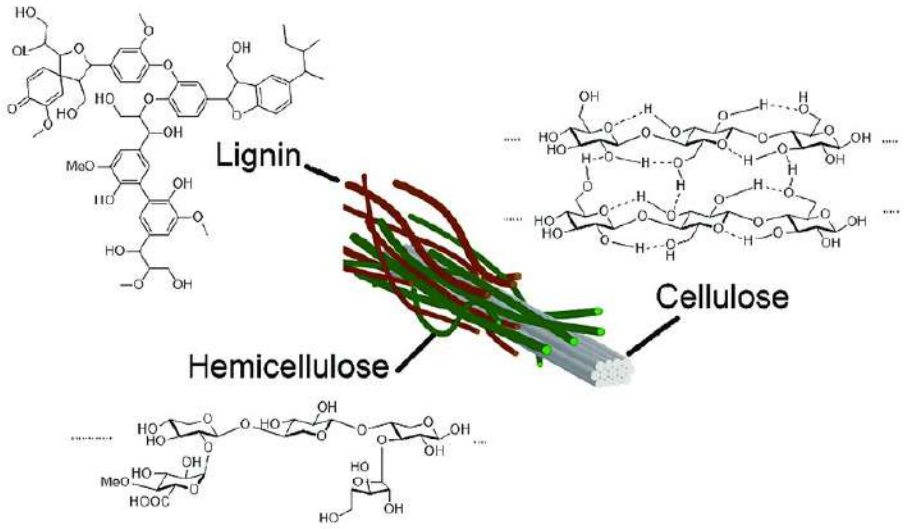

Figure I-4: Structural and Main Chemical Components of Plant Fiber: Cellulose, Hemicellulose, and Lignin [12].

I.5.1 Cellulose

The main component of plant fiber is cellulose. In terms of structure, cellulose is a polymer consisting of multiple glucose molecules ($C_6H_{11}O_5$) arranged on a single chain. Cellulose has both

ordered crystalline and disordered amorphous regions. Cellulose also has strong hydrophilic property, and while it is soluble in few solvents and is resistant to them, it can be broken down into water-soluble sugars through acid hydrolysis [13-15].

I.5.2 Hemicellulose

Hemicellulose is one of the major ingredients forming the cell walls of the plant fibres, located beside the cellulose and lignin structures. Hemicellulose is associated with cellulose but unlike it, is amorphous, lower in weight and more elastic. Its flexibility adds to the elasticity of plant fibers enabling stretching of cell walls while growing plants [16, 17], Hemicellulose is a heteropolymer made up of different monomer sugars such as, arabinose, xylose, glucose, galactose, mannose, and uronic acids [17, 18]. Its chemical composition is more complex and less linear than that of cellulose.

I.5.3 Lignin

Approximately, lignins account for 15 to 35% of the dry weight of lignocellulosic materials. They are the predominant polyphenolic compounds in plants [15, 19]. Lignin provides rigidity and strength to wood and plants, which are in turn used to partially defend against some vegetative enemies parasitic in nature [20]. The chemical structure of lignin is illustrated in **Figure I.4**.

I.5.4 Other Components

Pectin is an acidic polysaccharide containing uronic acid monomers as its main chain. It gives some degree of elasticity to the plant [21], and is the most hydrophilic constituent of plant fibers owing to the presence of carboxylic acid groups [22, 23]. The chemical structure of pectin is shown in **Figure I.4**. Moreover, extractives, which constitute 2 to 5% of the dry mass, include different types compounds with low molecular weights. These substances protect and defend the plant against insect attacks.

I.6 Lygeum spartum (Senagh)

The plant known as “Senagh” or Lygeum spartum is a typical grass of the Mediterranean region and belongs to the Poaceae family. It is widespread in the highlands of Algeria and Morocco but also grows wild in southern Spain and North Africa. The stems of the Mediterranean plant Lygeum spartum has a high percentage of cellulose making it very important in paper industry [24, 25]. In

a comparative study of herbaceous plants like Lygeum spartum carried out by nedjimi et al. [26], it was noted that it may serve as an important forage resource in the semi-arid regions of Spain. The study also indicated that Lygeum Spartum contains from 6.32 to 8.48% lignin and from 5.27 to 6.73% ash.

Belouadah et al. [25], worked further on the use of Lygeum spartum fibers as natural cellulosic fibers in polymer composites looking at their properties. The study gave an in-depth description of the fiber with eco-friendly extraction as well as its morphological, chemical and mechanical properties. It was noted that the fibers had a significant crystallinity index of 46.19% which is required for adequate mechanical strengthening.

According to the thermogravimetric analysis, the fibers show a thermal stability up to 220°C and possess an activation energy of 68.77 kJ/mol. The study managed to demonstrate that the fibers achieved a tensile strength of up to 280 MPa with a Young's modulus of 13.2 GPa, confirming their effectiveness as reinforcements in composite materials.

At the moment, Lygeum spartum (L.S) is used as a reinforcement in polylactide (PLA) filament for 3D printing for the first time in our study (**Figure I.5**).

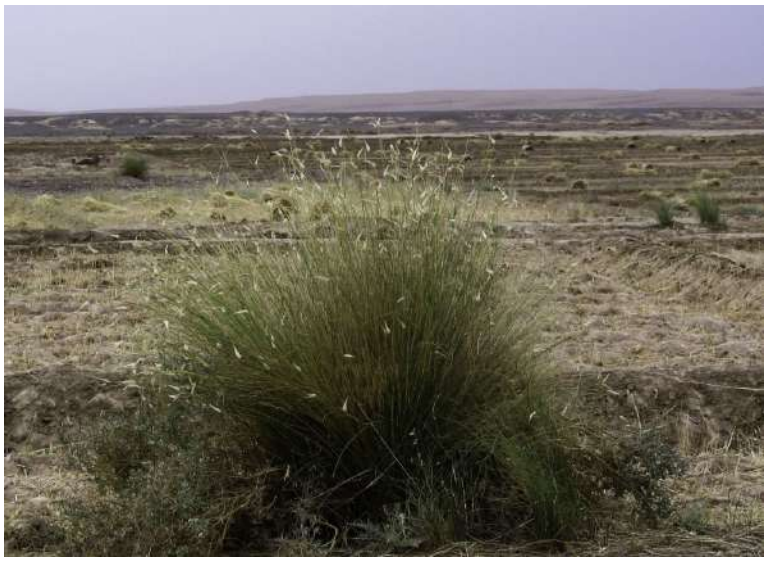

Figure I-5: The plant “Lygeum Spartum L.” known as Senagh which is abundant in the Hodna region (Msila, Algeria) [25].

I.7 Exploitation of plant fibers as reinforcements in polymer composites

Driven by renewability, environmental benefits and desirable mechanical properties, plant fibers have emerged as valuable reinforcers in polymers. These fibers are extracted from natural sources such as flax, hemp, jute, kenaf and sisal and have significant advantages over synthetic reinforcements like glass and carbon fibers. Plant fibers are lightweight, biodegradable and cost effective, essential for industries such as automotive, construction and packaging where performance and sustainability are critical concerns. In addition to their low environmental impact, plant fibers have considerable specific strength and stiffness, which has aided in enhancing the mechanical performance of polymer composites with an increase in toughness and reduced weight [27-29].

There are challenges that need to be overcome in the integration of plant fibers and polymers due to the aspect of inherent hydrophilicity. This may hinder the effectiveness of compatibility with hydrophobic polymer matrices [27]. To counteract this, there are common treatments like chemically treating, surface modifying and using alkali treatments or coupling agents to enhance the adhesion of the fiber matrix and improve the mechanical properties and moisture resistance. Furthermore, plant fibers are very effective in energy absorption, which gives it great use in applications that are in need of impact resistance, such as in automotive components and sports equipment. As improvements are formulated on extraction processes and fiber treatment, the scope for the usage of plant fibers as reinforcements in polymer composites is increase, providing a sustainable option for high powered engineering materials.

I.8 Chemical Modification of Plant Fibers

In order to enhance the adhesion and the dispersion of plant fibers in polymer matrices, a chemical modification is very important. These treatments can be broadly classified as either physical or chemical modifications, where effective modification of the fibers will enhance the fibers to matrix adhesion. The reason why chemical treatments are necessary is more than one; they prepare the fiber surface, modify the chemical structure of the fiber, decrease the moisture absorption, roughen the surface, enhance the mechanical properties, and increase the thermal stability. Because cellulose is the predominant constituent of plant fibers, most of the chemical treatments target the structural modification of cellulose. Modification is more conveniently done on the non-crystalline

(amorphous) regions of cellulose since the crystalline regions are more resistant to chemical attack [29, 30].

Kalia et al., 2009 [31], proved that certain chemical modifications aid in improving fiber surface characteristics which leads to better adhesion to polymer matrices. Commonly practiced are alkali treatment (NaOH), acetylation, permanganate treatment, silane coupling, and all sorts of pre-treatments with coupling agents. **Table I.2** shows the mechanical properties of palm fibers after undergoing various chemical treatments. Some treatments, as NaOH, are known to reduce tensile strength because of delignification and partial destruction of cellulose. However, these treatments lead to higher elongation at break and greater overall flexibility as well. Other treatments, such as acrylic and silane, are known to produce covalent bonds formed between the fiber and the matrix which aid in maintaining the tensile strength while improving fiber stiffness.

The study of Kalia et al indicated that untreated fibers possess adequate mechanical properties; however, they tend to lack efficient load transfer in the polymer composites, which results in low mechanical performance of the final product. Therefore, the fibers are recommended to be subjected to chemical modification in order to enhance the fiber-matrix bonding. Not only do these modifications enable a reduction in fiber's moisture absorption, but they also increase fiber's interaction to the polymer matrix for better interfacial bonding. Consequently, the chemically treated fiber composites have been reported to provide better mechanical properties, including greater tensile strength, greater stiffness, and greater durability (Mohanty et al., 2000) [32].

Table I-2: Effect of pretreatments on tensile properties of sisal fiber [32].

Treatment methods	Tensile strength (g/tex)	Tensile modulus ($\times 10^3$ g/tex)	Elongation at break (%)
Untreated	30.7	1.18	2.5
Benzol/alcohol	38.8	0.99	3.7
Acetic acid + alkali	9.3	0.39	2.6
Alkali	31.7	0.53	7.5
Acetylated	33.2	0.35	8.3
Thermal	42	1.22	3.5
Alkali-thermal	27.6	0.7	4.7
Thermal-alkali	25.7	0.71	4.4

I.9 Alkaline Treatment with NaOH

The alkaline treatment, also called mercerization, is one of the most common treatments of plant fibers. This is an old technique which the textile industry has mostly employed and is now widely used on plant fibers that serve as reinforcements for thermosetting and thermoplastic polymers [33-35]; The treatment includes the following reaction of sodium hydroxide (NaOH) with cellulose:

$$\text{Cellulose} - OH + NaOH \rightarrow (\text{Cellulose} - O^{-})\, Na^{+} + H_2O + \text{impurities}$$

Alkaline treatments have been shown to remove undesirable components such as hemicellulose, lignin, pectin, and oils from the fibers, This treatment leads to considerable dimensional, morphological, and mechanical changes [36-40]. These non-cellulosic materials that cover the cellulose structure are removed to produce microfibrils which increase the surface roughness of the fibers. The increased surface roughness improves the physical bonding between the fibers and the polymer matrix which leads to better impregnation and stronger fiber-matrix adhesion.

Alkaline treatment is known to increase the crystallinity of the fibers due to the removal of amorphous regions which leads to improved mechanical properties [36, 41]. The concentration of the alkali solution must however be regulated, due to the fact that high concentrations can lead to reductions in crystallinity and thus, downgrading the fiber's mechanical performance. The overall improvement in the mechanical properties of the treated fibers is therefore linked to the amount of crystallinity retained, as fibers with higher levels of crystallinity are stronger and stiffer [35].

I.10 Thermoplastic matrix

In composites, the matrix is important for blending and supporting the reinforcing fibers, applying loads, and giving strength to the material structure. It is in the form of a continuous phase that surrounds and suspends the fibers in such a manner that they are correctly oriented and positioned within the composite. By that, one of the major tasks of the matrix is to transfer external stresses to the reinforcing fibers, which are usually stronger and stiffer. As a result of this load transfer, the fibers are able to take the greater portion of the load, and in doing so, improve the mechanical performance of the composite [42, 43]. Furthermore, the matrix aids in the protection of the fibers from moisture, chemicals, sunlight, and other environmental factors which can deteriorate these materials over the time. It also increases the resistance of the composite to the impact or stress by

which fiber damage or failure can occur. The matrix is necessary to ensure that the fibers are able to perform as a single unit and not buckle or pull apart when stressed. Moreover, in thermosetting or thermoplastic composites, the matrix can enhance the overall thermal stability, dimensional stability, and processability of the material.

Thermoplastic is one of subclass of polymers that softens when heated, allowing it to be molded into shape, and hardens when cooled. These properties are a result of the polymers' long linear or branched chains that do not undergo a chemical change upon heating [44]. This process of heating and cooling is reversible, allowing thermoplastics to be reshaped as many times as desired. Because of such properties, these thermoplastics are highly versatile across numerous applications and industries. Unlike thermosetting plastics which undergo cross-linking between polymer chains resulting to laking the ability to remelted and reshaped, thermoplastics are usable throughout their lifecycle. These materials find usage in a broad range of industries, from packaging to the automotive industry, because of their low cost, ease of processing, and the ability to be reused or recycled. In composite materials, thermoplastics make excellent matrix materials because they increase the recyclability of the final product and allow for flexibility in processing.

I.11 Polylactic Acid (PLA) and its application

Polylactic Acid (PLA) is a compostable thermoplastic which can be synthesized from corn starch or sugarcane and is often labeled as a bio-based polymer. Some of the many claims for preferred attention are its benefits over traditional petroleum based polymer plastics which include a significantly smaller carbon footprint. PLA has a great tensile strength and stiffness enabling it to be an excellent matrix material for composites. Its moderate melting point and ease for processing allows different applications like 3D printing and biodegradable packaging to thrive. Even though PLA cannot handle extreme heat as some other thermoplastics, it does provide shelter to many sustainable material engineering constructs.

The PLA is widely used in various fields and applications due to its biodegradability, recyclability, and favorable mechanical properties, such as high tensile strength, stiffness, resilience and eco-friendly nature makes it an appealing option for many applications [45-49].

I.12 3D printing

I.12.1 History and Evolution of 3D Printing Technology

3D printing, or additive manufacturing, came into existence in the 1980s, and was first utilized for rapid prototyping. The first groundbreaking achievement in the field was made in 1984 when Chuck Hull, an American engineer invented stereolithography (SLA) a process by which UV lasers were used to convert liquid resin into a solid object by solidifying different layers. With this invention, we could create complex three-dimensional objects from fully formed digital models. This was the dawn of modern 3D printing technology.

With the development of other printing techniques in the 1990s, 3D printing technology continued to advance. For example, Selective Laser Sintering (SLS), which permits the fusing of powdered materials with the use of lasers, was developed in 1987 by Dr. Carl Deckard. This development increased the scope of materials that could be used. during this period fused deposition modeling (FDM) was invented by Scott Crump, the cofounder of Stratasys. This invention became one of the most prototyping methods for desktop 3D printing. Initially, these techniques were employed by industries to use them for prototyping, which helped companies save money and time in design and concept testing.

The 2000s marked the beginning of the democratization of 3D printing with the technology slowly moving from industrial sectors to consumer applications. This was made possible by the expiration of several key patents which allowed startups to innovate and build cheaper 3D printers. The RepRap project, started in 2005 by Dr. Adrian Bowyer, was central to this revolution. RepRap sought to design open source self-replicating 3D printers which made the technology accessible to a large number of individuals and small businesses.

By the 2010s, 3D Printing had penetrated several new markets including healthcare, aerospace, automotive, fashion, and construction. In biomedicine, 3D printing greatly impacted the production of custom-made prosthetics, implants, and even bioprinted tissues for engineering. In aerospace and auto industries, 3D printing saw the use in production of lightweight and durable parts by companies such as General Electric (GE) and Boeing for cars and airplanes to cut costs while enhancing performance. The technology also found application in architecture with

companies looking to build 3D printed buildings and other structures to cut down construction time and material waste.

The emergence of consumer version 3D printers, such as MakerBot and Ultimaker, propelled even further development of the technology by enabling individuals and small businesses to prototype, sculpt, and manufacture innovative items. The invention of new materials, including PLA, that are both biocompatible and biodegradable together with other materials like metals and ceramics, also increased the range of sustainable and high functional parts that could be produced.

The recent years have seen great changes in 3D printing, especially in the areas of speed, accuracy and diversity of materials. To be specific, multi-materail printing, metal 3D printing, and even bioprinting have opened up new possibilities in the manufacturing industry. The use of Artificial Intelligence and machine learning has also improved the design and printing strategies making the process more streamlined.

More importantly, 3D printing processes have moved from being a specialized instrument of rapid prototyping to a disruptive technology of various industries. It has changed the whole paradigm of production by supporting mass customization, reducing material waste, shortening supply chains, and enabling innovations that were previously thought to be impossible. As it continues to mature, the technology is expected to create even more possibilities which will be beneficial for medicine, aerospace, and eco-friendly production amongst other domains.

I.12.2 General Overview of 3D Printing

From virtual models, three-dimensional objects can be created using 3D printing or additive manufacturing. The process is unique as it constructs an object from the bottom to top layer by layer rather than cutting and drilling, this manufacturing method utilizes to construct objects and it is also able to manufacture objects that have intricate designs and complex structures [50].

The process goes through some significant phases. First, a model needs to be designed, in this case a digital model using computer-aided design (CAD). Next, the model is sliced into thin layers for the printer to follow while building the object. The most widely used technology for this is Fused Deposition Modeling (FDM). It uses thermoplastic filaments that are extruded through a nozzle to

create the layers of the object. Other methods do exist like Stereolithography (SLA), which uses lasers to solidify layers of liquid resin, or Selective Laser Sintering (SLS) which use lasers to melt powdered material into a solid object (**Figure I.6**).

As the technology in 3D printing keeps getting better over time, it is anticipated that it will significantly improve how things are made by allowing for greater manufacturing flexibility, spending less, and introduce new ways of designing and creating components.

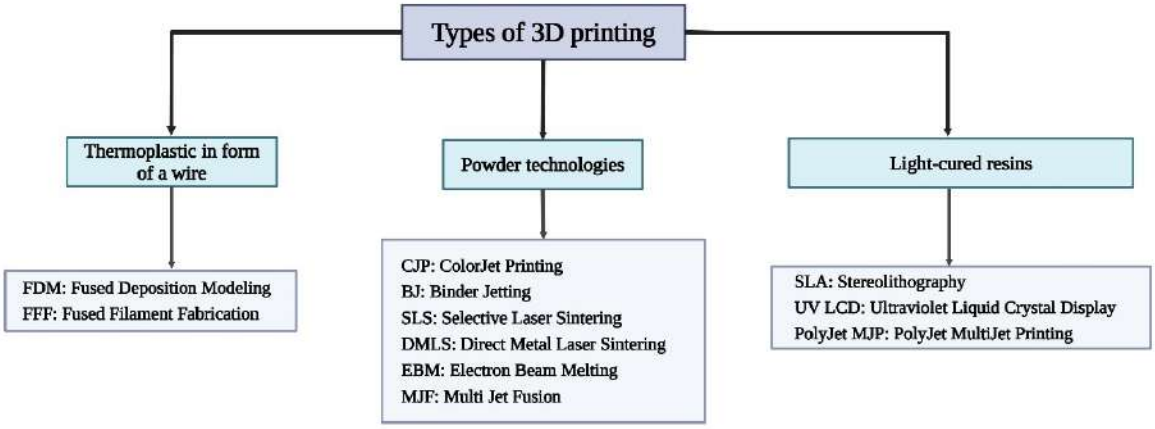

Figure I-6: Classification of 3D printing technologies and the main categories in each class [51].

I.13 Fused Deposition Modeling (FDM)

Fused Deposition Modeling (FDM) is a popular 3D printing method that is heavily utilized in desktop printers. Stratasys, a company specializing in 3D printing, developed this technology and patented it in 1989. After the FDM patent lapsed, it was adopted by various manufacturers who preferred to call it Fused Filament Fabrication (FFF).

I.13.1 FDM Process Fundamentals

- Techniques: The FDM technique involves communicating with the printer, which melts and deploys thermoplastic filament via a nozzle. A 3D object is manufactured by placing the melted filament in the desired shape on top of the previous filament layer. By moving the printer nozzle in the horizontal (X, Y) and then in the vertical (Z) direction (**Figure I.7**), each layer of filament is deposited as liquid and becomes solid after cooling.

- Material: Functional prototypes and components that are durable and useful can be manufactured with ease using FDM due to its variety of thermoplastic options such as Nylon, TPU, PETG, PLA, and ABS.

I.13.2 Advantages of Fused Deposition Modeling (FDM)

- Economical: FDM is one of the least expensive 3D printers and is therefore used by many individuals and small companies.
- The range of the material used: It has a very broad range of materials such as rigid and flexible thermoplastics.
- Ease of use: Operating an FDM printer is easy, and there is a large number of open sources FDM printers available.
- Use cases: FDM is generally used for making models, doing functional tests and small-scale production. It is also used in automotive, aerospace, and education industries.

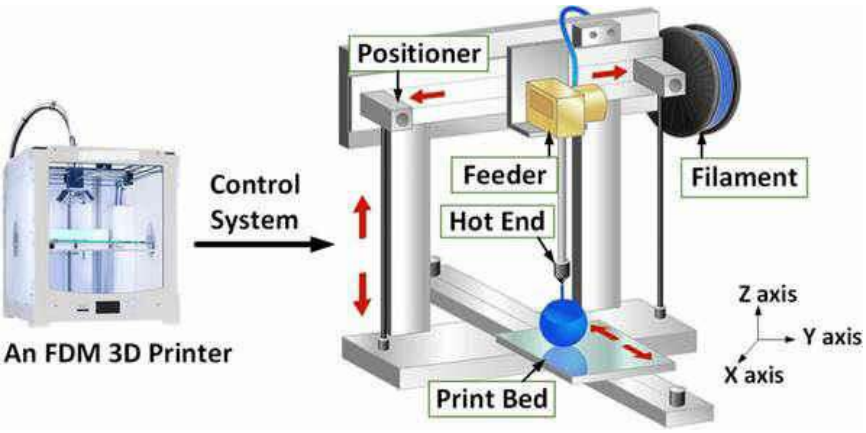

Figure I-7: The 3D printing process and the operating principle of Fused Deposition Modeling (FDM) [52].

I.13.3 Extrusion process for the production of three-dimensional printing filaments

The process of extrusion comprises the melting of PLA polymer pellets or granules into liquid, which is then formed into filaments (**Figure I.8**). These filaments serve as the raw materials for 3D print manufacturing. The process commences with the polymer granules being placed into an

extruder that is kept at an elevated temperature. After that, the polymer is shredded into smaller bits and then heated until it becomes a uniform liquid. After being homogenized, the plastic is released through a die of an appropriate size. Upon exiting the die, the filament undergoes a swift cooling process with water or air. This step entails solidifying the filament while ensuring it retains a consistent diameter. Subsequently, the filament is wrapped onto reels. The crucial parameter for the filaments is the diameter, as variances often result in inferior quality prints. This method of extrusion is very much applicable for the addition of various colorants or other fibers to reinforce the filaments for specific print materials.

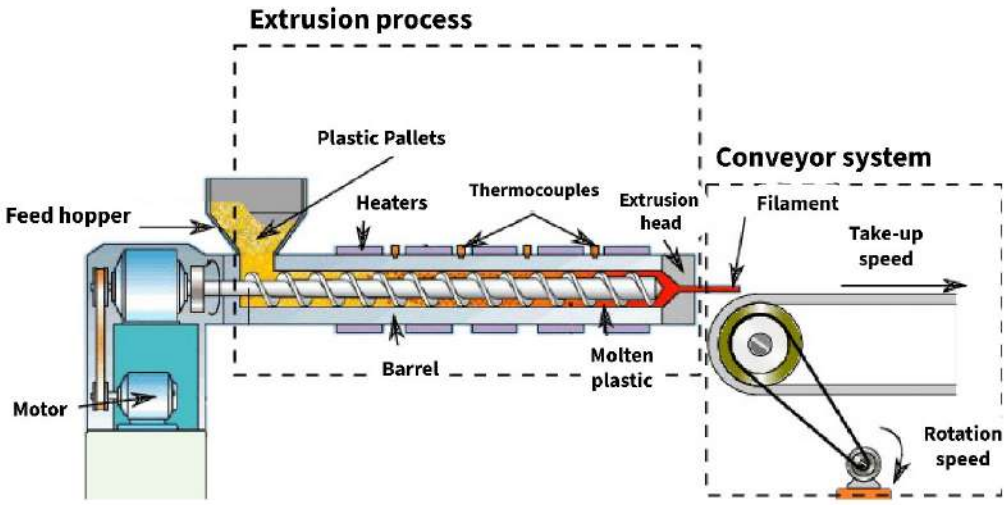

Figure I-8: Schematic of the Extrusion Process for the Production of 3D Printing Filaments [57].

I.14 Acoustic Emission

I.14.1 Presentation of the EA

Acoustic Emission (AE) [1,20] corresponds to a phenomenon of elastic energy release in the form of transient elastic waves within a material undergoing dynamic deformation processes. The elastic waves, of various natures and frequencies, propagate through the material before reaching its surface and may eventually undergo modifications. **Figure I-9** presents the EA acquisition chain. A material is subjected to mechanical stress and microcracks are created at the defects in the material. Transient elastic waves are thus created. The waves are collected at the surface by

piezoelectric sensors, they are amplified and provide the acoustic emission signal. This technique allows for real-time detection of damage evolution in a material. It is a non-destructive technique that does not require an excitation signal.

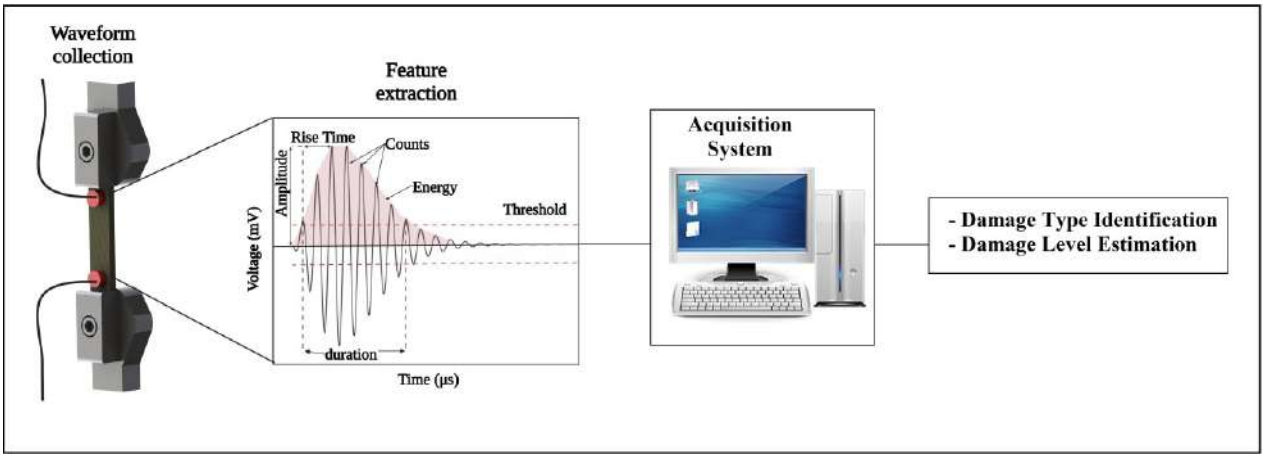

Figure I-9: Acoustic Emission Measurement Setup.

There are two types of EA:

- Discrete acoustic emission: the AE signals generated depend on the sensors used: damped sinusoids (bursts) in the case of resonant sensors, short impulses in the case of wideband sensors.
- Continuous acoustic emission: when the signals are frequent and overlap, it is not possible to separate them into bursts. It is mainly observed in metallic materials (plastic deformation).

The sources of EA are related to irreversible phenomena in the materials. For composite materials, the main sources of EA are attributed to the damage mechanisms presented earlier or to friction phenomena. However, many physical phenomena can be sources of EA:

- Plastic deformation, dislocation movement, fractures of inclusions or metallic compounds.
- Initiation and propagation of cracks (static stress, fatigue, etc.).
- Hydrogen embrittlement, corrosion.
- Micro and macroscopic fractures in composite materials.
- Friction, mechanical impacts.
- Leaks (liquid and gas).
- External noises (traction machine, jaws, etc.)

I.14.2 Kaiser Effect and Felicity Report

The Kaiser Effect (KE) reflects the irreversibility property of the phenomena responsible for the generation of AE waves. It is defined as the absence (or low presence) of EA when a material subjected to a stress level P_1 and then unloaded does not emit or emits little as long as the stress, applied during a second loading, remains below the previously reached maximum value P_1. The level of stress at which EA appears during the second loading is called P_2. If the material is damaged between two consecutive loadings, then $P_2 < P_1$.

The Felicity ratio (Rf) which allows for the quantification of EK is defined by:

$$R_f = \frac{P_2}{P_1}$$

If the material has been damaged, then $R_f < 1$. Generally, the Kaiser effect is more respected by metallic materials without evolving defects than by viscoelastic composites, which obey temporal evolutions of deformations likely to be reproduced under constant stress.

I.14.3 Method of Acquisition of EA Signals

Transducers used for EA

The transducers used to capture elastic waves on the surface of a material are of piezoelectric nature. The coupling on the surface of the material is done using silicone grease. The role of the coupling is to improve the transmission of waves between the surface of the sample and the transducer.

EA acquisition chain

In this study, an EA data acquisition system from (MISTRAS, USA) is used with two acquisition channels. The detected EA signals are amplified using two 40 dB gain preamplifiers. They are then sampled at a sampling frequency of 4 MHz. The signals are recorded by the acquisition system for further processing. An acquisition threshold of 35 dB was used, set slightly above the background noise to eliminate it.

The acquisition system is calibrated before each test using a mine break procedure [58, 59],allowing the generation of reference sources of elastic waves simulating the EA. These sources are created in the area of the sample between the two EA sensors. It is then sufficient to verify the

correct location of the created sources and adjust the arrival time of the pulses if necessary using the propagation speed (the propagation distance being known).

We also verify that the characteristics (amplitude and energy) of the signals received by the AE sensors as a function of the source-sensor distance remain constant, ensuring that the attenuation of the waves in the material is not too significant. This test thus allows for the localization of EA sources, estimation of propagation speed, and evaluation of acoustic wave attenuation in the material. For the tested specimens, the attenuation remains negligible, with a loss of less than 3 dB for the sensor-source distance.

Configuration of the acquisition software

The EA software requires configuring the acquisition of bursts. The PDT (Peak Definition Time), HDT (Hit Definition Time), and HLT (Hit Lockout Time) are time windows used to define, respectively, during the acquisition of a signal, the peak of the highest amplitude, the total duration, and the lockout time (**Figure I-10)**.

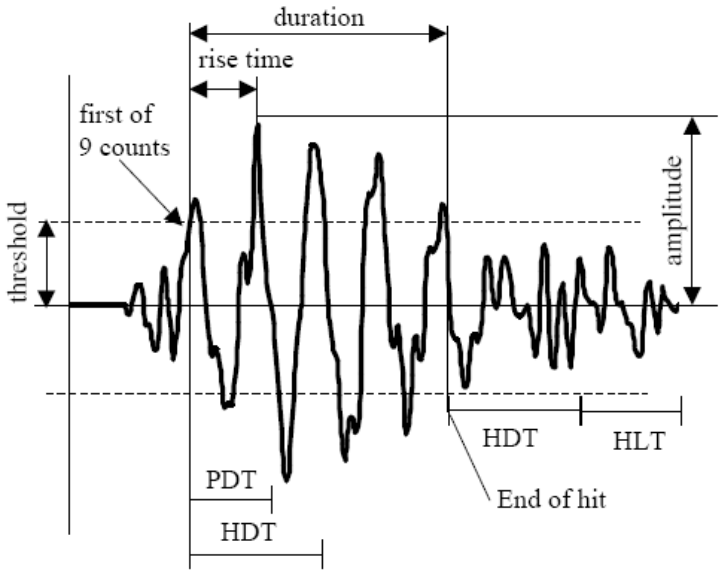

Figure I-10: Acquisition parameters of AE bursts: PDT (Peak Definition Time), HDT (Hit Definition Time), and HLT (Hit Lockout Time) [60].

I.15 Impulse Excitation Technique (IET)

IET can be broadly defined as the method which measures elastic characteristics such as elastic modulus of materials. This method is widely known as a nondestructive technique. To conduct this method, the sample is impacted with a mechanical impulse which excites vibrations within the sample. These vibrations are emitted as resonant frequencies and are further processed to find the elastic modulus of the material [61, 62]. IET is efficient for evaluating the material without damaging the simples and therefore can use it for the examination of Lygeum spartum/PLA and neat PLA specimences.

IET was utilized in this case study for the elastic modulus of specimens. The setup involved the clamping of samples and the application of a mechanical impulse in order to excite their natural frequencies as shown in **Figure IV.3**. Subsequently, a microphone detected the resulting vibrations. The elastic modulus was determined from the known dimensions and mass of the samples as well as the calculated resonant frequencies of the material.

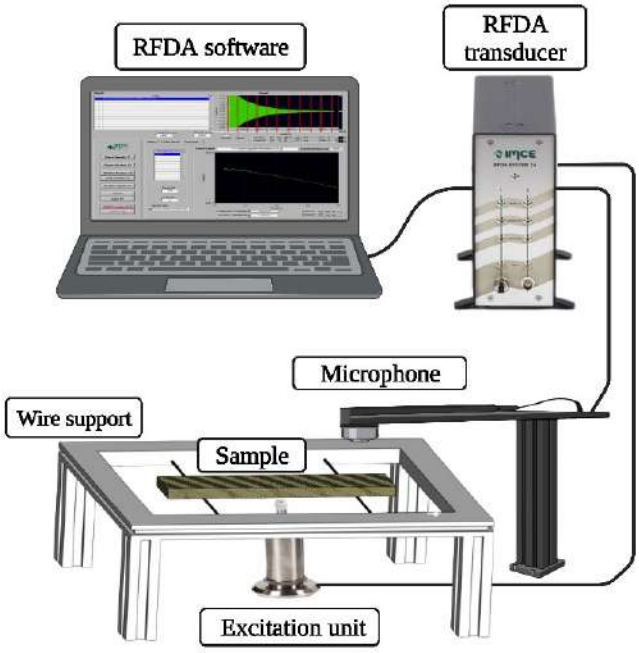

Figure I-11:schematic represents the setup for impulse excitation technique.

I.15.1 Working Principle of IET

- Mechanical Excitation: An impulse, either a tap or a strike, is made to the sample and is sufficient for inducing natural oscillations. The specimen is excited and vibrates freely generating oscillations as a function of its material properties.
- Measurement of Vibrations: the natural vibrations of the sample is measured with aid of a sensor (e.g., microphone or accelerometer) capturing the specimen's resonant frequencies.
- Resonant Frequency: The frequency at which the specimen vibrates and oscillates is established. This frequency is a factor of the specimen's geometry, mass and stiffness.
- Calculation of Elastic Properties: Using known mass and dimensions of the sample, and recording the resonance frequency of the sample, the elastic and shear moduli are calculated by using the known mathematical formulas.

I.15.2 Mathematical Framework

The Young's modulus (E) was calculated using the following formula for rectangular beam shaped specimens like the examined 3D Printed samples:

Where:

$$E = 0.9465.\frac{f_r^2.L^3.m}{4.h^3}$$

E: Young's modulus (GPa)

L: length of the specimen (m)

b: width of the specimen (m)

h: thickness of the specimen (m)

f_r: fundamental resonant frequency (in Hz)

m: mass of the specimen (kg)

The shear modulus (G) was calculated using the following formula with the obtained relationship between Young's modulus and Poissons ratio (ν):

Where:

$$G = \frac{E}{2(1+\nu)}$$

G: shear modulus (GPa)

ν: Poisson's ratio (material-specific constant)

This technique is of particular benefit with regard to the evaluation of 3D-printed specimens as it permits estimating the impact of factors such as layer bonding, orientation of the print, and fiber reinforcement on the mechanical properties of the material. IET can also reveal how the elastic behavior of the printed specimen's resonant structure depends on the printing parameters, as the resonance frequencies are a function of the specimen's internal structure, which in this case is the neat PLA and its L.S biocomposite.

I.16 Conclusion

This chapter has presented the latest developments of natural fiber composites in terms of their use and relevance in the industry owing to environmental and economic factors. The use of natural fibers, especially from plants, has great potential in the reinforcement of polymers because of improved mechanical and sustainable properties of the materials. However, fiber-matrix compatibility and durability over time still pose significant challenges to be solved. In many existing studies, the possible applications of these composites in industries such as automotive, construction, and even aerospace have been discussed. These discussions are what guide the current study aimed at determining the effectiveness of Lygeum spartum L. fibers in making sustainable and innovative biocomposite materials.

Chapter II

Materials and Experimental Techniques

II.1 Introduction

In this chapter, we describe the materials and experimental methods that were employed. The work concentrates on the design and analyses of Lygeum spartum L. plant fibers reinforced PLA biocomposite. Several methods were used to evaluate the physical and mechanical properties of the biocomposite, including mechanical testing methods, such as tensile and flexural tests, to evaluate strength and elasticity as well as non-destructive methods such as acoustic emission (AE) monitoring, mechanical impulse excitation, and digital image correlation (DIC) to measure fields of displacement and strain. while thermal and chemical analyses were conducted using thermogravimetric analysis (TGA) and Fourier transform infrared spectroscopy (FTIR) These measurements and methods, together with the other non-destructive techniques enable us to understand the effect of different factors on the performance of the biocomposite.

II.2 Mechanical extraction and chemical treatments of the fibers

The biocomposite is reinforced with Lygium spartum fibers for which, in this research, mechanical and chemical techniques were applied for the achievement of the final desired fibers. The process started with a plant's mechanical extraction, where the stalks of the harvested plant underwent a retting process to dissolve and disintegrate the untouched fibrous components. Finally, the fibers were isolated by crushing and decortication through mechanical separation.

After following the mechanical extraction procedure, the treating of fibers chemically was done by means of a sodium hydroxide (NaOH) solution in a concentration of 5%. In a span of 120 minutes, the fibers were submerged into the NaOH solution which provided sufficient duration towards dissolving the non cellulosic components of the fibers, such as lignin, hemicellulose, and other impurities. Not only did this treatment clean the fibers, but increased the surface roughness of the fibers enhancing their compatibility with the PLA matrix. After the soaking duration, the fibers were washed and rinsed with water several times to remove the residual NaOH. The importance of this rinsing process is to mitigate any consequences of the leftover chemicals on the fiber properties or the interaction of the fiber and matrix in the finished biocomposite material.

After cleaning, the fibers were dried and made ready for subsequent experiments.

II.3 Preparation of the reinforcement fiber

In order to achieve the right fiber size for 3D printing technology, the fibers were subjected to a crushing and a sieving procedure. A common concern with FDM/FFF 3D printers is the nozzle diameter range of 100 to 600 µm. It is important to note that the fibers must be smaller than 100 µm, preventing the clogging of the nuzzle during the printing process. These concerns demonstrate the necessary to employ a size reduction technique which has multiple sequential stages.

The first stage of the size reduction procedure included drying the fibers in an oven at 80 C° for two hours. Any remaining moisture was removed and because of this step, the subsequent mechanical processing step can be performed without concern. It is important that the fibers are dried or it could lead to clumping and poor grinding as well as lower the bonding strength with the polymer matrix.

After drying, the next step consisted of mechanical crushing utilizing a rotary grinder (**Figure II.1**). This step, the grinding process, enables bulk fibers to transform to lower bulk fragments. These fragments were then subjected to high-speed mechanical rotation, which enables the further breakdown of the fragments to particle sizes small enough to pass through the sieves.

Figure II-1: Laboratory Grinding Machine Used for Fiber Milling.

The fibers were classified by size using a multistage Fritsch sieve system after the grinding process (**Figure II.2**). This fiber sieving method required crushing the fibers into smaller pieces and screening them with larger mesh sizes until a limit of 50 to 100 µm was achieved. Reduced fibers greater than the designated size were returned to the grinder for further size reduction. This measure provided uniformity needed in the packing of the fibers which are very vital for 3D printing nozzle free of clogging and ensuring adequate dispersion within the polymer matrix.

Figure II-2: the fritsch sieve used for separation between deferent fibers size.

The meticulous processing enabled the necessary fiber dimensions are acquired for a biocomposite material used in 3D printing. The proper selection of fiber dimensions improves the printability of the biocomposite and the mechanical properties of the parts printed. The fibers obtained are shown in **Figure II.3**.

Figure II-3: Prepared Short Lygeum spartum L. Fibers After Extraction, Chemical Treatment, Grinding, and Sieving Processes, Ready for the Preparation of L.S/PLA Biocomposite Granules.

II.4 Preparation of biocmposite granules

Commercial PLA 4043D was dissolved in a chloroform solution ($CHCl_3$, 99.0-99.4%) from Honeywell Riedel-de Haen (Muskegon, MI, USA) using a Polymer to liquid Ratio of 1:9 in order to prepare the biocomposite granules for use in 3D printing. The selected PLA 4043D, is a commonly utilized biodegradable polymer supplied by Nature Works, USA that has a density of 1.24 g/cm³, a molecular weight of 110,000 g/mol, and melting temperature of 145-160°C. These attributes render it suitable for biocomposites since it provides mechanical strength and has environmental advantages.

While holding the temperature constant at 30 °C, to ensure that polymer completely uniforms into supper, the PLA and chloroform mixture was stirred on a magnetic stirrer at 900 rpm (**Figure II.4**). This step was very important because it was necessary to achieve a homogenous liquid phase to allow effective mixing with the reinforcing fibers. Speeding up or reducing the stirring rate is also detrimental as it may cause the PLA to partially or fully crystallize or separate the phases too early, both of which have negative outcomes on the quality of the biocomposite.

As soon as a distinct and homogeneous solution was achieved, a short Lygium spartum fiber were added incrementally. Control over thickening and allocation was put in place by incorporating low and steady quantities of fibers. This was done with the aim of having a concentrated amount of 10 wt % in the PLA matrix. The targeted reinforcement level was reached to enhance processability

and mechanical properties, enabling smoother 3D printing. After incorporating the fibers, the solution was further mixed to allow for superior blend uniformity and proper alignment of the fibers with the PLA matrix. Subsequent to completing fiber-reinforced PLA, the solution was dried and milled into granules that could be extruded and used for 3D printing. The procedure followed during fiber solutioning enabled uniform distribution which is very essential for part performance once printed.

Figure II-4: Preparation of Biocomposite Granules by Dissolving PLA, mixing with 10 wt% Lygeum spartum Fibers, and Drying the Mixture into Sheets, Followed by Cutting to Obtain Biocomposite Granules.

II.5 Extrusion Process

A custom-made mini extruder was built specifically for the requirements of biocomposite extrusion and as such, the extrusion process was performed on it (**Figure II.5**). The machine was modified with features that enabled it to meet the challenges of composite material processing. The machine employs two independently controlled zones for heating, which leads to accurate temperatures during the extrusion process. The machine is powered by a 1 kw asynchronous electric motor and has a 1.5 kw power supply for the electric speed control which helps in providing faster speeds with high torque. This enables the machine to operate efficiently. A

gearbox of 1:50 ratio is used to increase the torque available at the main screw so that efficient extrusion can happen even at high-torsion conditions.

The extrusion process is carried out with the main screw made from Z200 high strength steel for better strength and durability. It is manufactured with a diameter 30 mm and a pitch of 22 mm so that optimal performance is offered. The nozzle of the extrusion head is manufactured with a diameter of 1.9 mm, which allows for the extrusion of materials with sufficient pressure to avoid blockages. For the drawing process, an automatic diameter adjustment system was implemented, which enables control over the extrusion speed, and maintains the uniformity of the final product. These specifications ensure the reliability of the biocomposite extrusion.

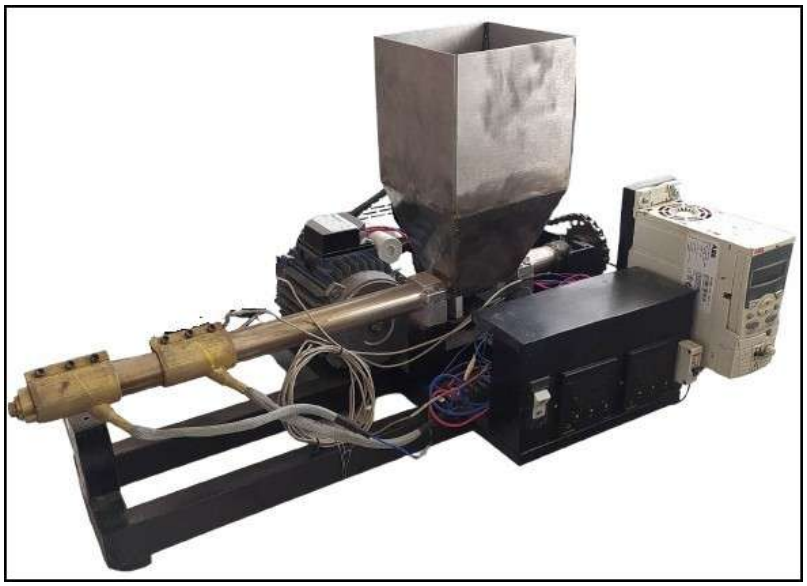

Figure II-5: Custom-Built Mini Extruder for the Production of Biocomposite and Pure PLA Filaments.

II.6 Production of Neat and Composite Filaments for 3D Printing

In order to obtain an accurate comparison between the performance of biocomposite filaments and neat PLA filaments, both types need to be manufactured under similar conditions. For consistency, neat PLA filaments were produced using the same grade of PLA, Ingeo 4043D, as was used to produce the biocomposite filaments, making it possible to evaluate the impact of the fiber reinforcements on the mechanical and thermal properties of the filaments more directly.

Both the neat PLA filaments and fiber-reinforced biocomposite filaments were produced by using PLA 4043D granules, which are known for being biodegradable and having good mechanical properties, as the primary polymer matrix. The extrusion process involved using a custom built mini extruder which was initially meant for biocomposite production. Such a setup was prepared in order to control the dimensions and production parameters of the neat PLA filaments. This standardization enables accurate evaluation of changes in filament performance in relation to printability, strength, and thermal behavior.

The resulting neat PLA and biocomposite filaments are shown in **Figure II.6**, where their uniformity and quality known to be achieved by optimized extrusion is illustrated. Abiding by the same processing conditions, the differences between neat PLA and biocomposite filaments will be useful in determining the effects which fiber reinforcement has on overall material performance in 3D printing.

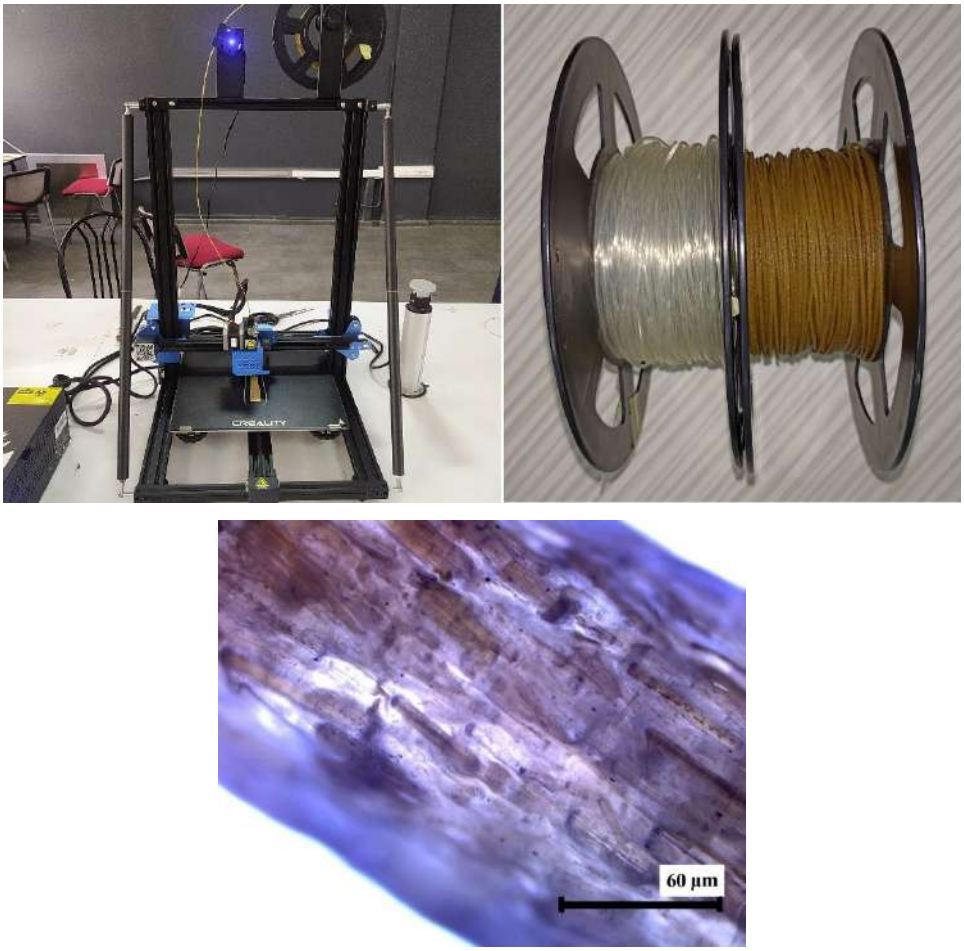

Figure II-6: Neat PLA and Biocomposite Filaments Produced via Extrusion Process, The alignment of the fibers in the biocomposite filament and Their Subsequent Use in 3D Printing.

II.7 Printing of Tensile and Flexural Specimens

In order to evaluate the mechanical characteristics of the new biocomposite, tensile and flexural test specimens were printed in accordance with the standard procedures of the ASTM system (**Figure II.7**). The sample for the tensile tests were constructed with respect to the dimensions of ASTM D638 [63], having a length of 165 mm, a height of 3.2mm, and a width of 13mm (L × H × W). Likewise, for the flexural tests, the prints were done according to the requirements of ASTM D790 [64], with a length of 80 mm, height of 3.2 mm and width of 13 mm.

The parameters for all samples were kept constant to ensure similar layer adhesion and material deposition between layers so as to reduce differences in the mechanical performance of specimens due to the printing parameters. Print speed, nozzle temperature, layer height, and the percentage

of infill, the printed samples underwent mechanical testing to determine tensile and flexural strength and other relevant properties. Such accuracy is required to make comparative analysis of the biocomposite with neat PLA and other reference materials.

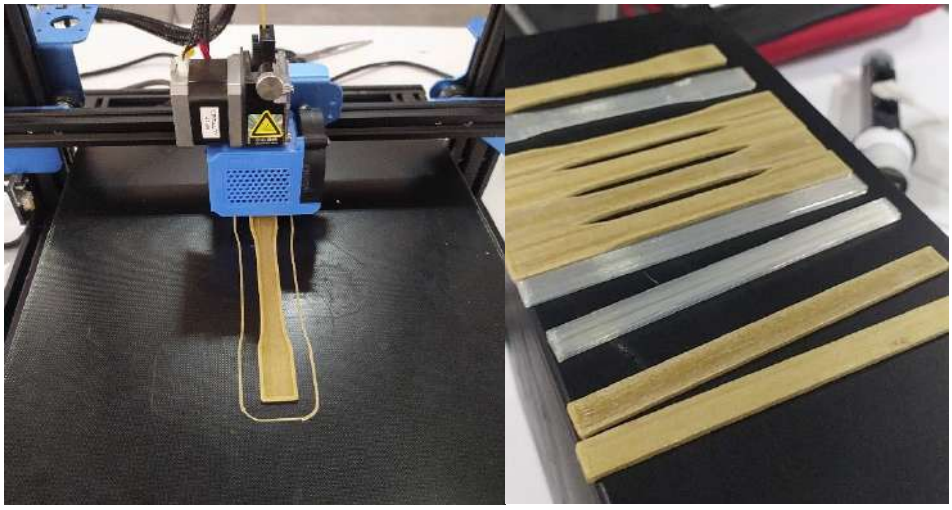

Figure II-7: 3D-Printed Tensile and Flexural Specimens of Neat PLA and L.S/PLA Biocomposite.

II.8 Tensile and flexion tests

The mechanical properties of the biocomposite in comparison to the neat PLA materials are evaluated by performing tensile and flexural tests at room temperature with an Instron LM-U150 electromechanical testing machine which is outfitted with 50 kN load cell (**Figure II.8**). The tensile tests were carried out according to ASTM D638, at a crosshead speed of 1mm/min. In the subjected samples, strain was measured from an attached 55 mm extensometer. Flexural tests were conducted according to ASTM D790 by means of two bending positions with a support span of 50 mm. In order to assess the flexural strength of the specimens, a crosshead speed of 2.5 mm/min was used. Each sample underwent the same test set four times to achieve reliable and valid data to enable average values of both obtained tensile and flexural values. This rigorous procedure of testing gives a comparison of the mechanical properties of the biocomposite to the neat PLA.

Figure II-8: Universal Testing Machine in Operation During Mechanical Testing.

II.9 Porosity and density measurements

For the measurements of the porosity and density of the fibers, biocomposite, and the neat PLA, a Micromeritics helium pycnometer ACCUPYC 1340 was utilized (**Figure II.9**). The analysis gas used in these devices is helium, which ensures a precise measurement of volume followed by density evaluation of the materials. The tests were performed at room temperature so that all the samples were taken under similar conditions. To improve the quality of the results, every measurement was performed 10 times for each material. The Helium pycnometer made by Micrometritics has high repeatability, which makes it possible for a detailed degree of assessment of the porosity and density of the neat PLA, biocomposite, and the reinforcing fibers. These values are particularly important in order to appreciate the mechanical properties of the material and the way it acts during the 3D printing process.

Figure II-9: Pycnometer Used for Porosity and Density Measurements.

II.10 ATR-FTIR Analysis

A Shimadzu IR Tracer 100 was used in conducting the Fourier Transform Infrared (FTIR) spectroscopy. As illustrated in **Figure II.10**, FTIR was used scanning from 600 to 4000 cm^{-1} with a resolution of $4cm^{-1}$ in attenuated total reflectance (ATR) absorbance mode, PLA, fiber samples and biocomposite were examined on their functional groups and analyze the chemical composition and molecular structure of the materials. This technique provided crucial insights into the chemical interactions between the PLA matrix and the reinforcing fibers, contributing to a better understanding of the bonding mechanisms and material properties.

Figure II-10: Shimadzu IR Tracer 100 Equipment Used for FTIR Spectrum Analysis.

II.11 Thermal Analysis

The thermal behavior of the samples was conducted using a TA Instruments SDT-Q600 (**Figure II.11**), which incorporates both the thermogravimetric analysis (TGA) and differential scanning calorimetry (DSC). The assessment was done from room temperature (25°C) to 600°C at a 10°C/min increase rate in temperature in order to observe the thermal stability and the decomposition of the materials. 6 mg of each sample were tested while applying nitrogen gas at a rate of 20 ml/min in order to avoid oxidation. The combination of weight loss and heat flow associated with subtype decomposition along with phase transitions in the neat PLA, biocomposite and L.S fiber were analyzed resulting in proper understanding of the thermal properties such as stability of the material.

Figure II-11: TA Instruments SDT-Q600 Used for Thermal Analysis.

II.12 Morphology Characterization

A Hitachi S-4800 field emission scanning electron microscope (FESEM) was used to analyze the samples' microstructure. The observations were done at an accelerating voltage of 15 kV to obtain finer details of the fracture areas. From both the tensile and flexural test specimens, an x20 to x100 magnification range acquired through the microscope enabled high-resolution images of the fracture surface. The microstructural analysis was performed on the neat PLA samples as well as the biocomposite ones to determine the fiber-matrix interaction, fiber distribution, and the damage mechanisms. These observations provided an understanding of fiber reinforcement effect on the mechanical properties and failure modes.

II.13 Impulse Excitation (IE)

To determine the natural frequency of the flexural samples, the IMCE system of impulse acoustic excitation (IMCE, Belgium) was used, which is also used to derive their Young's modulus (**Figure II.12**). This process is in accordance with the rules established in ASTM E1876, which enables measurement of elastic properties such as Young's modulus and Poisson's ratio on the basis of the resonance frequencies that have been measured. The impulse excitation technique is non-destructive and highly accurate, making it possible to measure the elastic parameters of materials with ease, which in this case includes both neat PLA and the biocomposite specimens.

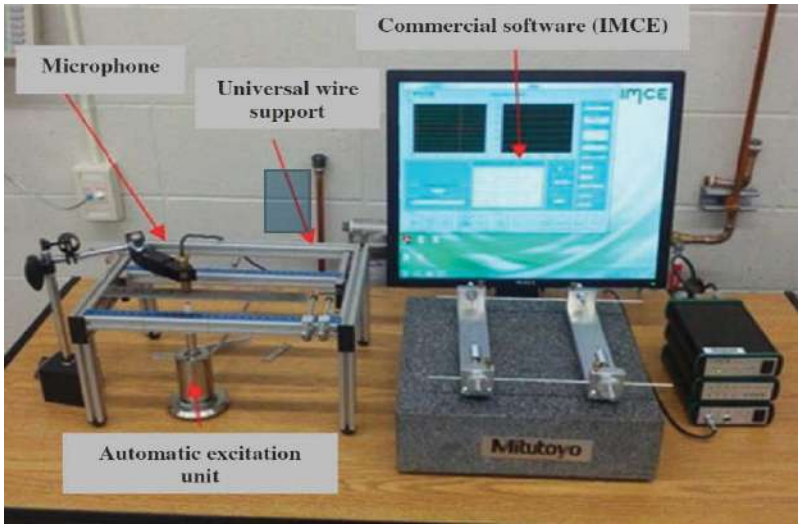

Figure II-12: impulse excitation technique setup.

II.14 Digital Image Correlation (DIC)

A two-dimensional (2D) image correlation system (StrainMaster, LaVision Inc.) was used to track the displacement as well as the surface strain fields of the specimens (**Figure II.13**). The system had a CCD camera with sensor size of 7.2 x 5.4 mm² and a video frame rate of 1 frame/second with a resolution of 1628 x 1236 pixels, The GOM Correlate Software was used for the post-processed results. scanning step and digital gauge set at 10 pixels each to ensure the accurate correlation of displacement measurements. Once the displacement field was determined, the strain field was calculated, which, in turn, allowed a detailed analysis of deformation across the surface of the specimen during testing.

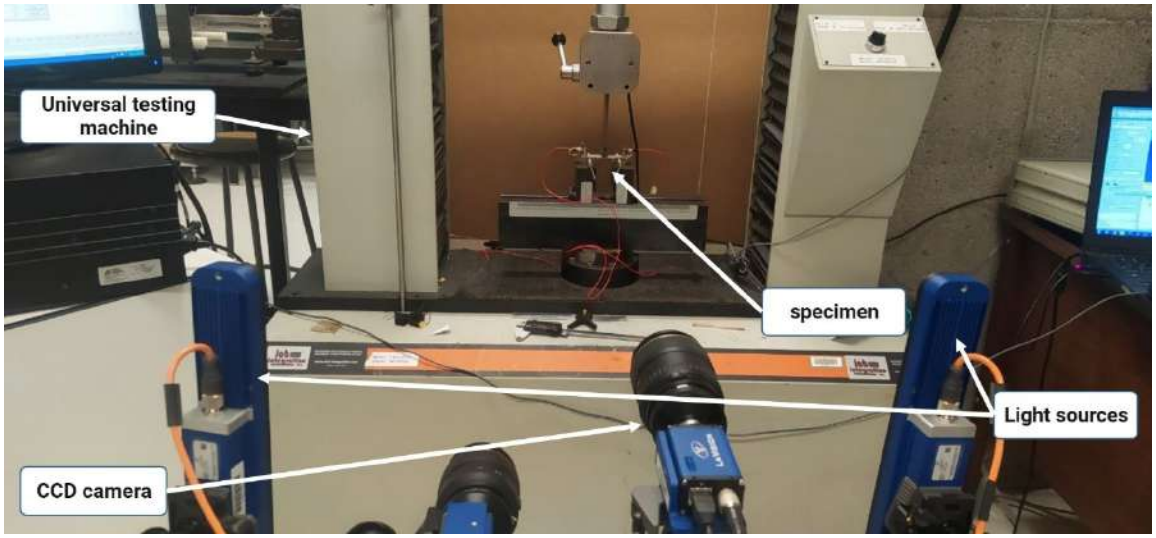

Figure II-13: Digital Image Correlation Setup for Capturing Displacement and Deformation Fields.

II.15 Acoustic Emission (AE) Signals

Acoustic emission signal were recorded using a MISTRAS data acquisition device obtained from Physical Acoustics Corporation, with two channels and 4 MHz and a 40 dB of pre-amplification. This device was connected to two MICRO-80 sensors, with frequency of 100-1000KHz operating range. The AE signals were captured using the sensors which are subjected to surface of the specimens which were fixed using clamps and silicon grease for effective coupling (**Figure II.14**). To avoid other interference, background noise was filtered with a threshold setting of 35 dB. Other system parameters were: peak definition time was 50 µs, hit definition time was 150 µs, and hit

lockout time was 300 µs. To calibrate the coupling and AE source location, three pencil lead break tests were conducted prior to all tests.

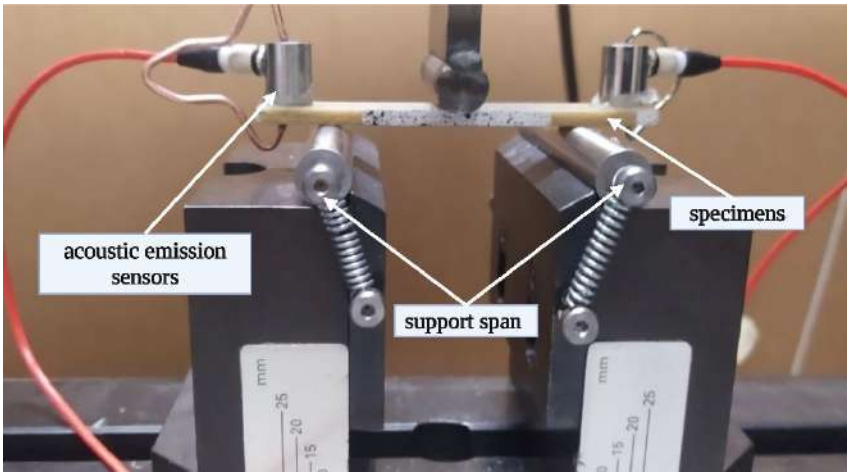

Figure II-14: Acoustic Emission Setup During Flexural Testing.

II.16 Reverse engineering of gears model using neat PLA and Lygeum Spartum/PLA biocomposite

In this study a reverse engineering was conducted to design and manufacture a gear from neat PLA and Lygeum spartum/PLA biocomposite filaments (**Figure II 15**). The process of developing this gear entailed studying and reproducing the geometry and functionality of a reference model. It was possible to identify critical design parameters in reverse engineering, such as gear dimensions, tooth shape, and pitch, converting them into a CAD model that was used for 3D printing. this illustrating the practical uses of the biocomposite material in the 3D printing, these approaches allow for the comparison of the two filaments in terms of printability, appearance and the strengths of the printed parts. The biocomposite material marks a step toward the engineering of sustainable components as the strength and toughness of the material are crucial for its functions alongside its low environmental impact.

This comparison shows that the L.S/PLA biocomposite provides mechanical benefits relative to neat PLA, and also surpasses it in print and aesthetic finish quality. Hence, L.S/PLA biocomposite appears to be a very suitable alternative for 3D printing applications with finishing requirements.

Figure II-15: a gear model printed from neat PLA end biocomposite.

II.17 Conclusion

This chapter discusses all material treatments and experimental techniques carried out for investigating the Lygeum spartum L. fiber-reinforced PLA biocomposite. The mechanical characterization methods, namely tensile and flexural testing, along with non-destructive techniques such as acoustic emissions (AE) and digital image correlation (DIC), provided important insight into the material behavior. Further, thermal and chemical examinations using TGA and FTIR were carried out to characterize the properties of the biocomposite. This combination established the basis for a detailed investigation of biocomposite behavior, enhancing the understanding of possible applications and performances under various exposure conditions.

Chapter III

Physicochemical and Thermal Characterization of Lygeum spartum/PLA Biocomposite

III.1 Introduction

The primary focus of this chapter is the analysis of physicochemical and thermal properties of the Lygeum spartum/PLA biocomposite made in this work. The knowledge of the material properties such as chemical, physical as well as the thermal attributes are necessary in order to evaluate the material in different application setups. The chapter proceeds with porosity and density measurement and then with an FTIR, where the chemical composition of the fibers and the biocomposite is analyzed to ascertain the functional groups present and the level of fiber-matrix interactions. Fiber-matrix interactions are critical for the mechanical properties. Furthermore, the microstructure and surface morphology are investigated using scanning electron microscopy (SEM) that they serve an important aspects of fiber dispersion and fiber-matrix bond strength in the PLA matrix.

TGA and DSC are also important techniques in the evaluation of the materials regarding their thermal characteristics like thermal stability, degradation behavior, and crystallinity. Such analyses are important in estimating the practicality of thermal sensitive processes. These physicochemical and thermal parameters are essential in forming an indicative framework for the material properties evaluation and merits for industrial applications.

III.2 Porosity and Density

The porosity and density profile for Lygeum spartum fibers, neat PLA, and Lygeum spartum/PLA biocomposite were evaluated and compared (**Figure III.1**). The fibers showed maximum density of 1.66 g/cm³ which is normal for plant based fibers [65]. On the other hand, the biocomposite had lower density of 1.24 g/cm³ as compared to neat PLA which was 1.27 g/cm³. This reduction in density for the biocomposite is likely the result of imperfect bonding that occurs between the hydrophilic fibers and hydrophobic PLA matrix [66], resulting in voids within the material. In addition, due to the random orientation and distribution of short fibers within the composite, more gaps were created within the polymer matrix.

The 3D printing process itself generates formation of voids because it’s easier for air pockets to develop in the rough surfaces between printed layers, in contrast to other manufacturing processes such as injection molding, which indeed has smoother surfaces and therefore carries a lower

probability of void formation. The porosity measurements further substantiated this, with fibers having the highest porosity value of 39.87 %, followed by neat PLA at 21.41 %, and the biocomposite demonstrating slightly lower porosity at 19.91 %. The porosity value in the biocomposite is reduced because of the irregularity of the extruded material [67], which filled some of the voids formed between the layers, as the SEM images revealed. These images showed larger triangular voids in the neat PLA samples but significantly smaller or almost no voids in the biocomposite. Even though air bubbles did occur in the biocomposite samples, they are less significant to the overall porosity than the voids visible in the neat PLA specimens.

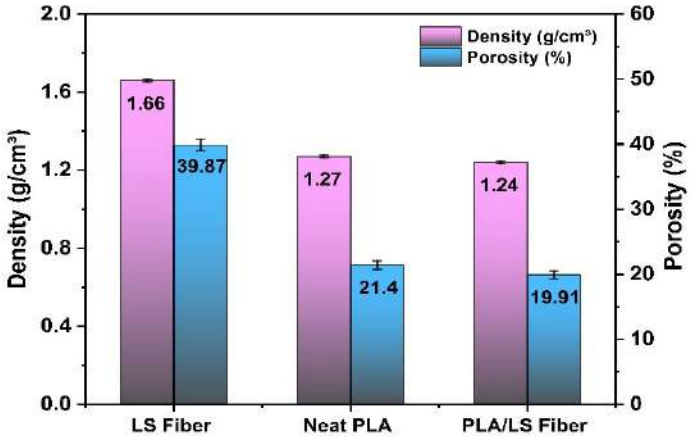

Figure III-1: porosity and density of L.S/PLA biocomposite, pure PLA, and L.S fibers.

III.3 FTIR Analysis

FTIR offers great potential and application in the specific fields of materials science for the chemical structure characterization because it is possible to identify functional groups and interpret the bonding of molecular structures in the sample. In the case of composite materials such as Lygeum spartum/PLA biocomposite, FTIR allows fonding the relation between the polymeric matrix and the reinforcing fibers. By detecting the mainly absorbed wavelengths of infrared light, infrared spectroscopy measures the free vibrations caused by the energetic transition of the chemical bonds in the material and subsequently generates a spectrum that corresponds to the bearers of the vibrational modes. This process is critical in acquiring the image of chemical interactions in the matrix and the fibers as they strongly affect the mechanical, thermal, and performance characteristics of the composite. In addition, the FTIR analysis allow us to see the

alteration of polymeric chemical PLA into other chemical structures after the introduction of fibers which explains the how the incorporated fibers change the properties of the material.

The FTIR spectra of L.S fibers, PLA and Lygeum spartum/PLA biocomposite are provided in **Figure III.2**. by analyzing it we can observe that the major peaks agree with the previously conducted studies [7, 68]. We noted that in the spectrum of neat PLA, the stretching vibration of the carbonyl (-C=O) had a peak of 1747 cm^{-1} whereas, the asymmetric and symmetric vibrations of C-O-C bonds had peaks of 1080 cm^{-1} and 1040 cm^{-1} respectively. the C-O bending peak is 1180 cm, as well as the C-H characteristic peak are found at 2997 cm^{-} and 2949 cm^{-} respectively. For Lygeum spartum fibers, a peak around 3340 cm is associated with -OH which is attributed to the stretching vibrations of hydroxyl groups. -CH_2 groups present in cellulose and hemicellulose had a peak of 2916 cm. Peaks of 1734 cm and 1637 cm are associated with the carbonyl (C=O) groups whereas C=C bonds found in lignin have a weak peak of 1531 cm. The absorption peak near 1039 cm is an indicator of C-O stretching vibrations in cellulose [69-71].

The incorporation of L.S fibers to PLA polymer matrix is confirmed by the presence of -OH peaks at around 3340 cm^{-1} in the FTIR spectrum of Lygeum spartum/PLA biocomposite. These peaks are absent in the neat PLA spectrum. The composite spectrum also displays key carbonyl stretching at 1747 cm^{-1} and the C-O-C stretching at 1082 cm^{-1} [69].

It is however important to understand that there is an observable reduction in the biocomposite's C=O stretching peak within the FTIR spectrum relative to neat PLA [72]. This reduction suggests some interaction between the L.S fibers' hydroxyl structures and the PLA polymer's carbonyl structures, confirming at least partial bonding or interfacial adhesion between the polymer matrix and fiber reinforcements. These changes illustrate that some interactions do exist but the overall chemical structure of the composite, including the position of characteristic peaks, are well preserved.

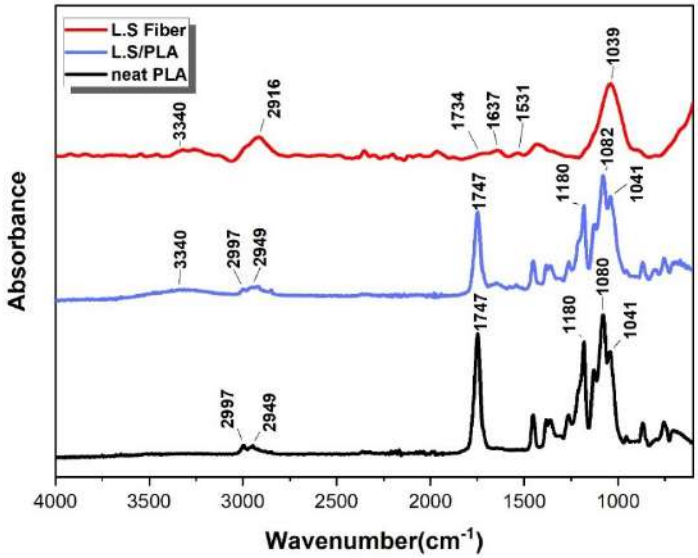

Figure III-2: FTIR Spectrum of Lygeum spartum Fibers, Lygeum spartum/PLA Biocomposite, and Pure PLA Matrix.

III.4 Thermal analysis

III.4.1 Thermogravimetric analysis (TGA) and (DTG)

Figure III.3(a,b)depicts the thermogravimetric analysis (TGA) and derivative thermogravimetric analysis (DTG) which was performed to analyze the thermal degradation behavior of L.S/PLA biocomposite, neat PLA, and L.S fibers. On one hand, TGA evaluates the mass loss of a sample as it undergoes a heat treatment over time and on the other hand, DTG details the mass loss rate, allowing for the determination of specific degradation steps. Both methods are necessary for acquiring further details about the thermal decomposition behaviors of the biocomposite, especially in this case considering the 3D printing and extrusion processes that subject the material to high temperatures. The biocomposite material operating effectively in high temperatures is significant in reducing possible defects such as voids and air bubbles on the final printed parts since these defects may significantly reduce the mechanical properties.

The TGA curve of Lygeum spartum fibers revealed three stages of weight loss. The first stage commencing at the beginning of heating is associated with moisture evaporation from the fibers

[73]. The additional important mass loss occurred at about 253°C, attributed to the degradation of cellulose and hemicellulose components [74]. A final mass loss was recorded at around 389°C due to thermal decomposition of lignin. These transitions indicate the complex thermal behavior of the natural fibers, which has to be taken into account during the processing of the biocomposite [75].

Comparatively, the TGA analysis of the Lygeum spartum/PLA biocomposite showed relatively higher weight losses during the initial stages due to greater moisture content arising from hydrophilic nature of Lygeum spartum fibers. Hence weight loss due to moisture retention was higher for the biocomposite in the early stage than for neat PLA. The onset of degradation of the biocomposite was around 281°C, earlier than neat PLA, which started losing its weight at 306°C. However, in the later stages of thermal degradation of the biocomposite, mass loss, although initiated earlier, was slower compared to neat PLA at elevated temperature. The neat PLA lost over 98.71% weight between 306°C and 386°C with fast degradation, while 97.86% weight loss of the biocomposite was observed between 281°C and 379°C, which indicated that fiber addition slightly broadens the decomposition temperature profile.

While the TGA results of the biocomposite show improvements in thermal stability with widened ranges of thermal decomposition, the use of hydrophilic fibers that are moisture-absorbing has proven to be challenging. This moisture absorption may lead to formation of air bubbles found in the printed samples (**Figure III.4**), which may weaken the structure as a result of the voids created. These results only make clear that the moisture content has to be well-controlled during the processing and the thermal treatment of the biocomposite, so that its performance is adequate for the purpose of 3D printing.

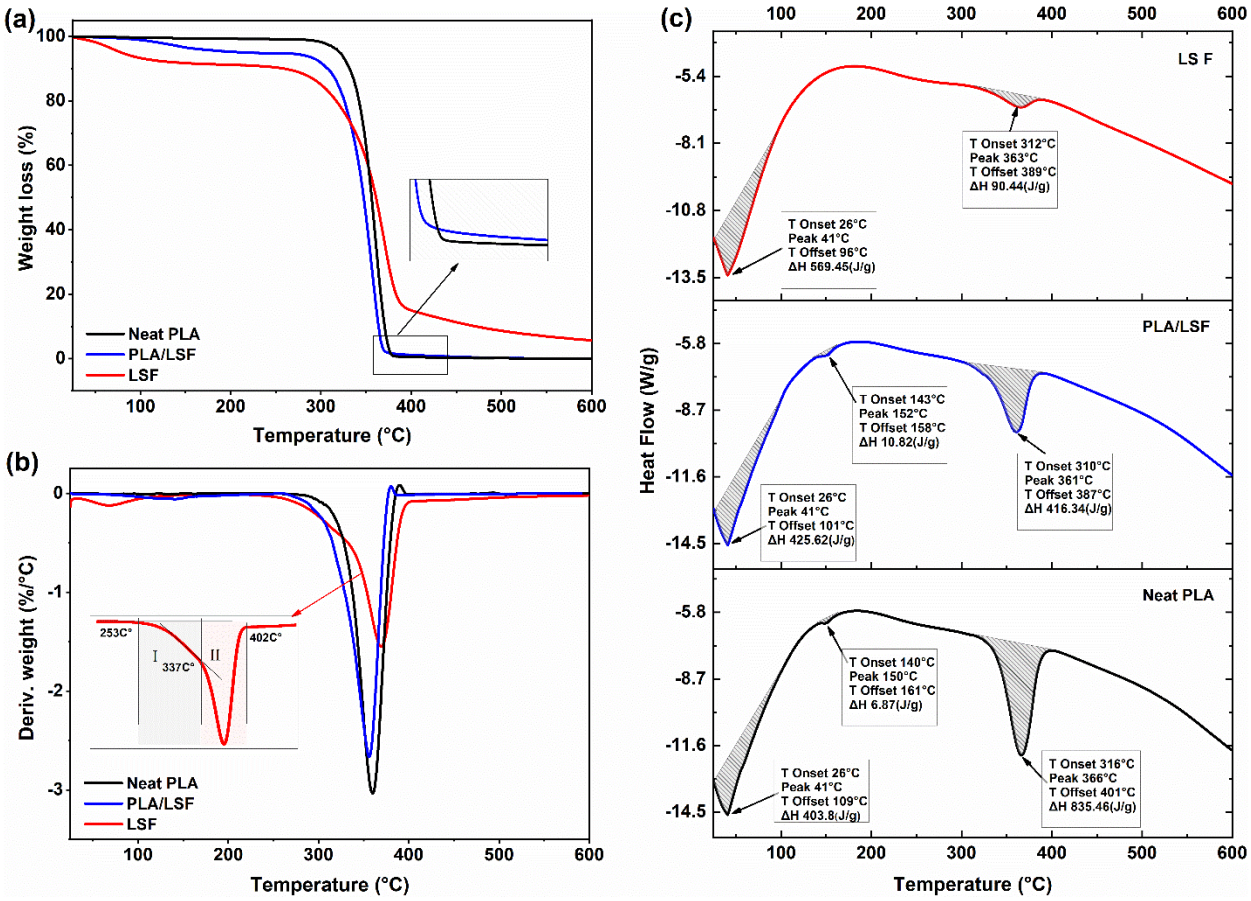

Figure III-3: Thermal Characteristics of Pure PLA, Lygeum spartum/PLA Biocomposite, and Lygeum spartum Fibers: (a) TGA, (b) DTG, and (c) DSC.

III.4.2 Differential Scanning Calorimetry (DSC) Analysis

The DSC curves for neat PLA, L.S fibers, and the L.S/PLA biocomposite are shown in **Figure III.3(c)** and it's further details in **Table III.1**. The analysis showed that there were corresponding peaks attributed to moisture evaporation in all neat PLA, L.S fiber, and the biocomposite that occurred at around 109°C. This is in opposition to the TGA where loss of moisture was captured only in the Lygeum spartum fibers. Such concentration can be simply understood from the high resolution of DSC.

As supported by the thermograms, the hydrophilic nature of the fibers is validated by the enthalpy values associated with the moisture loss where L.S had the highest enthalpy (569.45 J/g) while biocomposite (425.62 J/g) and PLA ranked lower with (403.8 J/g). This is explained by the higher

water amounts present in natural fibers which have higher specific affinity towards water than the more hydrophobic PLA.

Regarding the thermal behavior of the materials containing polymers, the DSC analysis detected melting peaks for both neat PLA and the biocomposite at approximately 150–151°C, corresponding to PLA's melting temperature [76]. The enthalpy values linked to these melting peaks were measured at 6.87 J/g for neat PLA and 10.82 J/g for the biocomposite, indicating a higher degree of crystallinity in the Lygeum spartum/PLA biocomposite. These values can be calculated using the following equation:

the DCS analysis showed that the melting peaks of both neat PLA and the biocomposite were observed at around 150–151 °Cand that's matched the PLA melting temperature. The energy values associated with these melting peaks were determined as 6.87 J/g for neat PLA and 10.82 J/g for the biocomposite, suggesting that the Lygeum spartum/PLA biocomposite has higher degree of crystallinity. The above mentioned values can be calculated by the following:

$$F_c = \frac{\Delta H_m}{[\Delta H_m^0 (1-x)]} \qquad (1)$$

where F_c is the crystal fraction, ΔH_m is the enthalpy of fusion, and ΔH_m^0 is the enthalpy of fusion of the crystal phase of PLA at 100% crystallinity. This used value (93.6 J/g) is according to sonawane et all [77]. The higher crystallinity obtained in the biocomposite was attributed to the nucleating effect of the natural fibers, which increase crystallization due to their cellulose content. According to the DSC analysis crystallinity values calculated was 11.53% for the biocomposite compared to 7.33% for neat PLA.

In the case of L.S fiber, a new peak emerged at around 363°C which is attributed to the thermal decomposition of cellulose, hemicellulose, and lignin in the biocomposite, which corresponded well with the transitions seen in the TGA results. In addition, the biocomposite exhibited an additional degradation peak in the range of 361 to 366°C, which was attributed to the degradation of the PLA matrix. The enthalpy for this degradation in neat PLA (835.46 J/g) was significantly

higher than that of the biocomposite (416.34 J/g), which suggests that the thermal decomposition mechanism may be altered due to the inclusion of fibers.

These results are quite consistent with the thermal stages noted in the TGA analysis which was the moisture loss, melting of PLA, and the degradation of the natural fibers and the polymer matrix. These results give a valuable information regarding the thermal stability and behavior for these materials particularly the effect of introducing Lygeum spartum fibers into the PLA matrix.

Table III-1: DSC Enthalpy Peaks of Pure PLA, L.S Fiber, and L.S/PLA Biocomposite.

Materials		**Peak**	**Enthalpy (J/g)**	**References**
Matrix	Neat PLA	40.9	403.80	Current work
		150.15	6.87	
		365.74	835.46	
		171	50.43	[78]
		168.24	28	[79]
		166	28.5	[80]
Composite	L.S/PLA	40.92	425.62	Current work
		151.53	10.82	
		360.5	416.34	
	PLA/alfa	171.1	40.52	[78]
	PLA/wood flour	168.33	28	[79]
	PLA/cork	167	24.2	[80]
Fibres	L.S fibre	41.21	569.45	Current work
		363.19	90.44	
	Sisal fibre	28	77	[81]
		234	22	
		328	25	
		387	10	

III.5 Morphological Analysis

The morphological analysis into the fracture surfaces showed that the neat PLA samples and the Lygeum Spartum /PLA biocomposite samples had pronounced differences in morphology, especially with regards to the interlayer air bubbles and voids. More interlayer voids were found in the neat PLA samples and these results correlate with the fracture surface images from the tensile and flexural tests (**Figure III.4**). The differences stems from the neater flow of the neat PLA during extrusion, which results in gaps being left between the printed layers. On the other hand, the biocomposite showed a reduced amount of voids as the reinforced material flows turbulently out

of the nozzle [82]. This turbulence aids in closing off void spaces with the melted material, resulting in improved layer bonding of the biocomposite [83].

The presence of voids has a substantial effect on the flexural attributes of the samples, especially when the applied forces are perpendicular to the layers. It deteriorates the interface between layers, forming stress concentration factors that reduces the flexural strength. The experiments with digital image correlation further confirmed that during flexural loading, lower layers are under tension while the upper ones are under compressive stresses, which indeed worsens the impact of interlayer voids on mechanical performance. On the other hand, the voids had a minimum effect on the tensile strength of the samples particularly those printed at a 90° angle, where the load was parallel to the direction of extruded lines.

The presence of Air bubbles was greatly noticed on the biocomposite samples and this affected the tensile and flexural strength. It is possible that the mechanism of formation of air bubbles is related to the moisture evaporation by the plant fibers or even due to thermal degradation during the printing [84-86]. When fibers are exposed to high temperatures in the nozzle, they vaporize moisture they were absorbing which creates gas bubbles within the material. Furthermore, some printing parameters may have been led the fibers to an excessive residence contact time in the nozzle exposing them to the high temperatures, leading to partial degradation of the fibers which results in the formation of the gas bubbles. These bubbles are stress concentrators and thus weaken the parts that are printed in the mechanical aspects towards the prints strengthening and stiffening. The mechanisms of fracture were studied in detail using SEM imaging and this showed the damage modes and the failure mechanisms on the micro-scale. The images emphasized the degree of impact the voids and bubbles had on the fracture menus and gave insight on how the flaws in the material perform on the composite's overall functionality.

Observations from SEM images reveal important details to failure mechanisms in both neat PLA and L.S/PLA samples such as matrix cracking, fiber-matrix debonding, fiber pull out, and matrix-matrix friction. Some of the areas within the SEM micrographs showed fiber pull out where the weak fiber matrix bonding is displayed by fiber imprints and pits. Other areas however showed fibers that remained well adhered to the matrix indicating effective load transfer and improved fiber matrix interactions. Matrix cracking was however more prominent in flexural tests as the stress increased leading to crack initiation and propagation. These observations are also consistent

with AE analysis that confirmed the onset and progress of these damage modes, which helped to fully understand the fracture behavior of the biocomposite material.

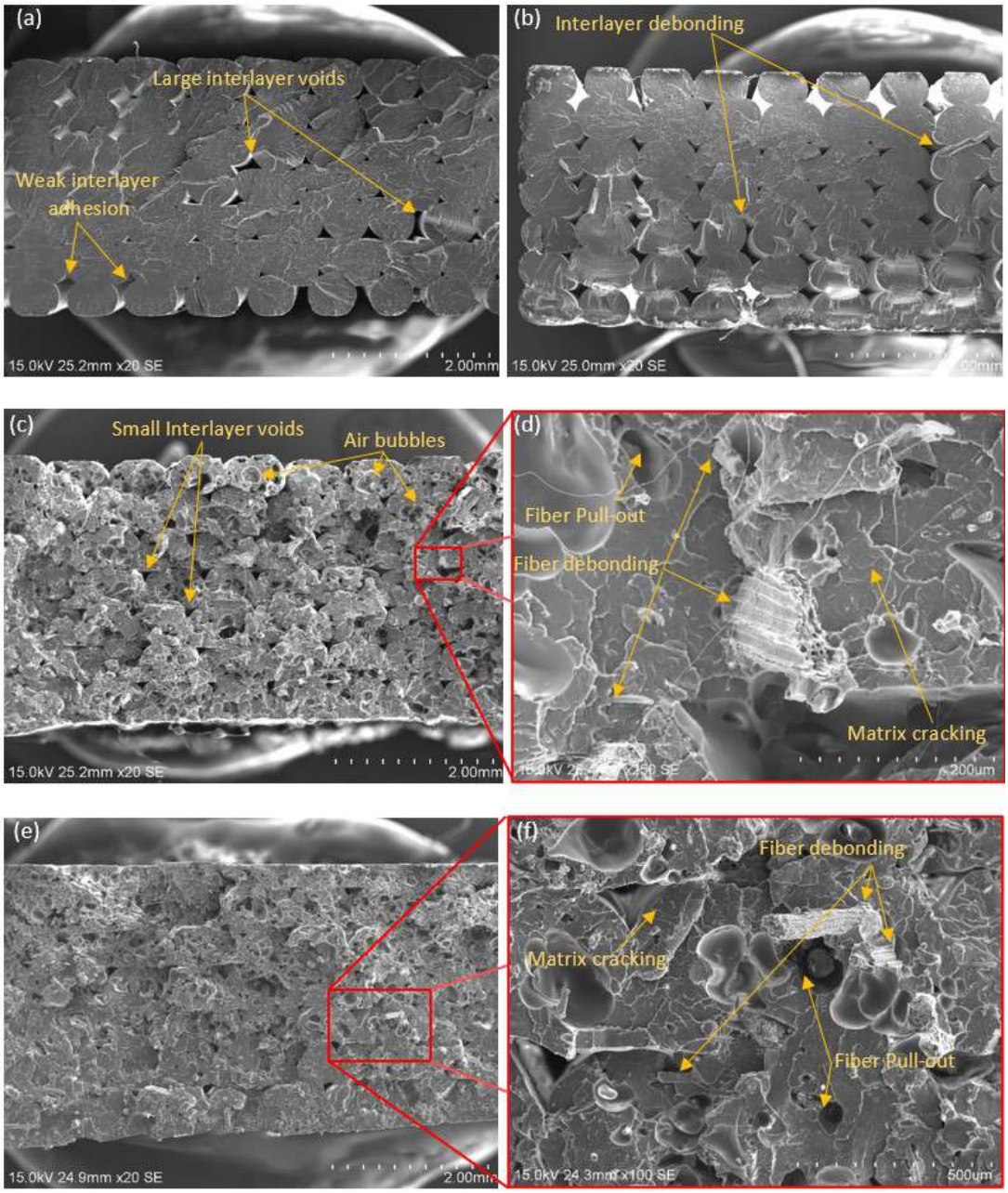

Figure III-4: SEM fracture surfaces: (a-b) and (c-d) pure PLA and L.S/PLA respectively after tensile tests, (e-f) L.S/PLA after Flexural Testing.

III.6 Conclusion

This chapter provides an in-depth analysis of the physicochemical and thermal properties of Lygeum spartum/PLA biocomposite. From the Fourier Transform Infrared Spectroscopy (FTIR) analysis, a reliable estimation of the chemical interactions between the fibers and PLA matrix was obtained which proved the successful embedding of the fibers into the composite. Scanning electron microscopy (SEM) provided critical information on the microstructure focusing on the dispersion and bonding of fibers within the matrix.

The composite's thermal stability and crystallinity was evaluated through thermogravimetric analysis (TGA) and differential scanning calorimetry (DSC). These results are essential for studying the performance of this biocomposite for different industrial purposes, especially for those which require elevated temperature operation. In general, the characterization done in this chapter provides important information regarding the functioning of the composite and helps to enhance its development and application.

Chapter IV

Mechanical Properties and Damage Assessment Through Spectral Analysis

IV.1 Introduction

The potential application of natural fiber reinforced composites and other composite materials is dependent primarily on their mechanical properties which are essential for the automotive, aerospace, and construction industries. These properties allow the composite to endure stresses, resist impacts, and function appropriately during prolonged mechanical activity. The purpose of this chapter is to conduct a detailed study of the mechanical properties of Lygeum spartum/PLA biocomposite with the use of both destructive and non-destructive test analyses.

Tensile and flexural tests fall under the category of destructive testing and are useful in determining informations on ultimate strength, stiffness, and ductility of the material. these tests are crucial in order to undertake an assessment of the mechanical performance of both the neat PLA and Lygeum spartum/PLA biocomposite and their load bearing capacities and respective failure modes. These properties like tensile strength, flexural strength and elastic modulus greatly help us understand how the addition of natural fibers impacts the mechanical performance of biocomposite.

Along with destructive analysis, it important to investigate non destructive evaluation (NDE) methodologies that can track the performance of the material without causing damage. NDE methodologies, like the Impulse Excitation Technique (IET), Digital Image Correlation (DIC), and also Acoustic Emission (AE), are of the almost importance because they allow for materials to be placed under load while still remaining intact. These techniques enable real time monitoring of damage development, deformation, strain distribution, and elastic properties on the material, allowing for analysis of the material throughout its use. This combination of strategies helps evaluate Lygeum spartum/PLA biocomposite from the initital and final perspectives. Since Neat PLA is the matrix for this biocomposite, it enables us to compare mechanical properties that helps assessing the damage mechanisms without physical interaction and the efficiency of natural fibers as reinforcements and their effects on the biocomposites performance. This chapter will detail the information acquired by the two testing procedures which provide a broad explanation of the mechanical behavior and damage evolution of the biocomposites of interest.

IV.2 Mechanical properties

IV.2.1 Tensile test

The tensile test results in **Figure IV.1**, illustrates the behavior of Lygeum spartum/PLA biocomposite and neat PLA specimens during stress-strain testing. It was clearly noted that the biocomposite's mechanical response is not similar to that of neat PLA as highlighted in **Table IV.1**. Biocomposite had lower tensile strength compared to neat PLA samples that exhibited higher strength. This reduction in tensile strength points to the possibility that the introduction of Lygeum spartum fibers is compromising the strength of the PLA matrix because of poor adhesion achieved between the hydrophilic fibers and the hydrophobic polymer [87, 88].

The strain at failure of the composite was between 1.84% and 2.27%, indicating that it is more ductile than the PLA which had a more brittle failure, with strain values between 1.5% and 1.8%. This increase in ductility for the biocomposite is attributed to the natural fibers ability to absorb energy and deflect cracks, thus toughening the material [87, 89]. The average tensile modulus values for both materials were almost close, the biocomposite having an average of 3.24 GPa and the neat PLA 3.39 GPa. However, it seems the Lygeum spartum fibers do increase the flexibility of the PLA matrix without reducing its stiffness.

The poor tensile strength can be attributed to the poor interfacial adhesion between the Lygeum Spartum fibers and the PLA, which leads to stress concentration in same region and causing premature failure [25, 90]. On the other hand, the increased ductility is encouraging as it indicates that the fibers aid in stress distribution and bolster the material's toughness. This is consistent with what has been found previously on the use of natural fibers to reinforce PLA based composites, where the contradictory behavior of strength and the ductility in fiber reinforced composites is noted.

As compared to other PLA matrix composites reinforced with hemp or wood fibers (**Table IV.2)**, Lygeum spartum/PLA biocomposite had comparable or slightly better values for Young's modulus (3.1 GPa) and tensile strength (33.37Mpa). On the other hand, elongation at break (1.99%) was within the range which are reported for the rest of the natural fiber composites which range between 0.8% and 5% depending on the fiber type.

Furthermore, printing parameters like layer height, infill percentage, speed of the extruder, printing direction, and temperature has significant impact on the result of the PLA composites 3D printed mechanical properties [91-97]. For example, reducing the layer height and increasing the infill percentage tend to enhance the tensile strength and modulus, while the direction of printing the object is also very important to the overall performance of the material. These results suggest that there is a compromise among strength, stiffness, and ductility that needs to be achieved in these biocomposites by well optimizing these printing parameters.

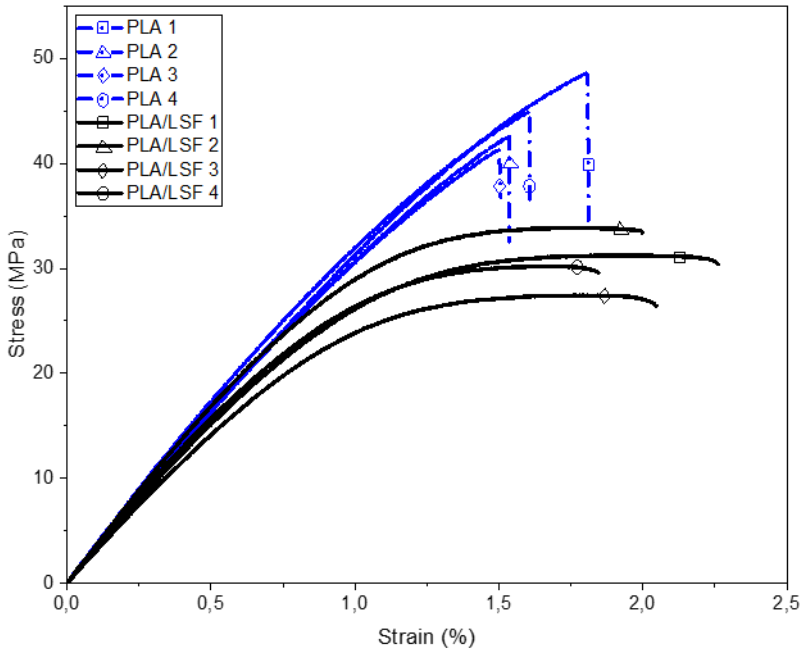

Figure IV-1: Tensile test curves for neat PLA and L.S/PLA biocomposite.

Table IV-1: Results of tensile characteristics for the L.S/PLA bio-composite and the neat PLA specimens.

	TENSILE TESTS									
	L.S/PLA					PLA				
specimens	1	2	3	4	average value	1	2	3	4	average value
Elasticity modulus (GPa)	3.201	3.528	2.959	3.303	3.247	3.307	3.347	3.379	3.565	3.398
Max stress (MPa)	31.24	33.85	27.45	30.21	30.68	48.45	42.54	41.27	44.82	44.27

Elongation at break (%)	2.26	1.99	2.04	1.84	2.03	1.8	1.53	1.5	1.61	1.61

Table IV-2: Comparison of tensile properties between literature and current work.

Composite Matrix/Fibers (content)	fiber wight ratio (%)	Pure matrix tensile test			Composite tensile test			nozzle diameter (mm)	layer thickness (mm)	References
		stress (MPa)	strain (%)	young modulus (MPa)	stress (MPa)	strain (%)	young modulus (MPa)			
wood flour fiber/PLA	10	38	-	-	21	-	-	-	-	[79]
Wood flour-filled/PLA	5	27	5	-	23	5	-	0.4	-	[98]
wood fiber/PLA-PHA	10-20	-	-	-	21	1.5	2100	0.4	0.3	[99]
hemp fiber/PLA	20	-	-	-	23,29	1,4	2884	-	0.18	[100]
wood fiber/PLA	30	-	-	-	28.7	-	3115	0.4	0.2	[101]
cork/PLA	10	60.03	1.53	3344	26.1	0.8	2111.8	0.8	0.4	[80]
Wood flour fiber/PLA	20	31	3	1750	13	2.5	1125	-	-	[102]
hemp/PLA	10	35	-	2500	38	-	3400	1	1	[103]
harakeke/PLA	10	35	-	2500	34	-	2700	1	1	
Lygeum. S/PLA	10	48.27	1.81	3341	33.37	1.99	3104	0.8	0.5	current work

IV.2.2 Flexural test

Figure IV.2 displays the results of flexural testing of the Lygeum spartum/PLA biocomposite specimens. Such results also provide information on the differences in the mechanical properties of neat PLA and Lygeum spartum/PLA biocomposite. As it is seen in **Table IV.3**, the stress values of the biocomposite samples have a range from 64.67 MPa to 88.76 MPa, and the average value is 75.69 MPa. The PLA samples have lower stress values ranging from 59.25 MPa to 77.6 MPa and averaging 69.22 MPa. It can be seen that the incorporation of Lygeum Spartum fibers into a PLA matrix increases its flexural strength. This is most likely due to the reinforcing effect of the fibers on the matrix, making it more resistant to bending. Measuring strain shows a range of 2.79% to 3.74% with an average of 3.31% for the biocomposite, whereas for neat PLA the strain range was a little higher 3.28% to 3.64% with an average value of 3.40%. These differences, although nominal, indicate that this bioplastic able to withstand increasingly stronger bending forces without losing flexibility.

The flexural values of Lygeum spartum/PLA biocomposite exhibited better performance compared to neat PLA and many other PLA composites that use other natural fibers (**Table IV.3**), except for the wood fiber/PLA that show the highest stress (113.6 MPa) and modulus (4.1GPa) due to the layer thickness that was optimized. The increase of flexural properties of the L.S/PLA biocomposite was made possible by the adequate bonding of fiber to matrix and the significant reduction of voids and defects in the printed layers, which was confirmed by the SEM observation of the fracture surfaces (**Figure III.4**). On the other hand, the neat PLA samples had more voids and gaps between the layers, which led to poorer interlayer adhesion and more delamination during the test.

In the flexural test, which involves applying a force perpendicular to the printed layers (with a 90° printing orientation used in this study), layer separation contributes to the formation of stress concentration areas with poor adhesion which will increase the failure rate [27]. The deformation field evidenced by the DIC test reveals the distribution of strain, with the upper layers in tension while the lower ones are under compression (**Figure IV.5**). The results verified that the fiber reinforcement helps to reduce the delamination while increasing the strength of the materials allowing to achieve higher flexural strength than for neat PLA.

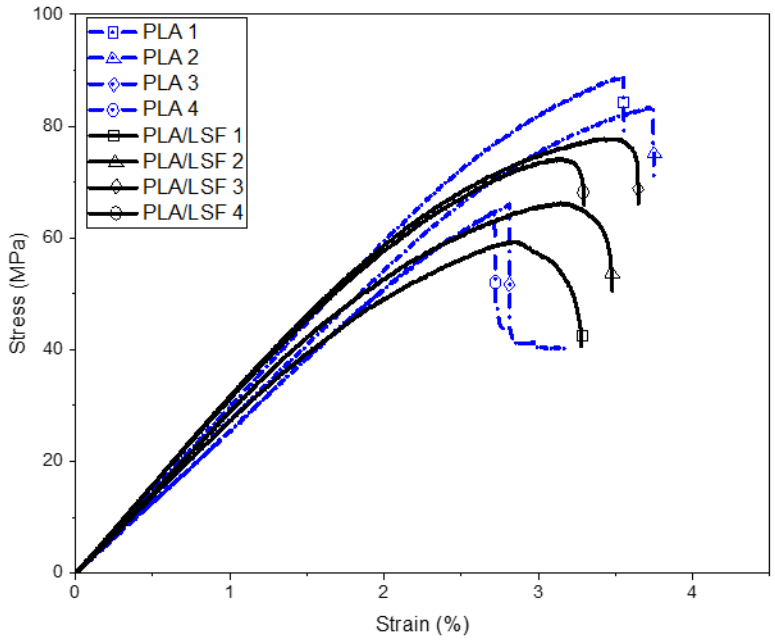

Figure IV-2: Flexural test curves for Neat PLA and L.S/PLA biocomposite.

Table IV-3: Results of flexural characteristics for the L.S/PLA bio-composite and the neat PLA specimens.

	FLEXURAL TESTS									
	L.S/PLA					PLA				
specimens	1	2	3	4	average value	1	2	3	4	average value
Elasticity modulus (GPa)	2.79	2.811	3.176	3.163	2.985	3.043	2.693	2.526	2.461	2.68
Max stress (MPa)	59.25	66.15	77.6	73.88	69.22	88.76	83.35	65.98	64.67	75.69
Elongation at break (%)	3.28	3.47	3.64	3.28	3.4	3.55	3.74	3.18	2.79	3.315

Table IV-4: Comparison of flexural properties between literature and current work.

Composite Matrix/Fibers (content)	fiber wight ratio (%)	pure matrix bending test			composite bending test			nozzle diameter (mm)	layer thickness (mm)	layers orientation	References
		stress (MPa)	strain (%)	young modulus (MPa)	stress (MPa)	strain (%)	young modulus (MPa)				
Wood flour fiber/PLA	10	70.5	-	-	47	-	-	-	-	-	[79]
wood fiber/PLA	30	-	-	-	113.6	-	4125	0.4	0.2	0	[101]
wood flour fiber/PLA	20	59	4.2	2250	21	3.5	1100	-	-	-	[102]
Wood particles/PLA	30	102	-	3300	46	-	2100	0.4	0.2	45°/-45°	[104]
agave Fibers/PLA	10	87	-	3100	59	-	2750	-	0.3	45°/-45°	[105]
anchovy fishbone powder EE/PLA	10	98.2	3.8	2256	111.2	3.1	2975	0.4	0.1	0°/45°/-45°	[106]
Lygeum. S/PLA	10	70.84	3.75	2704.94	66.15	3.64	3026.54	0.8	0.5	90°	(Current work)

IV.3 Elastic Modulus Determination Using Impulse Excitation Technique (IET)

Four samples of each material were tested using IET in the present study and yielded consistent values of frequency, damping and modulus for the same specimens **Table IV.5**. This thereby demonstrates the technique's reliability. Standard deviation (SD) and the coefficient of variation (CV) shown in **Table IV.6** demonstrates the high level of accuracy of the technique. However, some variations were observed among the samples within each group. The composite specimens had an average elastic modulus of 0.6 GPa higher than the neat PLA specimens indicating the enhancement in flexural properties due to the addition of L.S. fibers.

A comparison was made between average elasticity modulus results of IET and flexural test and they were found to almost similar. Flexural test showed 17% and 13% lower results than IET for composite and neat PLA specimens, respectively. This difference could be accounted for by the theoretical assumptions made in the IET calculations and actual testing conditions which the measurements were taken [107-109]. The difference between them was however not significant, thus the IET technique can be considered robust and quite efficient for measuring these elastic properties.

Table IV-5: presents the frequency, damping, elasticity modulus, and their mean values for the composite and the neat PLA specimens.

	Frequency (Hz)			Freq average	Damping			Damp average	E modulus (GPa)			E average
L.S/PLA	1030.73	1030	1031.53	1030.75	0.0136	0.0137	0.0137	0.0137	3.38	3.38	3.39	3.38
	1019.01	1019.34	1019.54	1019.3	0.0136	0.0144	0.0133	0.0137	3.58	3.59	3.59	3.59
	1021.45	1021.58	1021.74	1021.59	0.0124	0.0129	0.0128	0.0127	3.76	3.77	3.77	3.77
	1018.56	1019.17	1019.34	1019.02	0.0128	0.0131	0.0131	0.013	3.71	3.71	3.71	3.71
PLA	916.77	916.16	917.03	916.65	0.0127	0.0124	0.0116	0.0123	3.38	3.38	3.38	3.38
	895.66	885.553	886.768	889.33	0.0149	0.0115	0.0118	0.0127	2.99	2.93	2.94	2.95
	957.1	957.206	957.233	957.18	0.012	0.0121	0.012	0.012	3.12	3.12	3.13	3.12
	912.765	913.386	914.204	913.45	0.0121	0.0112	0.0117	0.0116	2.89	2.89	2.89	2.89

Table IV-6: shows the mean, standard deviation (SD), and coefficient of variation (CV) of the frequency, damping, and elasticity modulus for the composite and neat PLA specimens.

		Frequency (Hz)	Damping	E modulus (GPa)
L.S/PLA	mean	1022.666	0.0132	3.6116
	SD	5.5131	0.0005	0.1697
	CV	0.0053	0.0388	0.047
PLA	mean	919.1529	0.0121	3.0866
	SD	28.1328	0.0004	0.2189
	CV	0.0306	0.0372	0.0709

IV.4 Digital Image Correlation (DIC)

Digital Image Correlation (DIC) is an optical non-contact technique for measuring the strains and displacements on the surface of the specimens under mechanical testing. It consists of taking images of the specimen at very high resolutions before, during, and after a load is applied to the specimen. Tracking the movement of surface patterns or speckles printed onto the surface of the specimen allows the DIC to obtain strain and displacement rates over the entire surface simultaneously and in real time [110].

By assessing the relative displacement of points between frames, the DIC system is able to undertake the full-field measurement of strain and displacement. The information gathered from DIC is especially beneficial when creating stress-strain curves, as well as locating the specific areas of deformation or failure in neat PLA and Lygeum spartum/PLA biocomposite specimens [111, 112].

DIC has many benefits compared to the conventional methods of measuring strain like strain gauges because it makes it much easier to collect more data regarding the deformation, especially in complex shapes or 3D printed components. DIC was employed to observe changes in deformation and strain in 3D printed samples subjected to tension and flexure. This helped provide deeper insight into how materials behave, including the determination of possible failure strains and regions of maximum stress concentration [113].

IV.4.1 The use of DIC Analysis in the case study

In this work, strain and displacement fields were captured during tensile and flexural tests using Digital Image Correlation (DIC). DIC provided a non-contact approach to measure material deformation that was independent of traditional strain gauges like extensometers. In this case, DIC was useful for quantifying stress concentration phenomena and deformation patterns around the entire specimen surface, which is a vital factor concerning the performance of 3D printed structures including Lygeum spartum/PLA biocomposite and neat PLA specimens.

IV.4.2 Comparison Between the Experimental and DIC Results

Two techniques were used to measure engineering strain: a conventional extensometer gauge, and DIC, which was based on the displacement field obtained from the surface of the specimens. Even though both techniques returned slightly equal values, DIC demonstrated improvements in the elastic modulus due to its capability to minimize mechanical errors linked to the testing setup. DIC allowed for eliminating the air between deferent mechanism in the testing machine, calibration errors, and local deformations at the reaction points [114]. Thus, more accurate material properties were obtained. As shown in **Table IV.7**, the values for elastic modulus, measured by DIC, were improved compared to those from the extensometer for tensile and flexural tests for neat PLA and the composite specimens.

As shown in **Figure IV.4**, the stress-strain curve comparisons over the tensile test on the neat PLA and biocomposite specimens indicated that the DIC curves followed the same trend as experimental curves and showed good agreement in the elastic region. The DIC slope was lower than the experimental slope until about 0.35% strain, after which the values diverged from each other only to converge again at approximately 1.25% strain. This behavior suggests that DIC is able to detect small changes in material deformation and is able to capture more accurate strain measurements in areas of high localized stress. In the flexural tests, the slope of DIC results curves was found to be lower in the elastic region than that of the experimental curve, which reinforces the advantages of DIC over the conventional techniques of measuring elastic modulus for both materials with claimed results for much higher elastic modulus.

Table IV-7: the results obtained from the experimental and DIC methods.

specimens	tensile tests				flexural tests			
	L.S/PLA		PLA		L.S/PLA		PLA	
	EXP TESTS	DIC TESTS	EXP TESTS	DIC TESTS	EXP TESTS	DIC TESTS	EXP TESTS	DIC TESTS
1	3201	3234	3307	4017	2790	2712	3043	2401
2	3528	3550	3347	3977	2811	3293	2693	2185
3	2959	2613	3379	3332	3176	2730	2526	3602
4	3303	3299	3565	3584	3163	3504	2461	3896
the average value	3248	3174	3400	3727.5	2985	3059.75	2681	3021

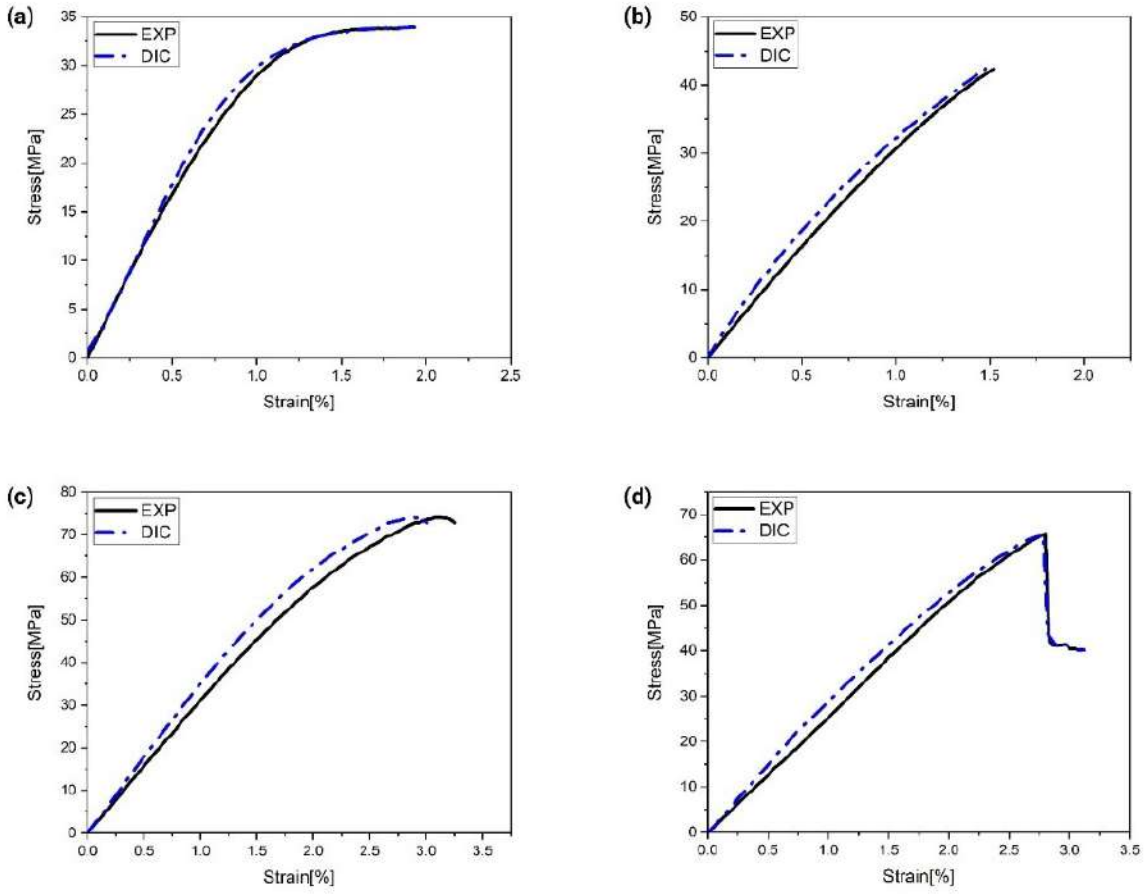

Figure IV-3: stress-strain curves obtained from the experimental and DIC methods for (a) composite tensile test, (b) neat PLA tensile test, (c) composite flexural test, and (d) neat PLA flexural test.

IV.4.3 Stress Concentration and Strain Analysis via Digital Image Correlation DIC

DIC in **Figure IV.5** provided details of the analysis regarding the stress concentration under both tensile and flexural loading. In the case of the tensile test, the displacement field was concentrated at the upper portion of the sample. This is where the moving jaw of the testing machine was pulling the sample apart while the lower portion of the sample was fixed. The graded vertical displacement field allowed to identify other areas that were concentrated with high strain, which is essential for analyzing the strain varying microstructure of the biocomposite materials, In which the orientation of fibers and their distribution are important parameters to be considered for the mechanical performance. When fibers were in the direction of the loading, they aided in resisting tensile forces.

In contrast, some areas were subjected to compression and fibers buckled or kinked, which caused local strain concentrations, commonly referred to as kink bands. This phenomenon was more pronounced, which stems from the 90° printing orientation used within the study, which placed the fibers in parallel to the direction of loading.

The DIC captured during the flexural test, has shown the typical tension and compression behavior which occurs at the same time but in different areas of the specimen. As seen from the strain field in **Figure IV.5-b**, the upper layers were under compression while the lower layers were under tension. This pattern clearly indicated compressive strain at the upper surface and tensile strain at the lower surface, while the concentration of stresses in the lower layers caused cracks and leading to the fracture. In bending tests, DIC provided better visualization of the material's behavior under stress. It also captured more phenomena than the methods of bending which only used point strain gauges and captured dynamic strain at those specific points without the entire full-field deformation profile.

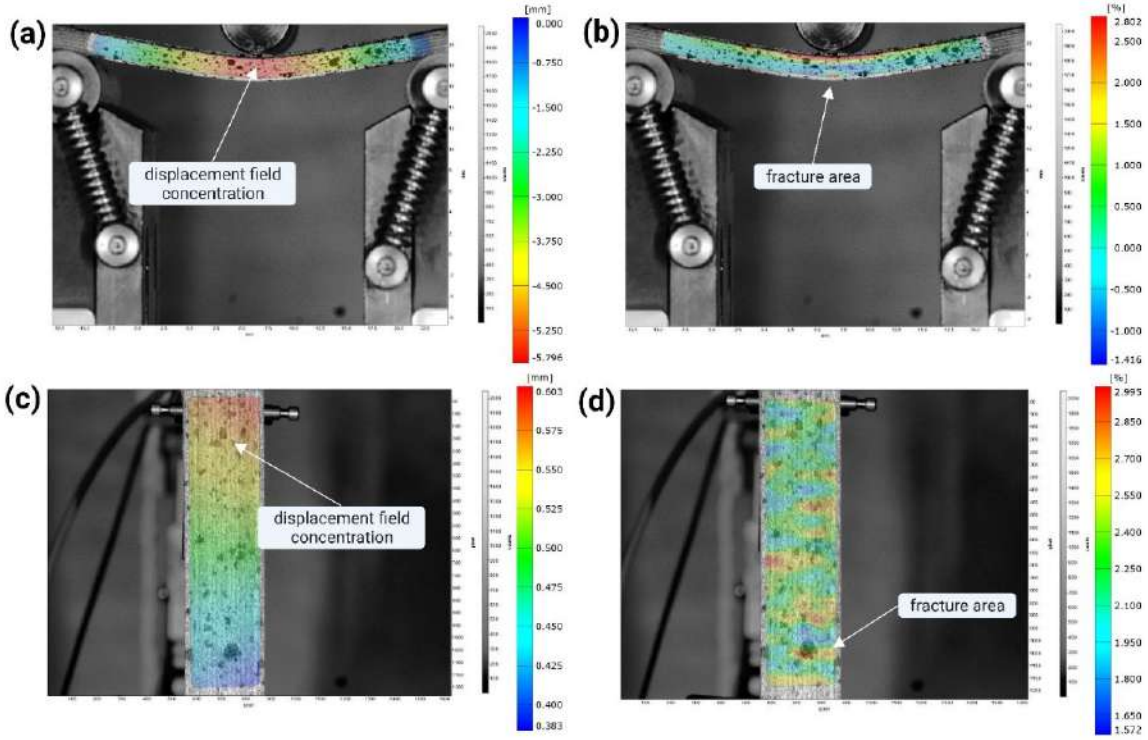

Figure IV-4: Deformation field and displacement field of composite specimens in tensile and flexural tests.

IV.4.4 Effectiveness of DIC in this Study

The DIC method showed to be particularly useful in evaluating the tensile and flexural behaviors of neat PLA and Lygeum spartum/PLA composites. The improvement in strain measurement that was achieved, particularly in the regions of high strain concentration, aided greatly in understanding the behavior of the material under force application. More importantly, the DIC data was superior compared to the extensometers, resulting in more accurate determinations of elastic moduli. For the flexural tests, DIC helped estimate the strain in the different layers and was able to demonstrate the upper layers with more compression and lower layers with more tension leading to the understanding of the failure mechanisms of the specimens.

IV.5 Acoustic emission

Acoustic Emission (AE) is a method for evaluating materials that has existed since the 1950s. AE measures the elastic waves produced by the sudden energy release within a material and tracks its damage. AE is useful to monitor physical changes such as crack formations and material failures produced during mechanical loadings [115]. In the past, AE was used by structural engineers to track the conditions of bridges, but later became a were made to study composites, metals, and ceramics. AE is useful in real-time damage assessments of materials such as crack formations and failures. Nowadays, AE is a great tool for assessing the durability and structural strength of materials such as fiber-reinforced composites and 3D prints.

IV.5.1 Overview of Acoustic Emission Data

Acoustic Emission (AE) data is a technique allows for the examination of material characteristics such as deformation mechanisms in fiber-reinforced composites. During the testing phase, internal damage such as matrix cracks, fiber debonding, and fiber pull-out cause the structure to emit stress waves. AE sensors pick up these high frequency stress waves where damage is occurring internally and convert them to electrical signals which can be analyzed to make conclusions about the material being tested. In addition, AE signals are generated and recorded for all the events that take place during the mechanical tests and every AE event corresponds to some internal event of analysis like crack propagation or matrix friction. The main features extracted from AE signals include:

- **Energy:** Indicates the magnitude of damage.
- **Count:** The number of AE hits or events.
- **Frequency:** The range of frequencies in the AE signal in Hz.
- **Amplitude:** Related to damage severity.
- **Rise:** Time from noise threshold to peak amplitude.
- **Duration:** Total time of each event in µs.

Figure. IV.6 depicts a typical AE waveform revealing the correlation of different features to various types of damage. For example, matrix cracking generates signals that are generally lower in energy and amplitude whereas fiber pull out events are characterized by high energy, high amplitude signals. The capability of distinguishing between these mechanisms from AE data in real-time is particularly useful in composites where many damage types take place simultaneously. Automated AE data analysis, through machine learning models, facilitates the real time classification of damage modes. In subsequent sections, we discuss the processing of data, application of machine learning, and the predicted mechanical properties and performance evaluation of the material.

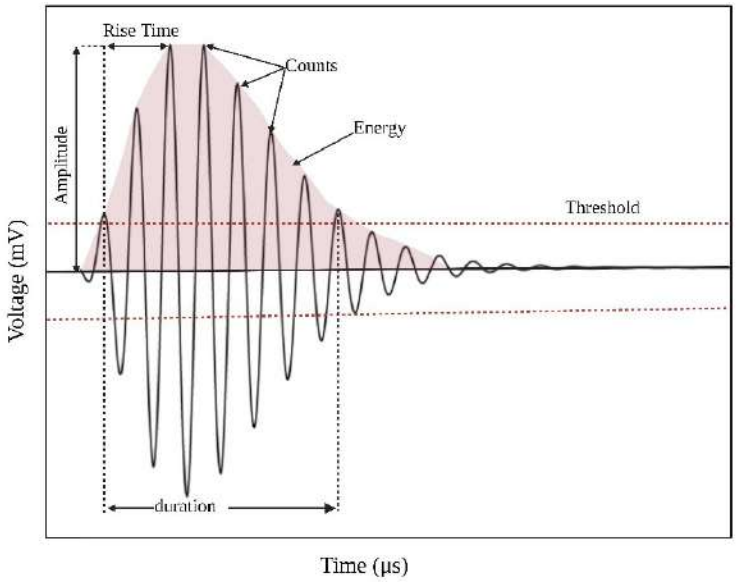

Figure IV-5: typical acoustic emission waveform [116].

IV.5.2 Preprocessing AE Data for Machine Learning

Preprocessing of Acoustic Emission (AE) Data for Machine Learning Analysis

In order to facilitate the effective use of machine learning algorithms, AE data undergoes a multistep process that includes noise reduction, feature extraction, normalization, and feature selection. These steps enable engineers to gauge the performance of Lygeum spartum/PLA biocomposites more accurately.

1. **Cleaning and Noise Reduction using (IQR Method)**: The AE data was first filtered with a 35dB threshold to reduce background noise and maintain focus on damage signals. Outliers from the data set were removed with the inter quartile range IQR method that focuses on the exclusion of extreme values. These steps improved the dataset and models to ensure that they adequately captured the material responses.

2. **The Extraction of the features:** Damage mechanisms were analyzed using key features like energy, count, frequency, amplitude, duration, and rise of AE signals. High energy signals directly relate to severe damage like fiber pull-out being experienced. On the other hand, low energy signals indicate that less severe damages like matrix cracking have occurred. The machine learning Models are able to predict damage with greater accuracy by focusing on these parameters.
3. **Normalization of the AE Data:** Z-score normalization was performed to AE data, helping to maintain equal contribution from all features. With normalization, biases are eliminated, ensuring equal representation in both training and testing sets. The model is better able to process data with the highly varying signals once normalization occurs.
4. **Selection of the relevant features:** Advanced feature selection methods including PCA were adopted to keep only the most important AE features within the model. Focused prediction approaches strengthen model accuracy alongside improving efficiency by lowering the computing load impact.

IV.5.3 Heatmap of Feature Correlations

In this experimental study of the acoustic emissions (AE) during tensile and bending tests, correlation of between AE parameters was obtained. The heat maps showing the correlation

coefficients regarding different AE parameters showed some interesting dependencies [117], In particular, the correlation coefficients are necessary for construction of highly accurate predictive models through Artificial Neural Networks (ANN), giving clues as to how AEs are generated and their correlation with various mechanical properties of the biocomposite materials. These correlations and their implications are studied further in the following sections, which deal with the application of AE parameters as predictors in the already developed machine learning algorithms. The correlation between the AE features from the tensile and flexural tests is depicted in the heat map in **Figure IV.7** and **Figure IV.8**.

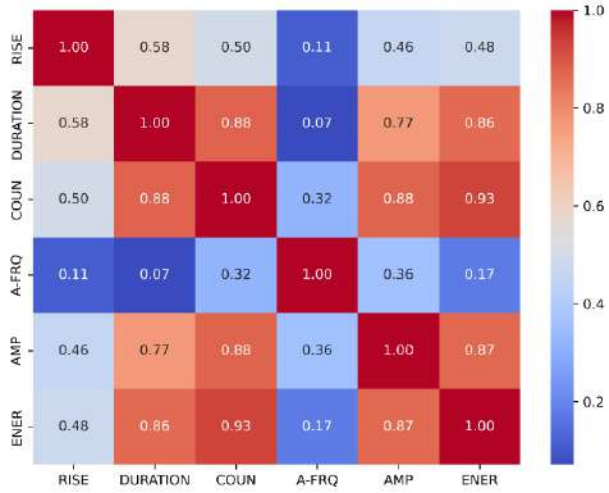

Figure IV-6: Heat map of correction coefficients between acoustic emission features for tensile test.

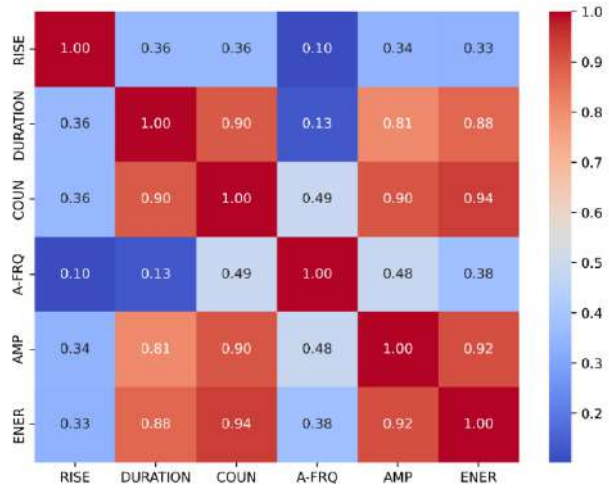

Figure IV-7: Heat map of correction coefficients between AE features for flexural test.

IV.5.4 Damage Evolution Analysis Using Acoustic Emission

The progression of damage in Lygeum spartum/PLA composites during tensile and flexural testing was assessed using acoustic emission (AE) analysis. In **Figure IV.9**, the stress-strain curves of the L.S/PLA are exhibited along with the accumulated AE energy and count for both tests. The cumulative AE energy constantly displays a trend that can be compared to the cumulative count, these signals can be used to identify damage modes within the composite [118, 119].

During the tensile test, at least three different damage modes were identified from the analysis of AE signals. In the first stage (Region 1, **Figure IV.9-a**), related to the elastic region of the curve, no AE signal of any note was registered above the noise threshold level. This indicates that no damage sustained during the elastic phase of deformation. The next phase begins (Region 1 – 2), which goes to approximately a 0.5% strain, there is a low-energy signal that reaches the threshold level. This suggests that some damage, most likely due to matrix microcracking, has commenced. As the strain of the material between 0.5% and 1.12% (Region 2–3), AE activity demonstrates relatively vast increases, accruing exponentially across cumulative energy and count. This suggests significant damage mechanisms like matrix-matrix friction and fiber pull out. The material enters a state of yielding at this stage, which is when the damage mechanisms become more pronounced. In the final phase (region 4), the sharp increase in AE activity observed corresponds with the maximum tensile stress after 1.12% strain, at which point fiber pull out emerges as the dominant damage mode. This mode is characterized by intense acoustic activity.

In flexural tests, AE signals had a similar pattern as they did in the tensile tests. The strain-stress curves obtained for the composite material during flexural loading are displayed in addition to the accumulated AE energy and count in **Figure IV.9-b**. No AE signals that exceeded the detection threshold and were recorded before Region 1 in the elastic region, This particular region shows that deformation that exceeds approximately 1.5% does not result in significant damage. Compared to the tensile test, AE signals appear sooner in the flexural test with considerably lower cumulative energy and count. This shows the initial matrix micro cracking. The transition to more significant damaging modes like matrix friction and fiber debonding is marked with a swift increase in the activity at region 3, identical to the results from tensile test. The final phase, right

before the ultimate strength is reached, shows a rapid pullout of the fibers which is indicated by a sharp rise in the AE energy and Count. This is followed by a swift change in damage and pull out damage leading to failure of the specimen.

This study shows the different damage development stages in L.S/PLA composites during tensile tests and flexural tests. AE helps in further understanding the damage development stage progression, from matrix cracking to fiber pulling out.

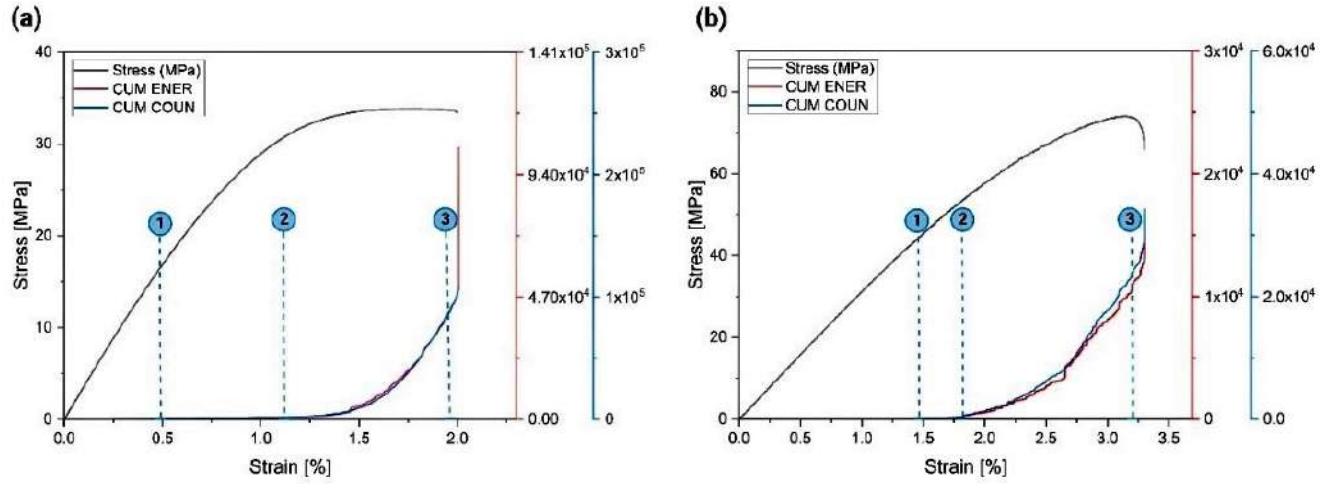

Figure IV-8: The typical stress-strain curves and the corresponding cumulative AE energy and count for tensile (a) and flexural testing (b) for the L.S/PLA bio-composite specimens.

IV.5.5 AE data processing

In order to analyze the damage mechanisms in a L.S/PLA composite, we used a multi dimensional approach which is based on principal component analysis (PCA). This type of analysis can condense data into fewer dimensions while keeping most of the necessary information [120]. Our approach was to apply PCA to turn original data into a new set of variables that are weighted combinations of the original variables.

Figure IV.10-a explains that the variance in information ratio based on the number of principal components used in PCA has been illustrated. This graph is helpful in determining the appropriate

number of principal components so as to capture most of the information while minimizing the complexity of the model. The curve shows a significant shift after the second principal component, indicating that two parameters capture most of the useful information. Hence selecting two components for our PCA is reasonable as it is simple yet able to capture relevant variations in the data.

PCA biplots illustrated in **Figure IV.10-b**, presents a scatter diagram of the principal component scores alongside the loading vectors of the original variables. It represents the projection of the dataset on the first two components PC1 and PC2 and the weight of each original variable associated with the principal components. The variables that contribute positively to the first principal component include AMP (amplitude), ENER (energy), and COUN (count), while A-FRQ (frequency) is the only variable that contributes positively to the second principal component. This implies that the two components measure different characteristics of the damage mechanisms: the first one is likely to be the damages mode intensity, while the second one may be damage mode frequency or timing.

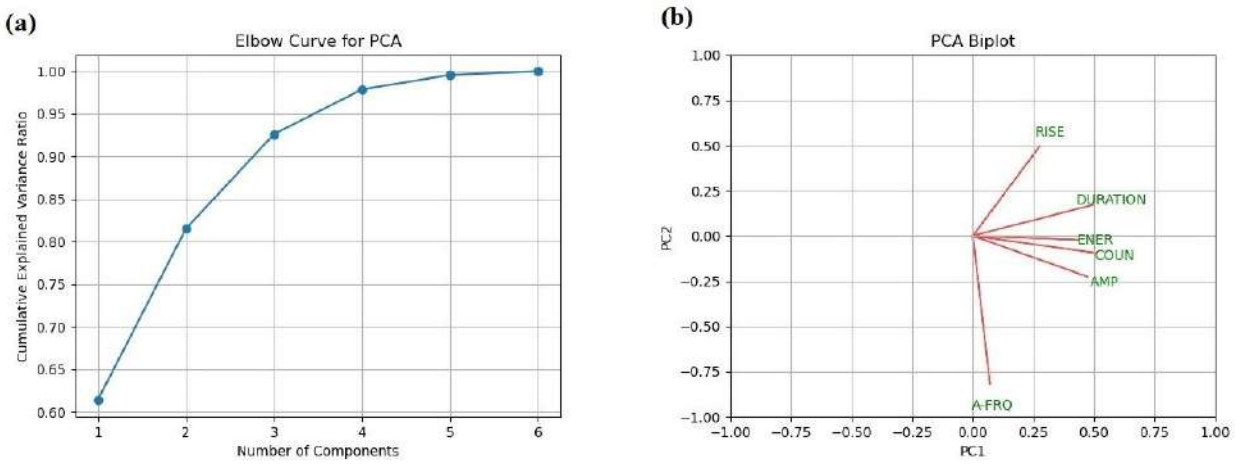

Figure IV-9: (a) Elbow curve for PCA and (b) PCA biplot.

The simplification of the feature space into two most important axes and the SEM (**Figure III.4**) observation of fracture faces enables an easy classification and discriminant analysis of two damage classes observed for neat PLA (matrix cracking and matrix/matrix friction) and four damage classes for biocomposite damage (matrix cracking, matrix/matrix friction, fiber debonding, fiber pull-out). The 2D representation aids in the understanding of the patterns of the clusters from the data and explains the model validation in terms of the variables and types of damages. Each of these classes is simply a specific type of damage that can take place in composite materials.

IV.5.6 Damage identification

The damage evolution in the L.S/PLA biocomposite under the tensile test was analyzed using AE. To better identify the damage mechanisms of composites, we need to evaluate the damage mechanisms of neat PLA alone. **Figure IV.11(a)** shows the stress, amplitude, and cumulative energy versus time with the different damage classes for neat PLA. This figure illustrates a brittle behaviour of PLA under load. The analysis of the AE data reveals two distinct phases corresponding to different deformation regimes and damage mechanisms: In Phase I (up to 239 s), PLA exhibits a linear increase in stress with time, characteristic of elastic behaviour. The corresponding AE events are likely caused by the initiation of microcracks in the polymer matrix. These cracks form but do not yet propagate, resulting in emissions of low amplitude and energy. In Phase II, the increase in AE toward the end of this phase indicates that the initial cracks are beginning to propagate rapidly through the matrix, a precursor to impending failure. Matrix/matrix friction also occurs at this stage as the crack faces interact under increasing stress.

At the failure point, characterised by the sudden drop in stress and the abrupt increase in AE, we can infer that critical failure events occur. The sharp increase in acoustic energy at this point is

characteristic of major fractures within the material, coinciding with the loss of structural integrity of the PLA. Baran et al.[121] noted that no accumulation of AE energy could be observed during the loading of carbon fibre reinforced polymer composites CFRP with brittle behaviour, and all recorded AE signals appeared only at the time of final failure.

Unlike PLA, which exhibits brittle behaviour, the composites showed ductile behaviour through mechanical tests, confirmed by an increase in tensile strain from 1.61% for PLA to 2.03% for the biocomposite. This behaviour change is attributable to the positive effect of the fibres, which introduce two new modes of damage to the composite: fibre debonding and fibre pull-out. **Figure IV.11(c)** shows the stress, amplitude, and cumulative energy versus time with the different damage classes for the tensile test, where at least four main failure modes can be distinguished by the AE signals. In the first phase (elastic region) up to 204 s (**Figure IV.11(c)**), the material behaves elastically, and the cumulative energy curve remains relatively flat or increases very slowly, indicating slight AE and corresponding to minimal damage. This part coincides with the linear portion of the stress–strain curve. In the second phase (the onset of plastic damage), between 204 and 293 s, the material exceeds the elastic yield point and begins to deform plastically. AE events become more frequent, signaling the onset of internal damage mechanisms. The cumulative energy curve slopes upward, indicating an increase in energy release due to phenomena such as matrix cracking, matrix/matrix friction and the presence of some fibre-debonding events. In the third phase (damage progression), as deformation continues, acoustic events become more numerous and energy release increases, indicating worsening damage. A new damage mechanism, fibre pull-out, may also appear. The cumulative energy curve becomes steeper, signifying that damage mechanisms such as matrix cracking, matrix/matrix friction, fibre debonding, and fibre pull-out

are all active. The rapid propagation of cracks leads to a peak in energy release, suggesting a critical phase potentially preceding final material failure.

Figure IV.11(b) and **(d)** illustrate the correlation between the duration of AE signals and damage mechanisms in neat PLA and L.S/PLA composite. For all materials, matrix cracking signals are concentrated in the lower left, suggesting a multitude of short and possibly less severe events. Matrix/matrix friction has a more extended distribution in duration, indicating variability in energy release during this phenomenon. In the L.S/PLA composite, fibre-debonding events, which are less frequent but longer, suggest significant energy release, typical of the separation of fibres from the matrix, leading to pull-out.

Figure IV.12(a) and **(b)** present 3D plots illustrating the correlation between frequency, amplitude, and duration across two damage classes for neat PLA and four damage classes for L.S/PLA composite, respectively, specifying the percentage represented by each class. For the neat PLA, the matrix cracking was characterised by acoustic amplitudes ranging from 35 to 46 dB, accounting for 76.42% of the detected events, and matrix/matrix friction, with acoustic amplitudes ranging from 47 to 54 dB, accounting for 23.58% of the events. In the tensile test, four damage classes were observed: matrix cracking, with acoustic amplitudes ranging from 35 to 46 dB, accounting for 66.5% of the detected events; matrix/matrix friction, with acoustic amplitudes ranging from 47 to 54 dB, accounting for 24.5% of the events; fibre debonding, with amplitudes from 55 to 63 dB, representing 7.6% of the events; and fibre pull-out, with amplitudes from 64 to 85 dB, constituting 1.3% of the events.

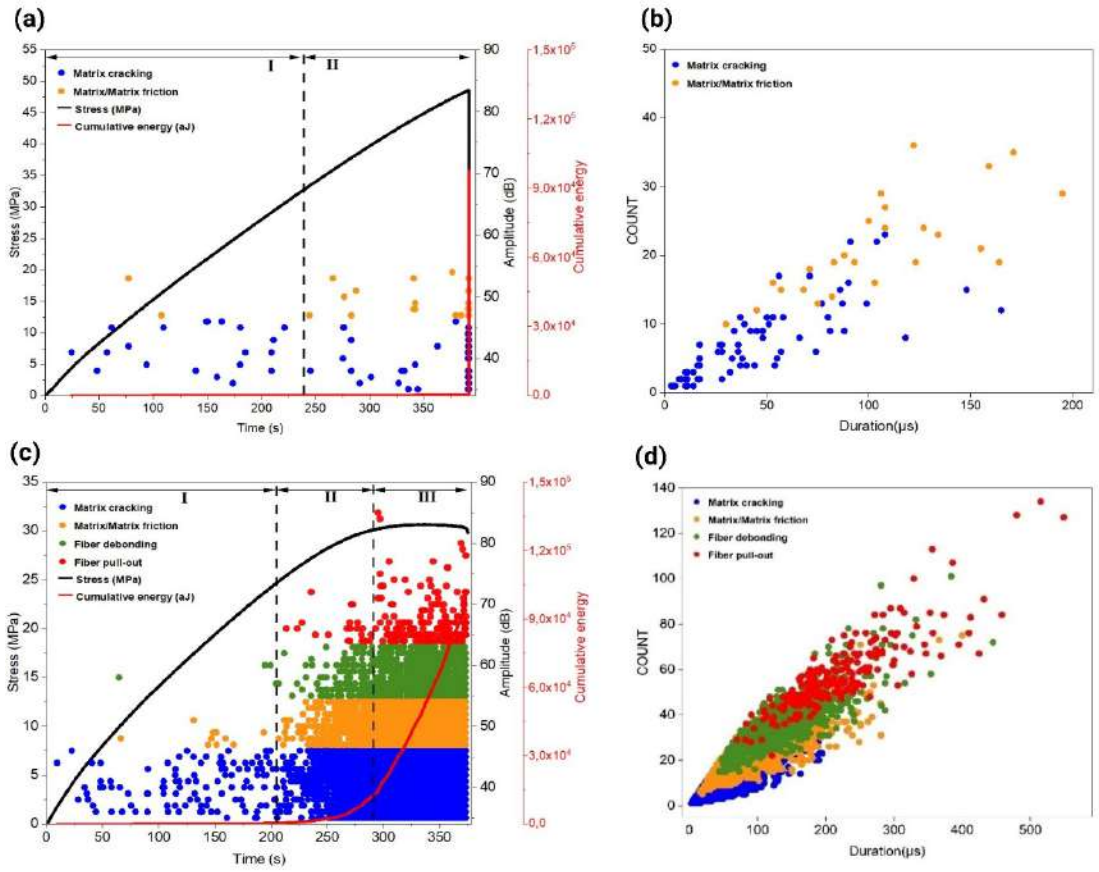

Figure IV-10: Stress, amplitude, and cumulative energy versus time with the different damage classes in the tensile test: (a) and (b) neat PLA, (c) and (d) L.S/PLA biocomposite.

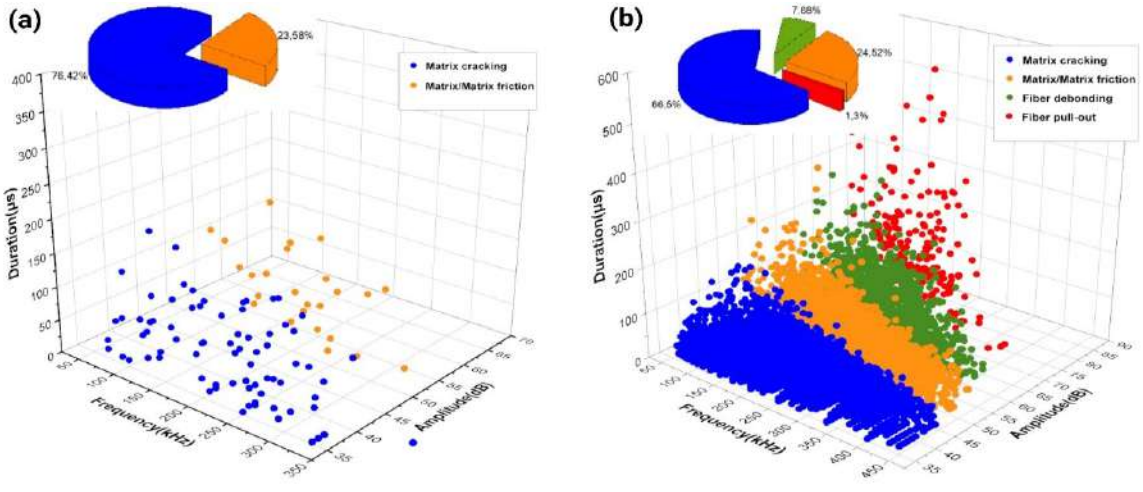

Figure IV-11: 3D plot of the AE events in the tensile test: (a) neat PLA, (b) L.S/PLA biocomposite.

IV.6 Mechanical Properties Prediction Using Machine Learning: Methodology Overview

The method provided in **Figure IV.13** explains the steps that are followed in predicting the stress levels using acoustic emission (AE) signals obtained from the tensile and flexural tests. AE data is divided into training set and testing set for model training and performance evaluation, respectively.

Two distinct techniques were used to evaluate the performance of the prediction model: Hold-Out Testing, which utilizes a portion of the data set for the purpose of testing, and 5-Fold Cross Validation (CV), which partitions the original data set into five separate subsets that are used for training and testing. By using these different methods, the ANN model developed is able to accurately gauge stress levels in different approaches providing a valuable information regarding the materials behavior and its respond to stress.

Figure IV-12: Machine learning prediction methodology.

IV.6.1 Descriptive Statistics

The input data for stress level prediction comprises of AE features: cumulative energy, amplitude, duration, frequency, rise and counts as well as levels of mechanical stresses from tension and flexural tests. This combined dataset is crucial for the ML models training to correlate AE signals with the stress levels.

Table IV.8 and **Table IV.8** summaries the AE features derived from the tensile and flexural tests, respectively, with special attention to the AE features and mechanical properties needed to estimate stress levels for both tests.

Table IV-8: presents a statistical summary of tensile stress and its corresponding EA data.

	Stress_MPa	CUM_COUNT	CUM_ENERGY	CUM_RISE	CUM_DURATION	CUM_AMPLITUDE	CUM_FREQUENCY
count	10436	10436	10436	10436	10436	10436	10436
mean	30.79	56944.27	19601.65	60373.19	233473.1	219894.4	1232906.03
std	0.83	32446.02	11145.77	34505.12	133872.4	126563.4	702596.31
min	24.20	13	3	10	47	47	277
25%	30.79	28791	9948	30112.25	116803.8	110462.8	631068
50%	31.05	57451.5	19807	60600	234905	220105.5	1237443
75%	31.19	84492.5	28921.5	89581.5	346821	329270.5	1840033.5
max	31.45	112935	39281	120715	467734	438660	2432094

Table IV-9: presents a statistical summary of flexural stress and its corresponding AE data.

	Stress_MPa	CUM_COUNT	CUM_ENERGY	CUM_RISE	CUM_DURATION	CUM_AMPLITUDE	CUM_FREQUENCY
count	2068	2068	2068	2068	2068	2068	2068
mean	54.02	15744.11	5525.93	17987.14	68603.15	45327.47	232244.85
std	4.63	9076.90	3184.93	10610.84	39623.21	26161.85	133838.30
min	33.30	9	2	7	68	39	132
25%	51.04	7847	2723.5	8794	33744	22619	117580.5
50%	55.35	15630	5514	17566	68390	45336.5	230682
75%	57.78	23721.25	8338.75	27172.5	103537	68017	347790.5
max	60.17	31242	10926	36615	136922	90437	462722

IV.6.2 Artificial Neural Network (ANN)

Artificial Neural Networks (ANNs) performing recognition of patterns and making predictions by imitating the way the brain works. In material science, ANNs process complex data sets for predicting properties or damage mechanisms based on certain input features such as amplitude, energy, frequency and duration of AE signals and the mechanical characteristics gathered during the mechanical testing.

Figure IV.14 shows the ANN model's structure:

1. First is the input layer which consists of AE features and every node corresponds to one feature.
2. Moving on to the hidden layers where the neurons are connected to each other and the appropriate activation functions are used. The number of layers can vary with the complexity of the model.
3. Finally, the output layer generates the last prediction, which can be a damage class or estimate on the material porosity.

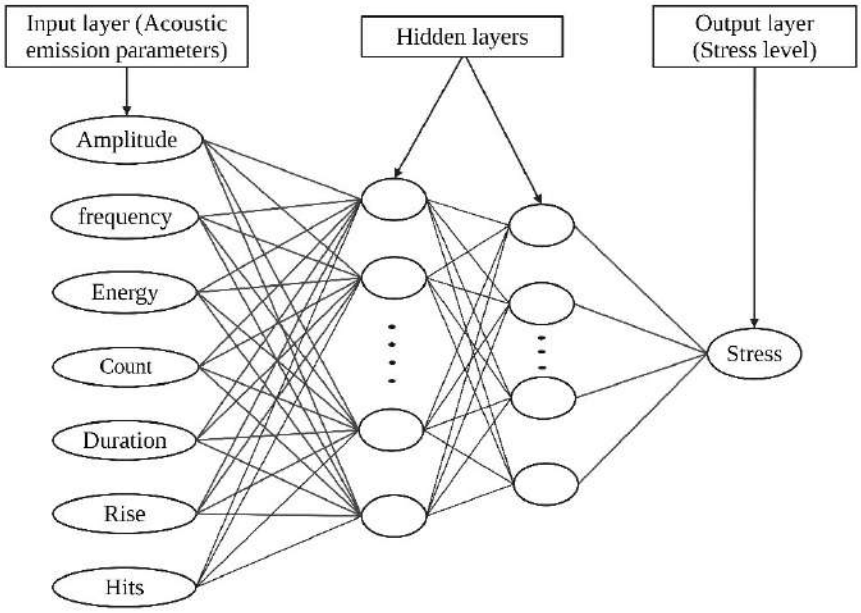

Figure IV-13: the ANN model for stress level prediction based on AE data inputs.

IV.6.3 Prediction of Stress Level Using Artificial Neural Network (ANN)

This research employs an ANN model to assess the stress level of Lygeum spartum/PLA biocomposite samples under mechanical loading, taking into account AE data from tensile and flexural tests. Achieving the best accuracy involved refining model input parameters through feature selection, outlier elimination, and combined analysis of AE and mechanical data. The architecture of the ANN was highly optimized, so it was balanced between complexity and generalization [122].

During tensile testing **Figure IV.15(a)**, the ANN had an R2 of 0.9808 and an MSE of 0.014, allowing the assumption of accurate predictions. During flexural testing **Figure IV.15(b)**, the R2 were slightly lower at 0.9681 and an MSE of 0.6490,the reduction of the accuracy in the case of flexural testing probably due to the difference in stress concentration during flexural loading [123, 124].

Tensile tests had an average MSE of 0.0221 and R^2 of 0.9687, whereas flexural tests had an average MSE of 0.9182 and R^2 of 0.9575. The model exhibited significantly different AE responses for distinct load states which validates the strength of the model according to cross-validation results. Crucial to the model's prediction of tensile tests, these results showcase the multi-faceted AE response relevant for accurate representation of biocomposite load behavior [125].

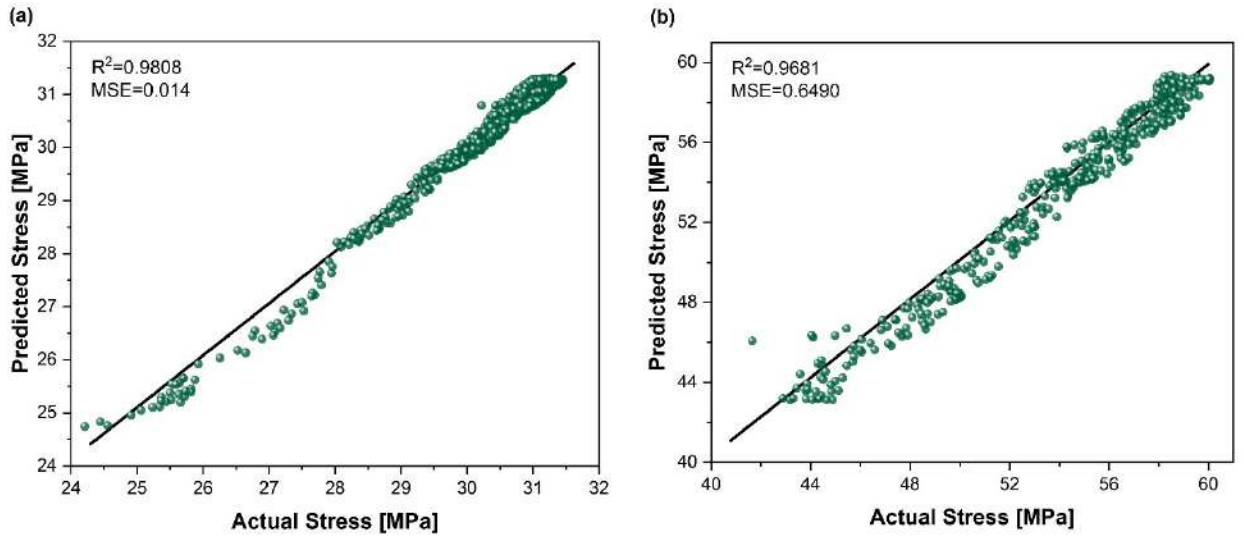

Figure IV-14: Stress levels predicted by the ANN algorithm (a) tensile test and (b) flexural test.

IV.7 Conclusion

In this chapter, the L.S/PLA and the neat PLA specimens were examined for their mechanical properties using destructive and non-destructive techniques. The tensile and flexural testing showed an enhancement due to the incorporation of the lygeum fibers. Regarding the NDT Digital Image Correlation (DIC) provided precise measurements of strain distribution and the concentration of the stress. The Impulse Excitation Technique (IET) was used in the flexural testing, and it demonstrated as a fast and reliable technique for the determination of the elasticity modulus. In addition, the Acoustic Emission (AE) was used for the identification of the damage modes and the track of the damage progression. Machine learning models were used to track the stress level under both test conditions and for the classification of the damage modes. The biocomposite demonstrates its role as an alternative for the synthetic carbon and glass fibers and the potential of the use of these biobased fibers for the enhancement of the mechanical properties in some manufacturing processes like 3D printing.

General Conclusion

General Conclusion

This investigation gives a detailed analysis of the mechanical response and damage mechanisms of Lygeum spartum (L.S) fiber reinforced PLA biocomposites manufactured by 3D printing techniques. several experimental techniques used to assess the physical, thermal, mechanical, and microstructural properties of the biocomposite material. This research develops understanding for the plant based fibers' interactions with polymer matrices, and particularly identifies the Lygeum spartum function, thus, being able to use it as eco-friendly substitutes to some of the synthetic fibers used in composite structures.

The research commenced with the extraction and treatment of Lygeum spartum fibers, which included an alkaline treatment with NaOH that partially enhanced fiber-matrix adhesion. This step was necessary to modify the surface of the fibers in order to make the hydrophilic fibers more amenable to the hydrophobic PLA matrix. The fibers were then grounded, sieved, and blended with PLA to produce biocomposite pellets. The biocomposite pellets were extruded into filaments which were used to fabricate specimens for tensile and flexural tests by using Fused Deposition Modeling (FDM). Furthermore, the biocomposite exhibited better print quality and surface finish, especially with less defects and lower levels of stringing compared to neat PLA, which suggested the potential of employing L.S fibers in additive manufacturing.

The effective chemical bonding of the PLA matrix with L.S fibers was confirmed by Fourier-transform infrared (FTIR) spectroscopy, and fiber-matrix interactions were enhanced as peak intensities significantly changed. The analyses of the density and porosity revealed that while the biocomposite possessed desirable mechanical properties, it also maintained a lightweight structure making it a promising material for structural application. The performed thermal analysis (TGA and DSC) indicates that the incorporation of L.S fibers influenced the thermal stability of the composite due to the natural sensibility the fibers possess. As a consequence, the onset degradation temperature was lower than that of neat PLA. It was noted, however, that the fibers served as nucleating agents thereby enhancing the crystallinity of the PLA matrix which in turn augmented its mechanical properties.

Regarding the mechanical characterization It was shown that adding L.S fibers to the composite improved its ductility, mitigating PLA's brittleness. An efficient stress transfer from the fibers to

the matrix and the fiber reinforcement resulted in considerable gains in the flexural modulus and ultimate stress in the flexural tests. While the tensile strength of the biocomposite was lower than that of the neat PLA, this is related to the heterogeneous dispersion of fibers within the matrix. However, the increased strain capacity of the biocomposite suggests that it is capable of attaining higher amounts of deformation energy, which makes it ideal for use in areas that require flexibility.

Critical insights into the mechanical behavior and damage progression of Lygeum spartum/PLA biocomposites were obtained through advanced non-destructive IET, DIC and AE monitoring techniques. IET has shown that embedding fiber increased the stiffness of the material, while DIC captured strain and distributions on the specimens which revealed important failure modes during the tensile and flexural tests. using AE, matrix cracking, matrix-matrix friction, and fiber debonding/pull-out were classified as the main damage mechanisms and were defined by their own sets of amplitude ranges. using an ANN model the stress level under the mechanical loading was predicted and showed a promising results demonstrating the value of the AE as a way for the prediction of the mechanical characteristics and to monitor the health of the composite materials.

In this study, the objective was accomplished by combining classical methods and advanced non-destructive techniques along with machine learning based models to assess the mechanical properties of 3D-printed biocomposites. This work serves as the foundation for new engineering grade sustainable materials by integrating conventional testing with advanced spectral non-destructive techniques for the evaluation of composite materials.

References

1. Chawla, N. and Y.L.J.A.e.m. Shen, *Mechanical behavior of particle reinforced metal matrix composites.* 2001. **3**(6): p. 357-370.
2. Karger-Kocsis, J., *Thermoplastic rubbers via dynamic vulcanization*, in *Polymer blends and alloys*. 2019, Routledge. p. 125-154.
3. Kim, J.-K. and Y.-W. Mai, *Engineered interfaces in fiber reinforced composites*. 1998: Elsevier.
4. Han, S.H., H.J. Oh, and S.S.J.C.P.B.E. Kim, *Evaluation of fiber surface treatment on the interfacial behavior of carbon fiber-reinforced polypropylene composites.* 2014. **60**: p. 98-105.
5. Kim, J.-H., et al., *The evaluation of the interfacial and flame retardant properties of glass fiber/unsaturated polyester composites with ammonium dihydrogen phosphate.* 2019. **167**: p. 221-230.
6. Singh, B., R. Kumar, and J.S. Chohan, *Polymer matrix composites in 3D printing: A state of art review.* Materials Today: Proceedings, 2020. **33**: p. 1562-1567.
7. Belouadah, Z., A. Ati, and M. Rokbi, *Characterization of new natural cellulosic fiber from Lygeum spartum L.* Carbohydrate polymers, 2015. **134**: p. 429-437.
8. Le Corre, D., N. Tucker, and M. Staiger, *Electrospun cellulosic fibre-reinforced composite materials*, in *Natural Fibre Composites*. 2014, Elsevier. p. 115-158.
9. Saber, D. and A. Abdelnaby, *Recent developments in natural fiber as reinforcement in polymeric composites: a review.* Recent Developments in Natural Fiber as Reinforcement in Polymeric Composites: A Review (October 19, 2022). D. Saber & AH Abdelnaby" Recent Developments in Natural Fiber as Reinforcement in Polymeric Composites: A Review" Asian Journal of Applied Science and Technology (AJAST) Volume, 2022. **6**: p. 56-75.
10. Reddy, N. and Y.J.T.i.B. Yang, *Biofibers from agricultural byproducts for industrial applications.* 2005. **23**(1): p. 22-27.
11. Mohanty, A.K., et al., *Sustainable bio-composites from renewable resources: opportunities and challenges in the green materials world.* 2002. **10**: p. 19-26.
12. Chai, Y.D., et al., *Recent progress on tailoring the biomass-derived cellulose hybrid composite photocatalysts.* Polymers, 2022. **14**(23): p. 5244.
13. Klemm, D., et al., *Cellulose: fascinating biopolymer and sustainable raw material.* 2005. **44**(22): p. 3358-3393.
14. Moon, R.J., et al., *Cellulose nanomaterials review: structure, properties and nanocomposites.* 2011. **40**(7): p. 3941-3994.
15. Sjostrom, E., *Wood chemistry: fundamentals and applications*. 2013: Elsevier.
16. Popescu, M.-C., B.-I. Dogaru, and C.-M.J.M. Popescu, *Effect of cellulose nanocrystals nanofiller on the structure and sorption properties of carboxymethyl cellulose–glycerol–cellulose nanocrystals nanocomposite systems.* 2020. **13**(13): p. 2900.
17. Ebringerová, A. and Z.J.C.E.J.o.C. Hromádková, *An overview on the application of ultrasound in extraction, separation and purification of plant polysaccharides.* 2010. **8**: p. 243-257.
18. Gatenholm, P. and D.J.M.b. Klemm, *Bacterial nanocellulose as a renewable material for biomedical applications.* 2010. **35**(3): p. 208-213.
19. Glasser, W.G.J.F.i.c., *About making lignin great again—some lessons from the past.* 2019. **7**: p. 565.
20. Terashima, N., et al., *2D-NMR (HSQC) difference spectra between specifically 13C-enriched and unenriched protolignin of Ginkgo biloba obtained in the solution state of whole cell wall material.* 2009.
21. Voragen, A.G., et al., *Pectin, a versatile polysaccharide present in plant cell walls.* 2009. **20**: p. 263-275.

22. Willats, W.G., et al., *Pectin: new insights into an old polymer are starting to gel.* 2006. **17**(3): p. 97-104.
23. Rinaudo, M.J.A.i.P.P.o.B., *Sol and gel based on polysaccharide: Characterization and structure-properties relationship.* 2017: p. 229-280.
24. Carrión, J.S., et al., *Ancient Forests in European drylands: Holocene palaeoecological record of Mazarrón, south-eastern Spain.* 2018. **129**(4): p. 512-525.
25. Belouadah, Z., A. Ati, and M.J.C.p. Rokbi, *Characterization of new natural cellulosic fiber from Lygeum spartum L.* 2015. **134**: p. 429-437.
26. Nedjimi, B.J.T.R.J., *Lygeum spartum L.: a review of a candidate for West Mediterranean arid rangeland rehabilitation.* 2016. **38**(5): p. 493-499.
27. Bledzki, A. and J.J.P.i.p.s. Gassan, *Composites reinforced with cellulose based fibres.* 1999. **24**(2): p. 221-274.
28. Mohanty, A., et al., *Biofibres, biodegradable polymers and biocomposites: An overview.* 2000. **276**(1): p. 1-24.
29. Thakur, V.K. and M.K.J.C.p. Thakur, *Processing and characterization of natural cellulose fibers/thermoset polymer composites.* 2014. **109**: p. 102-117.
30. Belgacem, M.N. and A. Gandini, *Surface modification of cellulose fibres*, in *Monomers, polymers and composites from renewable resources*. 2008, Elsevier. p. 385-400.
31. Kalia, S., et al., *Pretreatments of natural fibers and their application as reinforcing material in polymer composites—a review.* 2009. **49**(7): p. 1253-1272.
32. Mohanty, A., M. Misra, and L.T.J.C.i. Drzal, *Surface modifications of natural fibers and performance of the resulting biocomposites: An overview.* 2001. **8**(5): p. 313-343.
33. Ray, D., et al., *The mechanical properties of vinylester resin matrix composites reinforced with alkali-treated jute fibres.* 2001. **32**(1): p. 119-127.
34. Mwaikambo, L.Y. and M.P.J.D.a.m.C. Ansell, *The effect of chemical treatment on the properties of hemp, sisal, jute and kapok for composite reinforcement.* 1999. **272**(1): p. 108-116.
35. Sreekala, M., M. Kumaran, and S.J.J.o.A.p.s. Thomas, *Oil palm fibers: Morphology, chemical composition, surface modification, and mechanical properties.* 1997. **66**(5): p. 821-835.
36. Le Troedec, M., et al., *Influence of various chemical treatments on the composition and structure of hemp fibres.* 2008. **39**(3): p. 514-522.
37. Jacob, M., et al., *A study of advances in characterization of interfaces and fiber surfaces in lignocellulosic fiber-reinforced composites.* 2005. **12**(1-2): p. 95-124.
38. Alvarez, V.A., A.J.C.P.A.A.S. Vázquez, and Manufacturing, *Influence of fiber chemical modification procedure on the mechanical properties and water absorption of MaterBi-Y/sisal fiber composites.* 2006. **37**(10): p. 1672-1680.
39. Elkhaoulani, A., et al., *Mechanical and thermal properties of polymer composite based on natural fibers: Moroccan hemp fibers/polypropylene.* 2013. **49**: p. 203-208.
40. Liu, Y., et al., *A comprehensive review of recent advances in delignification technology.* 2024. **115**(12): p. 2489-2504.
41. Madhu, P., et al., *A review on synthesis and characterization of commercially available natural fibers: Part-I.* 2019.
42. Agarwal, B., et al., *Analysis and performance of fiber composites Second edition*. 1990: John Wiley & Sons.
43. Chawla, K., *Composite materials: science and engineering*. Vol. 1. 2012: Springer.
44. Young, R.J. and P.A. Lovell, *Introduction to polymers*. 2011: CRC press.
45. Hua, W., et al., *3D printing of biodegradable polymer vascular stents: A review.* 2022. **1**(2): p. 100020.

46. Mangaraj, S., et al., *Development and characterization of PLA and Cassava starch-based novel biodegradable film used for food packaging application.* 2022. **46**(9): p. e16314.
47. Gangolphe, L., et al., *Electrospun microstructured PLA-based scaffolds featuring relevant anisotropic, mechanical and degradation characteristics for soft tissue engineering.* 2021. **129**: p. 112339.
48. Fattahi, F.S., et al., *Sustainable, renewable, and biodegradable poly (lactic acid) fibers and their latest developments in the last decade.* 2020: p. 173-194.
49. Trivedi, A.K., et al., *PLA based biocomposites for sustainable products: A review.* 2023. **6**(4): p. 382-395.
50. Pearce, J.M.J.J.o.M. and M. Processing, *Distributed manufacturing of open source medical hardware for pandemics.* 2020. **4**(2): p. 49.
51. Willson, K., A.J.A.R.o.C. Atala, and B. Engineering, *Medical 3D printing: tools and techniques, today and tomorrow.* 2022. **13**(1): p. 481-499.
52. Shaik, Y., J. Schuster, and A. Shaik, *A scientific review on various pellet extruders used in 3D printing FDM processes. OALib. 08: 1–19*. 2021.
53. Huang, Y., et al., *Additive manufacturing: current state, future potential, gaps and needs, and recommendations.* 2015. **137**(1): p. 014001.
54. Kruth, J.-P., M.-C. Leu, and T.J.C.A. Nakagawa, *Progress in additive manufacturing and rapid prototyping.* 1998. **47**(2): p. 525-540.
55. Nazir, A. and J.-Y.J.P.o.t.I.o.M.E. Jeng, Part C: Journal of Mechanical Engineering Science, *A high-speed additive manufacturing approach for achieving high printing speed and accuracy.* 2020. **234**(14): p. 2741-2749.
56. Mazumder, J., et al., *Closed loop direct metal deposition: art to part.* 2000. **34**(4-6): p. 397-414.
57. Cruz Sanchez, F., et al., *Polymer recycling in an open-source additive manufacturing context: mechanical issues. Addit Manuf 17: 87–105*. 2017.
58. Ohtsu, M., *Acoustic emission and related non-destructive evaluation techniques in the fracture mechanics of concrete: fundamentals and applications*. 2020: Woodhead Publishing.
59. Ferdinánd, M., et al., *Impact modification of wood flour reinforced PP composites: Problems, analysis, solution.* 2023. **167**: p. 107445.
60. Marec, A., J.-H. Thomas, and R. El Guerjouma, *Contrôle de santé des matériaux hétérogènes par émission acoustique et acoustique non linéaire: discrimination des mécanismes d'endommagement et estimation de la durée de vie restante*. 2008, Laboratoire d'Acoustique de L'université du Mans.
61. Roebben, G., et al., *Impulse excitation apparatus to measure resonant frequencies, elastic moduli, and internal friction at room and high temperature.* 1997. **68**(12): p. 4511-4515.
62. Brebels, A. and B.J.T.e.-J.o.N.T. Bollen, *Non-destructive evaluation of material properties as function of temperature by the Impulse Excitation Technique.* 2015. **20**(6).
63. Anand Kumar, S. and Y. Shivraj Narayan. *Tensile testing and evaluation of 3D-printed PLA specimens as per ASTM D638 type IV standard*. in *Innovative Design, Analysis and Development Practices in Aerospace and Automotive Engineering (I-DAD 2018) Volume 2*. 2019. Springer.
64. Standard, A., *Standard test methods for flexural properties of unreinforced and reinforced plastics and electrical insulating materials. ASTM D790.* Annual book of ASTM standards, 1997.
65. Monti, A., et al., *Mechanical behaviour and damage mechanisms analysis of a flax-fibre reinforced composite by acoustic emission.* Composites Part A: Applied Science and Manufacturing, 2016. **90**: p. 100-110.
66. Mandala, R., et al., *A short review on fused deposition modeling 3D printing of bio-based polymer nanocomposites.* Journal of Applied Polymer Science, 2022. **139**(14): p. 51904.

67. Diederichs, E., et al., *Extrusion based 3D printing of sustainable biocomposites from biocarbon and poly (trimethylene terephthalate).* Molecules, 2021. **26**(14): p. 4164.
68. Cai, Y., J. Lv, and J. Feng, *Spectral characterization of four kinds of biodegradable plastics: poly (lactic acid), poly (butylenes adipate-co-terephthalate), poly (hydroxybutyrate-co-hydroxyvalerate) and poly (butylenes succinate) with FTIR and raman spectroscopy.* Journal of Polymers and the Environment, 2013. **21**: p. 108-114.
69. Tarique, J., S.M. Sapuan, and A.J.J.o.N.F. Khalina, *Extraction and characterization of a novel natural lignocellulosic (bagasse and husk) fibers from arrowroot (Maranta arundinacea).* 2022. **19**(15): p. 9914-9930.
70. Auras, R., B. Harte, and S.J.M.b. Selke, *An overview of polylactides as packaging materials.* 2004. **4**(9): p. 835-864.
71. Jose, C., et al., *Adhesion and surface issues in biocomposites and bionanocomposites: a critical review.* 2014. **2**(2).
72. Kumar, A., et al., *Utilization of banana peel as bio-filler to develop bio-composite materials and characterize their physical, mechanical, thermal, and tribological characteristics.* 2024. **81**(17): p. 16175-16196.
73. Izani, M.N., et al., *Effects of fiber treatment on morphology, tensile and thermogravimetric analysis of oil palm empty fruit bunches fibers.* 2013. **45**(1): p. 1251-1257.
74. González-Díaz, E. and J.-M.J.J.o.C.H. Alonso-López, *Characterization by thermogravimetric analysis of the wood used in Canary architectural heritage.* 2017. **23**: p. 111-118.
75. Kabir, M., et al., *Mechanical properties of chemically-treated hemp fibre reinforced sandwich composites.* 2012. **43**(2): p. 159-169.
76. Zhu, R., et al., *Compatibilizing effects of maleated poly (lactic acid)(PLA) on properties of PLA/soy protein composites.* 2012. **51**(22): p. 7786-7792.
77. Sonawane, S., P. Thakur, and R. Paul, *Study on thermal property enhancement of MWCNT based polypropylene (PP) nanocomposites.* Materials Today: Proceedings, 2020. **27**: p. 550-555.
78. Werchefani, M., et al., *Enzyme-treated Tunisian Alfa fibers reinforced polylactic acid composites: An investigation in morphological, thermal, mechanical, and water resistance properties.* Polymer Composites, 2020. **41**(5): p. 1721-1735.
79. Guo, R., et al., *Effect of toughening agents on the properties of poplar wood flour/poly (lactic acid) composites fabricated with Fused Deposition Modeling.* European Polymer Journal, 2018. **107**: p. 34-45.
80. Daver, F., et al., *Cork–PLA composite filaments for fused deposition modelling.* Composites Science and Technology, 2018. **168**: p. 230-237.
81. Martin, A.R., et al., *Studies on the thermal properties of sisal fiber and its constituents.* Thermochimica Acta, 2010. **506**(1-2): p. 14-19.
82. Diederichs, E., et al., *Extrusion based 3D printing of sustainable biocomposites from biocarbon and poly (trimethylene terephthalate).* 2021. **26**(14): p. 4164.
83. Liu, H., et al., *Three-dimensional printing of poly (lactic acid) bio-based composites with sugarcane bagasse fiber: Effect of printing orientation on tensile performance.* 2019. **30**(4): p. 910-922.
84. Niresh, J., et al., *Physical, chemical, morphological and thermal characterisation of natural fibers for sound absorption.* 2019. **29**(3): p. 219-227.
85. dos Santos, N.V., et al., *Analysis of voids, interfacial and thermal properties of additively manufactured continuous natural fiber-reinforced biocomposites.* 2024: p. 1-22.
86. Sgriccia, N., M.J.C.S. Hawley, and Technology, *Thermal, morphological, and electrical characterization of microwave processed natural fiber composites.* 2007. **67**(9): p. 1986-1991.
87. Sanivada, U.K., et al., *PLA composites reinforced with flax and jute fibers—A review of recent trends, processing parameters and mechanical properties.* 2020. **12**(10): p. 2373.

88. Agaliotis, E.M., et al., *Tensile behavior of 3D printed polylactic acid (PLA) based composites reinforced with natural fiber.* 2022. **14**(19): p. 3976.
89. Lv, C., et al., *The mechanical properties of plant fiber-reinforced geopolymers: A review.* 2022. **14**(19): p. 4134.
90. Lee, C.H., A. Khalina, and S.H.J.P. Lee, *Importance of interfacial adhesion condition on characterization of plant-fiber-reinforced polymer composites: A review.* 2021. **13**(3): p. 438.
91. Kovan, V., et al., *Effect of printing parameters on mechanical properties of 3D printed PLA/carbon fibre composites.* 2018. **4**(4): p. 126-128.
92. Kovan, V., et al., *Printing parameters effect on surface characteristics of 3D printed PLA materials.* 2018. **12**(7): p. 266-269.
93. Murariu, A.C., et al., *Influence of 3D printing parameters on mechanical properties of the PLA parts made by FDM additive manufacturing process.* 2022. **2**: p. 7-20.
94. Ahn, S.H., et al., *Anisotropic material properties of fused deposition modeling ABS.* 2002. **8**(4): p. 248-257.
95. Yadlapati, S.A., *Influence of FDM build parameters on tensile and compression behaviors of 3D printed polymer lattice structures.* 2018.
96. Domingo-Espin, M., et al., *Mechanical property characterization and simulation of fused deposition modeling Polycarbonate parts.* 2015. **83**: p. 670-677.
97. Chacón, J.M., et al., *Additive manufacturing of PLA structures using fused deposition modelling: Effect of process parameters on mechanical properties and their optimal selection.* 2017. **124**: p. 143-157.
98. Tao, Y., et al., *Development and application of wood flour-filled polylactic acid composite filament for 3D printing.* Materials, 2017. **10**(4): p. 339.
99. Le Duigou, A., et al., *3D printing of wood fibre biocomposites: From mechanical to actuation functionality.* Materials & Design, 2016. **96**: p. 106-114.
100. Bianchi, I., et al., *Comparison between the mechanical properties and environmental impacts of 3D printed synthetic and bio-based composites.* Procedia CIRP, 2022. **105**: p. 380-385.
101. Ayrilmis, N., et al., *Effect of printing layer thickness on water absorption and mechanical properties of 3D-printed wood/PLA composite materials.* The International Journal of Advanced Manufacturing Technology, 2019. **102**: p. 2195-2200.
102. Montalvo Navarrete, J.I., et al., *Thermal and mechanical behavior of biocomposites using additive manufacturing.* International Journal on Interactive Design and Manufacturing (IJIDeM), 2018. **12**: p. 449-458.
103. Stoof, D., K. Pickering, and Y. Zhang, *Fused deposition modelling of natural fibre/polylactic acid composites.* Journal of Composites Science, 2017. **1**(1): p. 8.
104. Mazur, K.E., et al., *Mechanical, thermal and microstructural characteristic of 3D printed polylactide composites with natural fibers: wood, bamboo and cork.* Journal of Polymers and the Environment, 2022. **30**(6): p. 2341-2354.
105. Figueroa-Velarde, V., et al., *Mechanical and physicochemical properties of 3d-printed agave fibers/poly (Lactic) acid biocomposites.* Materials, 2021. **14**(11): p. 3111.
106. Scaffaro, R., et al., *Green composites based on biodegradable polymers and anchovy (Engraulis Encrasicolus) waste suitable for 3D printing applications.* Composites Science and Technology, 2022. **230**: p. 109768.
107. Ashby, M.F. and D.J.L.J.d.P.I. Cebon, *Materials selection in mechanical design.* 1993. **3**(C7): p. C7-1-C7-9.
108. Foroozanfar, A., et al., *Experimental and Computational Analysis of Elastic Modulus of 3D Printed Parts Using Impulse Excitation Technique (IET).* 2023. **47**(4): p. 787-795.

109. Rech, J., et al., *COMPARISON OF YOUNG'S MODULI DETERMINED BY IMPULSE EXCITATION TECHNIQUE (IET), DYNAMIC MECHANICAL ANALYSIS (DMA) AND TENSILE TEST (TT).*
110. Sutton, M.A., *Digital image correlation for shape and deformation measurement.* Springer handbook of experimental solid mechanics, 2008: p. 565-600.
111. Schreier, H.W. and M.A. Sutton, *Systematic errors in digital image correlation due to undermatched subset shape functions.* Experimental mechanics, 2002. **42**: p. 303-310.
112. Pan, B., et al., *Two-dimensional digital image correlation for in-plane displacement and strain measurement: a review.* Measurement science and technology, 2009. **20**(6): p. 062001.
113. Guessasma, S., H. Nouri, and S. Belhabib, *Digital image correlation and finite element computation to reveal mechanical anisotropy in 3D printing of polymers.* Materials, 2022. **15**(23): p. 8382.
114. Tariq, F., et al. *Application of Digital Image Correlation Technique in determination of elastic constants of materials*. in *MatTect'12 All Pakistan Conference on Materials Technology, ASM—GIKI Student ChapterAt: GIK Institute of Engineering Sciences and Technology*. 2012.
115. Hamstad, M.A., *A review: acoustic emission, a tool for composite-materials studies.* Experimental mechanics, 1986. **26**: p. 7-13.
116. Aghighi, F., et al., *Acoustic Emission Analysis of Sliding Friction Using Wavelet Transform.*
117. Machikhin, A., et al., *Combined acoustic emission and digital image correlation for early detection and measurement of fatigue cracks in rails and train parts under dynamic loading.* Sensors, 2022. **22**(23): p. 9256.
118. Nazaripoor, H., et al., *Acoustic emission damage detection during three-point bend testing of short glass fiber reinforced composite panels: Integrity assessment.* Journal of Composites Science, 2022. **6**(2): p. 48.
119. Saeedifar, M. and D. Zarouchas, *Damage characterization of laminated composites using acoustic emission: A review.* Composites Part B: Engineering, 2020. **195**: p. 108039.
120. Jolliffe, I.T. and J. Cadima, *Principal component analysis: a review and recent developments.* Philosophical transactions of the royal society A: Mathematical, Physical and Engineering Sciences, 2016. **374**(2065): p. 20150202.
121. Baran, I.J., et al., *Acoustic emission from microcrack initiation in polymer matrix composites in short beam shear test.* Journal of Nondestructive Evaluation, 2018. **37**(1): p. 7.
122. Karsoliya, S., *Approximating number of hidden layer neurons in multiple hidden layer BPNN architecture.* International Journal of Engineering Trends and Technology, 2012. **3**(6): p. 714-717.
123. Li, P., et al., *Analysis of acoustic emission energy from reinforced concrete sewage pipeline under full-scale loading test.* Applied Sciences, 2022. **12**(17): p. 8624.
124. Karthik, M. and C.S. Kumar, *A comprehensive review on damage characterization in polymer composite laminates using acoustic emission monitoring.* Russian Journal of Nondestructive Testing, 2022. **58**(8): p. 705-721.
125. Han, S.N.M.F., et al., *Investigation of tensile and flexural properties of kenaf fiber-reinforced acrylonitrile butadiene styrene composites fabricated by fused deposition modeling.* Journal of Engineering and Applied Science, 2022. **69**(1): p. 52.

Appendix N°1

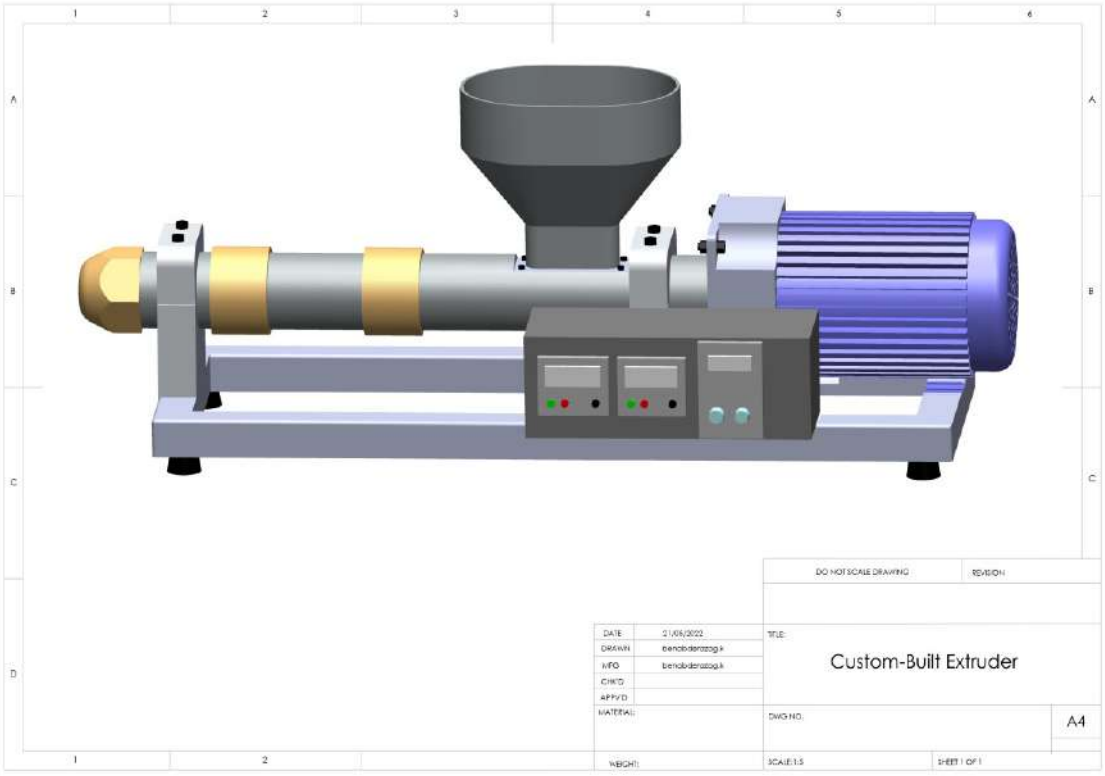
DO NOT SCALE DRAWING
REVISION
DATE
DRAWN
MFG
CHK'D
APP'D
MATERIAL
WEIGHT:
TITLE:
Custom-Built Extruder
DWG NO.
A4
SCALE:1:5
SHEET 1 OF 1

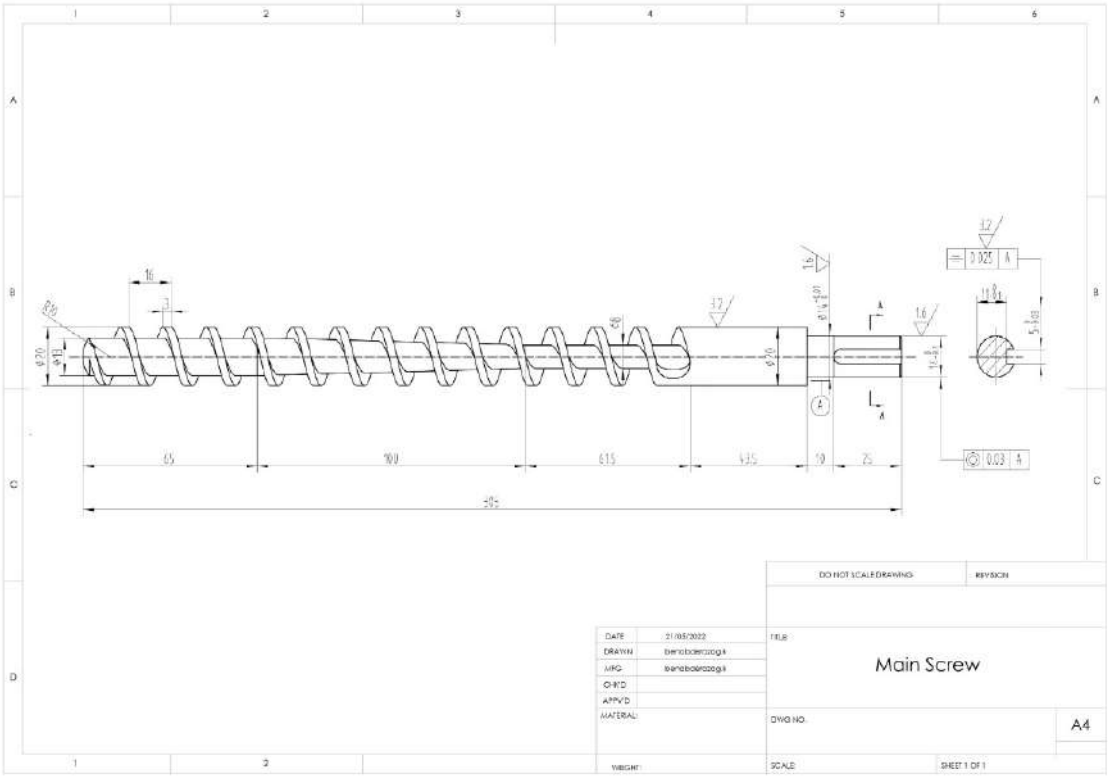
DO NOT SCALE DRAWING
REVISION
DATE
DRAWN
MFG
CHK'D
APP'D
MATERIAL
WEIGHT:
TITLE:
Main Screw
DWG NO.
A4
SCALE:
SHEET 1 OF 1

Appendix N°2

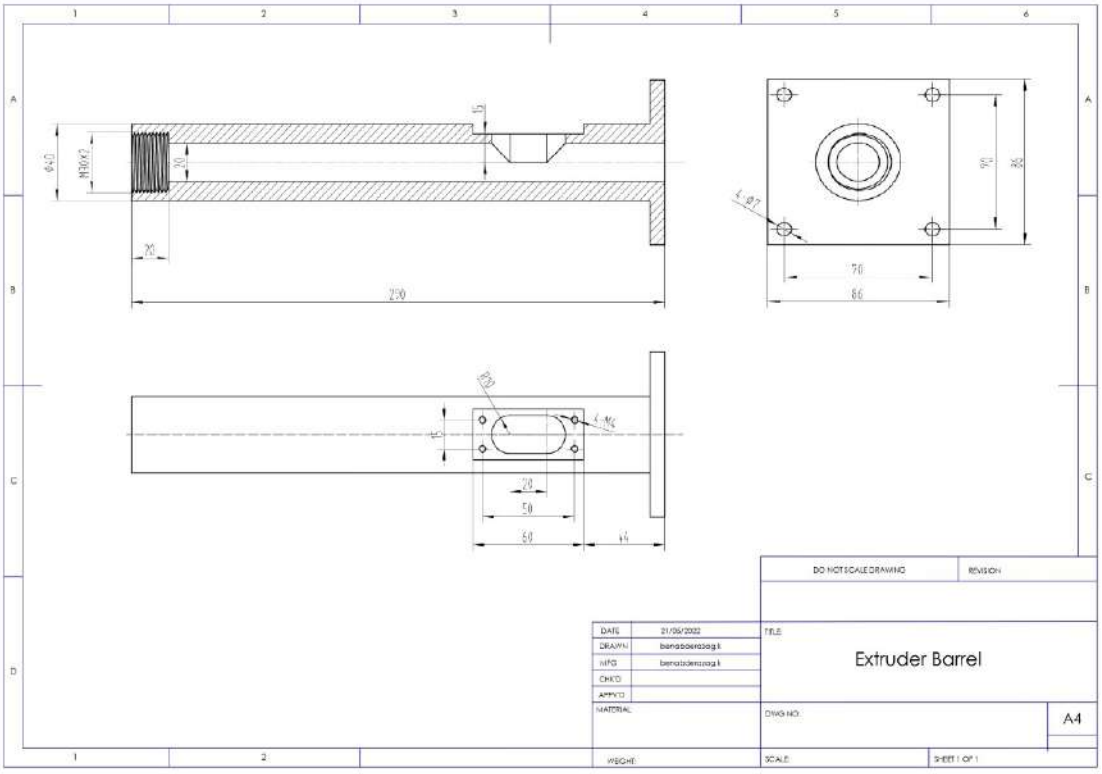

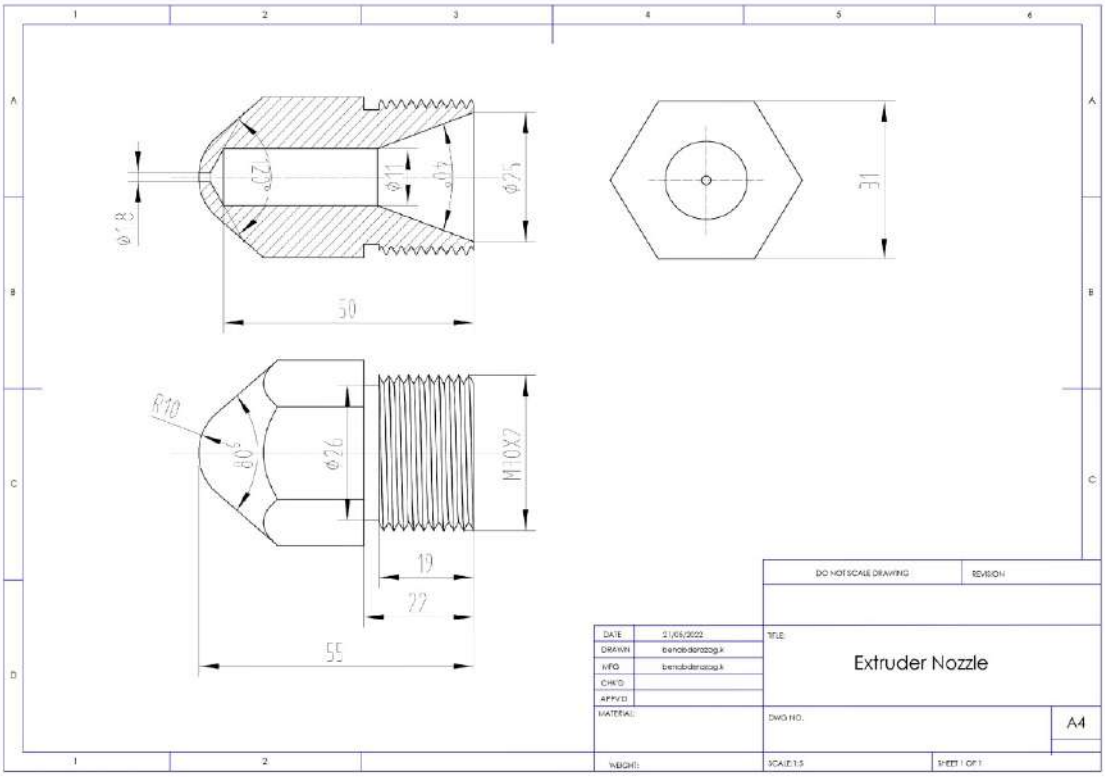

ملخص: تتناول هذه الأطروحة إعداد وتوصيف مركب حيوي من (PLA) مع ألياف *Lygeum spartum* كبديل مستدام للمركبات المدعمة بالألياف الصناعية. قُيّمت الخواص الفيزيائية-الكيميائية والحرارية والميكانيكية بشكل منهجي. أكدت مطيافية الأشعة تحت الحمراء (FTIR) وجود الألياف داخل مصفوفة الـ PLA من خلال ظهور أطياف مميزة لمجموعات السليلوز واللجنين. أظهرت الاختبارات الميكانيكية زيادة بنسبة 26% في الاستطالة عند الكسر، مع تباين في مقاومة الشد يعزى إلى توزيع الألياف. أما اختبارات الانحناء فقد بينت تحسناً في صلابة المادة، حيث ارتفع معامل المرونة من 2.68 إلى 2.98 غيغا باسكال. أظهر التحليل الحراري الوزني(TGA) انخفاضًا طفيفًا في درجة بداية التحلل من 306 °C في PLA النقي إلى 281 °Cفي المركب الحيوي، لكن نطاق التحلل الكلي توسع بشكل ملحوظ 281–379 °C مقابل 306–386°C ، مما يعكس استقرارًا حراريًا ممتدًا عبر مدى أوسع نتيجة التحلل متعدد المراحل لمكونات الألياف وتكوين الشُحُم الكربوني. أكدت تقنية الإثارة بالنبض (IET) زيادة الصلابة، في حين وفرت تقنيات الارتباط الرقمي للصور (DIC) خرائط مفصّلة لتوزيع الانفعال أثناء التحميل. كما كشف تتبّع الانبعاث الصوتي (AE) عن آليات تضرر محددة تساهم في فهم تطور الفشل التدريجي في المركب. مجتمعةً، تشير النتائج إلى أن مركبات *Lygeum spartum*/PLA واعدة للتطبيقات الصناعية خفيفة الوزن التي تتطلب مزيجاً من المتانة الميكانيكية، والمقاومة الحرارية الممتدة، والمعايير البيئية المستدامة.
الكلمات المفتاحية :المواد المركبة الحيوية، PLA، الخصائص الميكانيكية، الاختبارات غير المدمرة، الانبعاث الصوتي، الطباعة ثلاثية الأبعاد.

Résumé: Cette thèse présente la mise au point et la caractérisation d'un biocomposite constitué de PLA renforcé par des fibres de *Lygeum spartum*, proposé comme alternative durable aux composites à fibres synthétiques. Les propriétés physico-chimiques, thermiques et mécaniques ont été évaluées de manière systématique. La spectroscopie FTIR a confirmé la présence des fibres dans la matrice PLA par l'apparition de bandes caractéristiques liées au cellulose et à la lignine. Les essais mécaniques ont montré une augmentation de 26 % de l'allongement à la rupture en traction, la résistance en traction présentant en revanche des variations attribuables à l'hétérogénéité de la distribution des fibres. Les essais en flexion ont mis en évidence un gain de raideur, le module d'élasticité passant de 2,68 GPa pour le PLA pur à 2,98 GPa pour le biocomposite. L'analyse thermogravimétrique (TGA) a révélé une légère diminution de la température d'amorce de dégradation (281 °C contre 306 °C pour le PLA), mais un élargissement marqué du domaine de dégradation (281–379 °C vs 306–386 °C), traduisant une décomposition en plusieurs étapes des constituants fibreux et la formation de résidus carbonés qui prolongent la stabilité thermique à hautes températures. La technique d'excitation par impulsion (IET) a confirmé l'augmentation de la rigidité, tandis que la corrélation d'images numériques (DIC) a fourni des cartes détaillées de la distribution des déformations sous charge. Le suivi par émission acoustique (AE) a mis en évidence des mécanismes de dommage distincts, éclairant la progression du processus de rupture. Ensemble, ces résultats montrent que les biocomposites *Lygeum spartum*/PLA présentent des atouts pour des applications industrielles légères exigeant à la fois robustesse mécanique, résistance thermique étendue et démarche de conception durable.

Mots-clés: biocomposite, PLA, propriétés mécaniques, essais non-destructifs, émission acoustique, impression 3D.

Abstract: This thesis investigates the synthesis and characterization of Lygeum spartum/PLA biocomposites as a sustainable alternative to synthetic fiber composites. Physicochemical, thermal, and mechanical properties were assessed. FTIR spectroscopy confirmed the incorporation of Lygeum spartum fibers within the PLA matrix through the appearance of characteristic cellulose and lignin absorption bands. Mechanical testing revealed a 26% increase in tensile strain at break, while tensile strength exhibited some variation due to fiber distribution. Flexural testing showed an improvement of elastic modulus from 2.68 GPa for neat PLA to 2.98 GPa for the biocomposite. Thermogravimetric analysis indicated a slightly lower onset degradation temperature (281 °C compared to 306 °C for neat PLA); however, the overall degradation range broadened significantly (281–379 °C versus 306–386 °C), suggesting enhanced thermal stability over an extended temperature interval. The Impulse Excitation Technique confirmed higher stiffness, while Digital Image Correlation provided detailed mapping of strain distribution under load. Acoustic Emission monitoring further revealed distinct damage mechanisms, offering valuable insights into the progressive failure behavior of the biocomposite. Collectively, these results highlight the potential of Lygeum spartum/PLA biocomposites for lightweight industrial applications requiring mechanical robustness, extended thermal resistance, and sustainable material design.

Keywords: biocomposite, PLA, mechanical properties, non-destructive testing, acoustic emission, 3D printing.